ISSN 2413-9432

BIOMEDICAL PHOTONICS

Volume 13, # 4, 2024

In the issue:

BMP

Российская Фотодинамическая Ассоциация

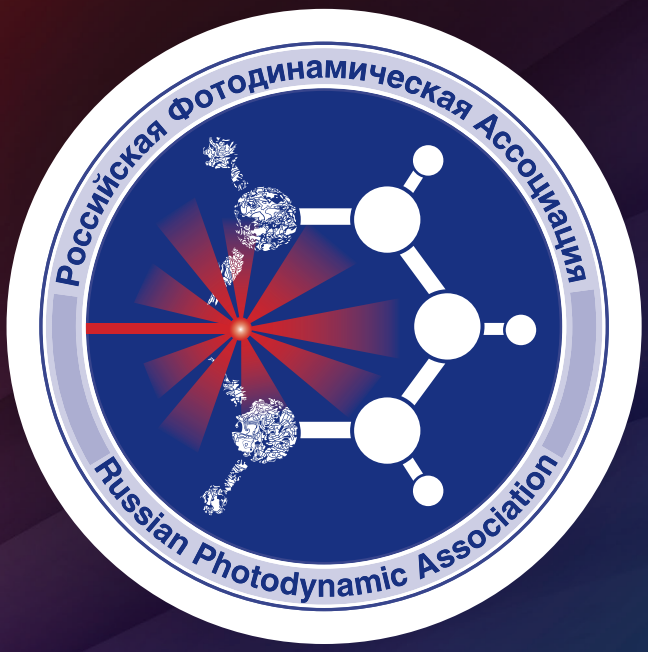

www.pdt-association.com

BIOMEDICAL PHOTONICS

BIOMEDICAL PHOTONICS –
research and practice, peer-reviewed, multidisciplinary journal.
The journal is issued 4 times per year.
The circulation – 1000 copies., on a quarterly basis.

The journal is included into the List of peer-reviewed science press of the State Commission for Academic Degrees and Titles of Russian Federation
The journal is indexed in the international abstract and citation database – Scopus.

The publisher «Agentstvo MORE».
Moscow, Khokhlovskiy lane., 9

Editorial staff:

Chief of the editorial staff	Ivanova-Radkevich V.I.
Science editor professor	Mamontov A.S.
Literary editor	Moiseeva R.N.
Translators	Kalyagina N.A.
Computer design	Kreneva E.I.
Desktop publishing	Shalimova N.M.

The Address of Editorial Office:
Russia, Moscow, 2nd Botkinskiy proezd, 3
Tel. 8 (495) 945–86–60
www: PDT-journal.com
E-mail: PDT-journal@mail.ru

Corresponding to:
125284, Moscow, p/o box 13

Registration certificate ПИ № ФС 77–51995, issued on 29.11.2012 by the Federal Service for Supervision of Communications, Information Technology, and Mass Media of Russia

The subscription index of «Rospechat» agency – 70249

BIOMEDICAL PHOTONICS

BIOMEDICAL PHOTONICS –
научно-практический, рецензируемый,
мультидисциплинарный журнал.
Выходит 4 раза в год.
Тираж – 1000 экз., ежеквартально.

Входит в Перечень ведущих рецензируемых научных журналов ВАК РФ.
Индексируется в международной реферативной базе данных Scopus.

Издательство «Агентство МОРЕ».
Москва, Хохловский пер., д. 9

Редакция:

Зав. редакцией	Иванова-Радкевич В.И.
Научный редактор	проф. Мамонтов А.С.
Литературный редактор	Моисеева Р.Н.
Переводчики	Калягина Н.А.
Компьютерный дизайн	Кренева Е.И.
Компьютерная верстка	Шалимова Н.М.

Адрес редакции:
Россия, Москва, 2-й Боткинский пр., д. 3
Тел. 8 (495) 945–86–60
www: PDT-journal.com
E-mail: PDT-journal@mail.ru

Адрес для корреспонденции:
125284, Москва, а/я 13

Свидетельство о регистрации ПИ
№ ФС 77–51995, выдано 29.11.2012 г.
Федеральной службой по надзору в сфере связи, информационных технологий и массовых коммуникаций (Роскомнадзор)

Индекс по каталогу агентства «Роспечать» – 70249

ORIGINAL ARTICLES

REVIEWS OF LITERATURE

ОРИГИНАЛЬНЫЕ СТАТЬИ

ОБЗОРЫ ЛИТЕРАТУРЫ

ORIGINAL ARTICLES

COMPARISON OF OPTICAL-SPECTRAL CHARACTERISTICS OF GLIOBLASTOMA AT INTRAOPERATIVE DIAGNOSIS AND *EX VIVO* OPTICAL BIOPSY

Romanishkin I.D.[1], **Savelieva T.A.**[1,2], **Ospanov A.**[2], **Kalyagina N.A.**[1,2], **Krivetskaya A.A.**[1,2], **Udeneev A.M.**[2], **Linkov K.G.**[1], **Shugay S.V.**[3], **Pavlova G.V.**[3,4], **Pronin I.N.**[3], **Loschenov V.B.**[1,2]
[1]Prokhorov General Physics Institute of Russian Academy of Sciences, Moscow, Russia
[2]National Research Nuclear University MEPhI, Moscow, Russia
[3]N.N. Burdenko National Medical Research Center of Neurosurgery, Moscow, Russia
[4]Institute of Higher Nervous Activity and Neurophysiology of the Russian Academy of Sciences, Moscow, Russia

Abstract

The difficulty of intraoperative delineation of glial tumors is due to the peculiarities of their growth along vessels and nerve fibers with infiltration of healthy white matter. Insufficiently complete removal of tumor tissues leads to recurrences, and excessive removal is fraught with neurological complications. Optical spectroscopy methods are characterized by high speed, accuracy and non-invasiveness, which determines the prospects of their use for intraoperative demarcation of the boundaries of such tumors. Fluorescence and diffuse reflectance spectroscopy have found wide application in intraoperative neuronavigation, mainly for detecting the edges of diffuse gliomas. At the same time, in recent years the direction of *ex vivo* spectral analysis of tumor samples using a combination of various optical spectroscopy methods, including both elastic and inelastic scattering spectroscopy, has been actively developed. Obviously, the ability to obtain spectra intraoperatively and on fresh specimens is different. The present article compares the results of the analysis of optical-spectral characteristics of intracranial tumors at intraoperative diagnosis and *ex vivo* analysis and proposes a mathematical model for interpretation of the observed dependencies.

Keywords: glial tumors, optical spectroscopy, scattering, mathematical modeling, Monte Carlo simulation.

Contacts: Romanishkin I.D., e-mail: igor.romanishkin@nsc.gpi.ru.

For citations: Romanishkin I.D., Savelieva T.A., Ospanov A., Kalyagina N.A., Krivetskaya A.A., Udeneev A.M., Linkov K.G., Shugay S.V., Pavlova G.V., Pronin I.N., Loschenov V.B. Comparison of optical-spectral characteristics of glioblastoma at intraoperative diagnosis and *ex vivo* optical biopsy, *Biomedical Photonics*, 2024, vol. 13, no. 4, pp. 4–12. doi: 10.24931/2413–9432–2024–13–4–4–12

СРАВНЕНИЕ ОПТИКО-СПЕКТРАЛЬНЫХ ХАРАКТЕРИСТИК ГЛИОБЛАСТОМЫ ПРИ ИНТРАОПЕРАЦИОННОЙ ДИАГНОСТИКЕ И ОПТИЧЕСКОЙ БИОПСИИ *EX VIVO*

И.Д. Романишкин[1], **Т.А. Савельева**[1,2], **А. Оспанов**[2], **Н.А. Калягина**[1,2], **А.А. Кривецкая**[1,2], **А.М. Уденеев**[2], **К.Г. Линьков**[1], **С.А. Горяйнов**[3], **С.В. Шугай**[3], **Г.В. Павлова**[3,4], **И.Н. Пронин**[3], **В.Б. Лощенов**[1,2]
[1]Институт общей физики им. А.М. Прохорова Российской академии наук, Москва, Россия
[2]Национальный исследовательский ядерный университет «МИФИ», Москва, Россия
[3]Национальный медицинский исследовательский центр нейрохирургии имени академика Н. Н. Бурденко, Москва, Россия
[4]Институт высшей нервной деятельности и нейрофизиологии Российской академии наук, Москва, Россия

Резюме

Сложность интраоперационного определения границ глиальных опухолей обусловлена особенностями их роста вдоль сосудов и нервных волокон с инфильтрацией здорового белого вещества. При этом недостаточно полное удаление опухолевых тканей приво-

дит к рецидивам, а избыточное удаление чревато неврологическими осложнениями. Методы оптической спектроскопии характеризуются высокой скоростью, точностью и неинвазивностью, что обуславливает перспективность их использования для интраоперационной демаркации границ таких опухолей. Спектроскопия флуоресценции и диффузного отражения нашли широкое применение в интраоперационной нейронавигации, главным образом, для обнаружения краев диффузных глиом. При этом в последние годы активно развивается направление *ex vivo* спектрального анализа образцов опухолей с помощью сочетания различных методов оптической спектроскопии, включающих спектроскопию как упругого, так и неупругого рассеяния. Очевидно, возможности регистрации спектров при интраоперационной работе и на свежих образцах отличаются. В настоящей статье проведено сравнение результатов анализа оптико-спектральных характеристик внутричерепных опухолей при интраоперационной диагностике и анализе *ex vivo*, а также предложена математическая модель для интерпретации наблюдаемых зависимостей.

Ключевые слова: глиальные опухоли, оптическая спектроскопия, рассеяние, математическое моделирование, Монте-Карло моделирование.

Контакты: Романишкин И.Д. e-mail: igor.romanishkin@nsc.gpi.ru.

Для цитирования: Романишкин И.Д., Савельева Т.А., Оспанов А., Калягина Н.А., Кривецкая А.А., Уденеев А.М., Линьков К.Г., Горяйнов С.А., Шугай С.В., Павлова Г.В., Пронин И.Н., Лощенов В.Б. Сравнение оптико-спектральных характеристик глиобластомы при интраоперационной диагностике и оптической биопсии *ex vivo* // Biomedical Photonics. – 2024. – Т. 13, № 4. – С. 4-12. doi: 10.24931/2413–9432–2024–13–4–4–12

Introduction

Currently, the primary line of therapy for highly malignant brain tumors is surgical resection, but *in vivo* tumor delineation remains a major challenge. Recent technological advances in neurophotonic developments such as Raman spectroscopy, thermal imaging, optical coherence tomography, and fluorescence spectroscopy have enabled the development of techniques for minimally invasive neurosurgery [1]. Despite advances in optical techniques, biopsy analysis remains the standard diagnostic tool for tumor delineation.

Further development of intraoperative analysis techniques with visual inspection would provide neurosurgeons with real-time information, shorten surgical procedure time, and enable more accurate resection by detecting residual or hidden tumor foci. Visual inspection tools can view and analyze the location, size, shape, type, and extent of tumors [1–6].

Among the promising new optical techniques for cancer diagnosis with the possibility of intraoperative tissue assessment is Diffuse Reflectance Spectroscopy (DRS). DRS is a non-invasive or minimally invasive technique that typically uses separate optical fibers – to deliver broadband light to the tissue and to register diffusely reflected light with a spectrometer. Diffuse reflectance signal formation is possible because biological tissues are characterized by their ability to scatter light multiple times, resulting in light scattering from the source in all directions, with a portion of the scattered light returning back. DRS can provide such clinical information as total hemoglobin content, tissue oxygen saturation, tissue lipid and water content, and tissue scattering properties. The method has already been used, for example, in studies to classify tumor tissue in upper gastrointestinal cancers [7], to distinguish tumor tissue from fibrosis in patients with rectal cancer as a guide to surgery [8], and to record optical mammograms and quantify absorption and scattering properties, from which hemoglobin concentration and oxygen saturation of healthy and pathological breast tissue were obtained and analyzed [9]. Studies have shown that DRS can aid in intraoperative decision-making during cancer surgery, including selecting the best resection plane and area, and distinguishing fibrotic or healthy tissue from tumor tissue.

In neurosurgery, the DRS method has been used to assess blood fractions and oxygen saturation changes by spectroscopic signal and hemoglobin absorption spectrum [10], to distinguish between glial tumors and normal brain *ex vivo* by assessing DRS signal [11], and to detect cancer *in vivo* without labels and in real time during brain surgery [12].

However, the accuracy of tissue classification is still insufficient and the DRS method requires further development. In this paper, we interpret a number of our findings on the diffuse light reflection spectra of intracranial tumor tissues and compare the data obtained *in vivo* during neurosurgical surgery for tumor removal, and *ex vivo* during biobanking. The results of the comparison allows avoiding methodological errors when translating such technologies. The mathematical model of elastic multiple scattering of light by the studied tissues proposed in the article allows to take into account not only karyomorphometric data, obvious in classical histological analysis with hematoxylin-eosin staining, but also demonstrates the necessity to take into account the contribution of larger structures, such as myelin sheaths of nerves, as well as, on the contrary, smaller ones, such as subcellular structures, e.g. mitochondria.

Materials and methods

Method and device for simultaneous registration of diffuse reflectance and fluorescence spectra in vivo

Diffuse reflectance spectra of tumor tissues are the object of the present study. The fluorescence of 5-aminolevulinic acid (5-ALA) induced protoporphyrin IX (PpIX) was used as a marker of tumor changes in

the area of interest. In the process of post-processing of spectral data obtained in the clinic, we analyzed the co-distribution of PpIX and markers of structural changes determined by the diffuse reflectance spectrum.

For simultaneous registration of diffuse reflectance and fluorescence spectra, the device described in [13] was used. The emission from a broadband source (halogen lamp) was filtered through a 500–600 nm bandpass filter. A laser source with a wavelength of 632.8 nm (He-Ne laser) was used to excite the fluorescence. Diffuse reflectance and fluorescence spectra were recorded simultaneously in 500–640 and 640–850 nm spectral ranges, respectively. Measurements were performed using a fiber-optic probe, the illumination and the receiving fibers were collected in a special bundle and placed on one side of the object, which determined the specifics of signal registration in the diffuse reflectance geometry (Fig. 1). Several hours before the operation, a solution of 5-ALA hydrochloride was injected into the patient's body. The combined spectra of normal tissue (usually the cerebral cortex at a distance from the tumor projection) and pathologically altered tissue above the tumor, in the tumor, and in the tumor bed (to control the quality of the resection) were measured sequentially during the tumor resection surgery. This paper presents a retrospective analysis of *in vivo* data obtained at the Burdenko Neurosurgery Center. Diffuse reflectance spectra recorded during the removal of glioblastomas (in 38 patients, 163 samples in total) and anaplastic astrocytomas (in 6 patients, 35 samples in total) were considered. Glioblastoma samples were distributed as follows: 14 samples with normally appearing white matter (NAWM), 18 samples from the perifocal area of tumor, 86 samples from tumor center, 18 samples with necrotic tissues. Anaplastic astrocytoma samples included 21 samples from tumor center, 11 – from perifocal area, 3 NAWM, and no necrosis.

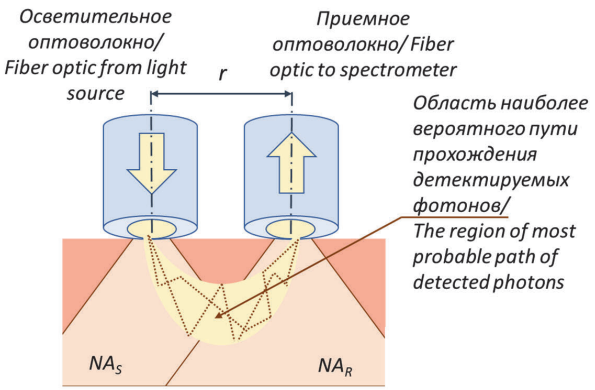

Рис. 1. Схема регистрации сигнала диффузного отражения: r – расстояние от центра осветительного волокна до центра приемного волокна, NA_s – числовая апертура осветительного волокна, NA_R – числовая апертура приемного волокна.
Fig. 1. Scheme of registration of diffuse reflection signal: r – distance from the center of the illumination fiber to the center of the receiving fiber, NA_s – numerical aperture of the illumination fiber, NA_R – numerical aperture of the receiving fiber.

Method and device for simultaneous recording of diffuse reflectance and Raman spectra ex vivo

Studies of the combined method of *ex vivo* optical biopsy of tumor samples were conducted in the laboratory of neurosurgical anatomy and preservation of biological materials at the Burdenko Neurosurgery Research Center on tumor tissue samples extracted during neurosurgical operations, immediately after removal. Samples from patients diagnosed with glioblastoma (n=60) were studied. From each patient 1–4 biopsy specimens were taken with subsequent verification by pathomorphologic examination (84 specimens in total).

For all samples, Raman spectra were measured with StellarNet Raman-HR-TEC-785 spectrometer under 785 nm excitation, fluorescence was measured at 405 nm and 632.8 nm, and diffuse reflectance was measured in 500–600 nm spectral range using Biospec LESA-01-BIOSPEC spectrometer. In this paper, we use only diffuse reflectance spectroscopy data in white light (to calculate hemoglobin concentration) and at 632.8 nm, just as we did in *in vivo* measurements performed in the operating room. The results of our previous studies of this method [14–16] showed a significant contribution of these spectroscopic features to the principal components.

Algorithm for processing diffuse reflectance spectra

Raman, fluorescence, and diffuse reflectance spectra were subjected both to preprocessing in order to increase decoding properties and to various variants of decomposition in order to highlight characteristic features peculiar to the tissues under study.

From the fluorescence spectrum of PpIX, we calculated the values of the 632.8 nm integral backscatter laser intensity (area under the spectrum curve in the range of 625–640 nm) and the value of the PpIX fluorescence index (ratio of the area under the spectrum curve in the range of 690–730 nm to the value of the 632.8 nm integral laser intensity). In this work, we consider only the first of these parameters.

The spectrum of diffusely reflected by the tissue broadband light was used to calculate the hemoglobin concentration [17] in the sample and the light scattering coefficient [18].

Model of light interaction with structural elements of tumor tissues

To determine the influence of the measurement geometry and biological processes occurring in the tumor on the recorded signals, a mathematical model of the studied biological tissue in different states was developed. It considered both the variation of individual tissue components using Mie theory and their concentration and composition of the medium, for which the Monte Carlo simulation method was chosen, which has a higher accuracy in the tissue regions proximal

to the illuminator and receiver than the diffusion approximation of the radiative transfer theory [19].

Cells, organelles, elements of intercellular matrix, nerve endings can be approximated by spheres and cylinders with refractive indices corresponding to the content of proteins and fats in them, and immersed in a medium whose refractive index is determined by all the molecules contained in it that are not accounted for as independent scatterers. The scattering cross section of unpolarized light by a spherical particle was determined according to [20]. The infinite cylinder solution, also proposed by Bohren and Huffman, was used to model the scattering of an electromagnetic wave on myelinated nerve fibers. Two variants of wave incidence with respect to the plane in which the cylinder lies: parallel and perpendicular to the plane of incidence, were considered and averaged.

Numerical modeling of radiation propagation in scattering and absorbing media

The Monte Carlo method is widely used for numerical solution of the radiative transfer theory (RTT) equation, which is based on modeling of photon transport in a scattering medium. The initial conditions are set and each act of photon scattering on the inhomogeneities of the medium is traced up to its absorption or exit from the sample. Free path length and rotation angle are random variables with theory-based distribution. The scattering and absorption probabilities are determined by the μ_s' and μ_a coefficients. The main disadvantage of the Monte Carlo method is the substantial expenditure of computational resources, which renders it impractical for addressing the inverse problem in real time. However, it is possible to develop algorithms for data interpretation based on Monte Carlo simulation, as was done in [21] to describe the dependence of the diffuse reflection coefficient on the absorption and scattering coefficients for a semi-infinite medium.

In the present work, a Monte Carlo packet method has been implemented in the Visual Studio development environment using C# language tools. It is based on the assumption that a set of photons begins to co-propagate in the medium, but gradually the population of the packet runs out due to absorption, and the remaining part of the packet is scattered until the population of the packet becomes too small. This technique allows us to increase the dynamic range of the calculated distribution at unchanged costs of machine time in case of the absorbing medium. For registration of radiation the possibility of receiving radiation with a given aperture on a given area at a given distance from the source in the XY plane is realized.

Determination of input parameters of mathematical modeling

The main characteristic of glial tumors is their growth along myelinated nerve fibers and blood vessels without forming a capsule, which leads to their infiltration into the normal white matter of the brain [22]. At the organ-tissue level, glial tumors consist of central and perifocal zones [23] and lead to displacement, deviation, and destruction of nerve tracts during their development [24]. The central zone of glioblastoma multiforme (the most malignant form of glial tumors) is characterized by the development of necrosis in the tumor nucleus with concomitant destructive changes of myelinated nerve fibers [25, 26].

At the tissue level, the number and shape of cell membranes should also be taken into account. It is well known that about 50% of the white matter consists of myelin sheaths of nerve tracts, which are multilayered membranes consisting of a lipid bilayer (70-85% of dry matter) with protein inclusions (15–30%) [27, 28], which causes its high refractive index. How developed the surface of the astrocyte membranes is also important, as this factor is altered by cell compaction in the tumor and affects scattering.

In [29], diffusion tensor MRI was used to show that fluctuations in the fractional anisotropy index correlate with the integrity of nerve tracts formed by myelinated fibers, as well as with the state of the cells. Thus, the significant decrease of the fractional anisotropy index in the center of glioblastoma is due to a high degree of nerve fiber disintegration and necrotic changes, while its more moderate deviations are observed in the perifocal zone, where nerve tracts are still structured and intact glia

Таблица 1
Результаты исследования показателя фракционной анизотропии для глиальных опухолей различной степени озлокачествления

Table 1
Results of the fractional anisotropy index study for glial tumors with different degrees of malignancy

Центр опухоли Tumor center	Граница Edge	Нормальное белое вещество Normal white matter	Источник Reference
Глиобластома (IV стадия) Glioblastoma (Grade IV)			
	0.257	0.467	[30]
0.13	0.16	0.47	[26]
0.13	0.2085	0.4685	среднее average
Анапластическая астроцитома (III стадия) Anaplastic astrocytoma (Grade III)			
0.165	0.168	0.391	[31]
	0.223	0.467	[30]
0.165	0.1955	0.429	среднее average
Диффузная астроцитома (II стадия) Diffuse astrocytoma (Grade II)			
0.144	0.259	0.391	[32]

cells are observed. The numerical values of this coefficient, averaged from data from the literature, are shown in Table 1.

For modeling purposes, to unify data from different sources, the fractional anisotropy index values obtained in each study were normalized for the tumor center and margin to the values from normal white matter. After that, the average values were calculated, which were reduced to the absolute value of the fractional anisotropy index by multiplication by its average value for normal white matter for all studies.

As can be seen in Table 2, at the cellular level, glioblastoma multiforme (Grade IV) exhibits such features as dense cellularity, atypical development of nuclei, increase in their size, and pleomorphism (diversity of shapes) [36]. Anaplastic astrocytoma is characterized by increased cell density, anaplasia, and mitosis, but to a lesser extent than glioblastoma. Benign tumors show a moderate increase in cell density and nuclei size without cellular atypia or mitotic activity [38, 39]. At the subcellular level, the most critical changes occur in the content and structure of mitochondria. In normal tissue, mitochondria make up about 7–8% of the cell volume [40, 41]. In liver tissue, mitochondria have been shown to have a significant effect on light scattering by the cell [42, 43]. Also, by analyzing liver slices using phase-contrast microscopy, Schmitt and Kumar showed a significant contribution of organelles to light scattering by cells [44].

Results and discussion

Comparison of in vivo and ex vivo data

The results of our previous work have shown that in the combined spectral analysis of glial tumor tissues, one of the most prominent features in classification is the intensity of diffuse light scattering [13, 16]. Results confirming this observation were obtained in [12].

Our *in vivo* and *ex vivo* studies included different kinds of pathomorphological data, which determined the samples as coming from normal white matter, perifocal tumor area, or actively growing part of tumor, and the percentages of tumor and necrotic tissue in the sample (Fig. 2). In our *ex vivo* biobanking studies of optic-spectral characteristics, the samples were represented as having a certain percentage of tumor/connective/fibrotic/necrotic tissue. However, when we subdivide this sample into quartiles by tumor tissue content (with the exclusion of necrotic areas), we see a similar pattern of correlation between the degree of malignancy in the measured area and the scatter score. The lowest light-scattering values correspond either to the perifocal zone (in *in vivo* measurements) or to a tumor content of 25 to 50% in the sample (in *ex vivo* measurements), which are reasonable to compare with each other. Some differences in the distribution of light scattering in different types of glioblastoma tissues are also observed. For example, in *in vivo* measurements, we could afford to record spectral dependencies from normal white matter far away from the tumor, as this did not require its removal.

The healthy areas of white matter obtained in the biobanking process, were the areas adjacent to the tumor showing morphological signs of normality. However, according to the light-scattering ratio for *ex vivo* measurements, we can assume that these samples were still subject to some changes. Our mathematical model of the relevant structural changes occurring in neural tissues during tumor development is presented in the following section.

Таблица 2
Данные кариоморфометрии для глиальных опухолей различной степени озлокачествления
Table 2
Karyomorphometry data for glial tumors of different degrees of malignancy

Гистологический тип Histological type	Макс. диаметр, мкм Max diameter, μm	Отношение меньшей оси эллипса к большей Inverse aspect ratio of the ellipsis	Клеточная плотность, 1/мм^2 Cell density, 1/mm^2	Клеточная плотность, 1/мкм^3 Cell density, 1/μm^3
Нормальное белое вещество Normal white matter	4–5 [33]	-	850.9 [32]	0.025×10^{-3}
Пилоцитарная астроцитома (степень I) Pilocytic astrocytoma (Grade I)	-	-	2689±745 [34]	0.14×10^{-3}
Диффузная астроцитома (степень II) Diffuse astrocytoma (Grade II)	8.93±1.26 [35]	0.74±0.13 [36]	2363±726 [37]	0.12×10^{-3}
Анапластическая астроцитома (степень III) Anaplastic astrocytoma (Grade III)	9.61±0.9 [27]	0.65±0.15 [36]	4864±1428 [37]	0.34×10^{-3}
Глиобластома (степень IV) Glioblastoma (Grade IV)	10.65±3.44 [35]	0.627±0.5 [38]	5540±2160	0.41×10^{-3}

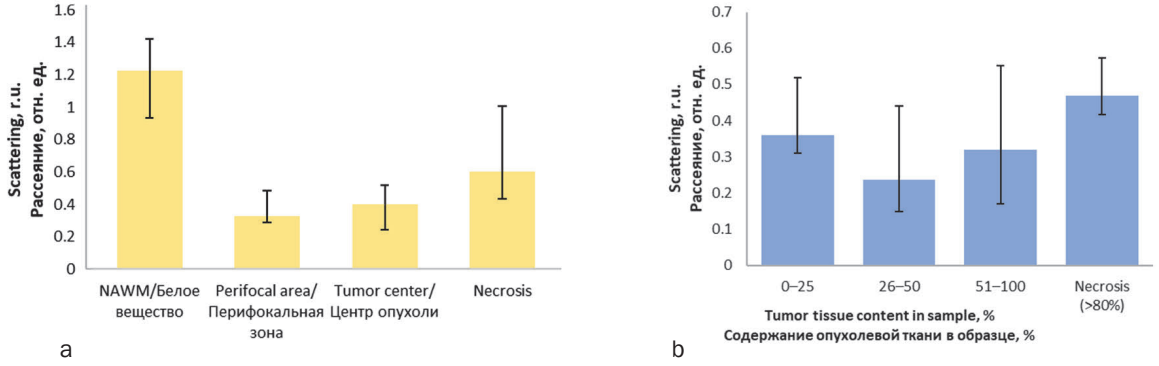

Рис. 2. Вариация индекса диффузного рассеяния в опухолевых тканях (представлен сигнал диффузного отражения на длине волны 632.8 нм), регистрируемая (a) интраоперационно *in vivo* и (b) на образцах из операционной *ex vivo*.
Fig. 2. Diffuse scattering index in tumor tissues (as scattering index at 632.8 nm) registered (a) intraoperatively *in vivo* and (b) in *ex vivo* samples.

Comparison of results of mathematical modeling and spectroscopic measurements of gliomas

Local changes in light-scattering properties and accumulation of tumor marker (5-ALA induced PpIX) in the patient's tissues during tumor removal were investigated. For this purpose, the data of spectroscopic study performed *in vivo* in different tumor sections were compared with the subsequent sampling of histological material from the same sections. As a result of the analysis of structural features of nervous tissues, and in particular healthy white matter of the brain and glial tumors of different degrees of malignancy, as well as physiological characteristics, a mathematical model of scattering signal formation in the tissues under study was created using Mie theory (Table 3). The optical parameters of the model composition media obtained as a result of modeling are shown in Table 4.

Comparison of the results of numerical modeling of laser radiation propagation in a complex medium that contains scatterers with parameters corresponding to the main structural elements of nervous tissues and hemoglobin as the main chromophore and the data of spectroscopic study carried out *in vivo* showed a good correspondence between the developed mathematical model and clinical data (Table 5).

As can be seen from the above results, both in numerical experiment and *in vivo* spectroscopic studies, differences in light-scattering properties were observed for the center and edge of tumor of different degrees of malignancy.

The light scattering of the central portion of benign neoplasms is less pronounced than that observed in glioblastoma. However, in both cases, this value is markedly lower than that exhibited by normal white matter. (Fig. 2). This can be explained by competing effects occurring at the tissue level during tumor development affecting the scattering signal. Gradual demyelination of nerve fibers, their displacement and destructurization, as well

Таблица 3
Морфологические характеристики, послужившие входными данными для моделирования оптических свойств отдельных компонентов нервных тканей

Table 3
Morphological characteristics that served as input data for modeling the optical properties of individual components of neural tissues

Параметр Parameter	Центр Center			Край опухоли Tumor edge		
	a, мкм a, μm	ρ, 1/мкм² ρ, 1/μm²	n	a, мкм a, μm	ρ, 1/мкм² ρ, 1/μm²	n
Норма Normal tissue	4 / 0.5 / 0.8 (100%)	0.0004 / 200 / 0.07	1.39 / 1.42 / 1.455	-		
Степень II–III Grade II–III	9.5 / 0.3 / 0.8 (40%); 0.48 (60%*)	0.0007 / 70 / 0.07	1.39 / 1.42 / 1.455	8.5 / 0.3 / 0.8 (50%); 0.48 (50%*)	0.0005 / 70 / 0.07	1.39 / 1.42 /1.455
Степень IV Grade IV	10.65 / 0.25 / 0.8 (20%); 0.48 (80%*)	0.0015 / 0-30 / 0.07	1.39 / 1.42 / 1.455	9.5 / 0.25 / 0.8 (40%); 0.48 (60%*)	0.0007 / 30 / 0.07	1.39 / 1.42 /1.455

*a – диаметр рассеивателя, ρ – плотность ядер, n – показатель преломления. Значения приведены для ядра / митохондрии / миелинизированных волокон.
*a – diameter of scatterers, ρ – nuclei density, n – reflectance index. Values are provided for nucleus / mitochondria / myelinated fibers.

Таблица 4
Оптические свойства нервных тканей с различной морфологией, полученные в результате математического моделирования с использованием многокомпонентной модели соответствующих тканей

Table 4
Optical properties of nervous tissues with different morphology obtained by mathematical modeling using a multi-component model of the corresponding tissues

Параметр Parameter	Длина волны, нм Wavelength, nm	Норма Normal tissue	Степень II–III Grade II–III		Степень IV Grade IV	
			Центр опухоли Tumor center	Край опухоли Tumor edge	Центр опухоли Tumor center	Край опухоли Tumor edge
μ_s, 1/см μ_s, 1/cm	**632.8**	113.7	49.7	54.2	112.6	50.9
	710	88.4	39.3	42.9	90	40.3
μ_a, 1/см μ_a, 1/cm	**632.8**	1.7	3	2.2	7.1	3.5
	710	0.76	2	1.5	2.5	1.2
G	**632.8**	0.85	0.89	0.86	0.9	0.89
	710	0.84	0.88	0.85	0.89	0.88

Таблица 5
Сопоставление данных имитационного моделирования и результатов спектроскопии *in vivo*

Table 5
Comparison of simulation results with *in vivo* spectroscopy

Диффузное отражение по отношению к нормальной ткани Diffuse reflectance compared to normal tissue		Степень II–III Grade II–III		Степень IV Grade IV	
		Центр опухоли Tumor center	Край опухоли Tumor edge	Центр опухоли Tumor center	Край опухоли Tumor edge
Монте-Карло Monte Carlo	632.8 нм 632.8 nm	0.22±0.001	0.41±0.002	0.56±0.001	0.28±0.001
in vivo		0.21±0.02	0.37±0.02	0.53±0.02	0.26±0.02

as a decrease in the number of mitochondria due to the transition of tumor cells from oxidative phosphorylation to glycolysis, lead to a decrease in the scattering signal, while an increase in the size and density of nuclei leads to its increase. For different parts of the tumor of one patient, this effect can be traced by comparing the central part of the tumor and its edge, where these changes are less pronounced than in the center. Here we see the opposite picture. The tumor edge of benign neoplasms exhibits higher scattering properties than the edge of glioblastoma, because in this region in the former case there is not yet significant destructurization of myelinated fibers and the decline of the scattering signal is due to the greatest extent to metabolic changes leading to the depletion of intracellular composition, while in the latter case all components leading to the decline of the scattering signal are already evident, but cellular density is not as pronounced as in the center of the tumor. Thus, we can rank the considered areas of pathologically altered tissues in the following order: normal white matter, edge of benign tumor, center of benign tumor, edge of malignant tumor, center of malignant tumor, which illustrates the competitive nature of parameters influencing the light scattering signal.

Conclusion

The study of the scattering properties of glial tumors, both *in vivo* during neurosurgical operations and *ex vivo* during biobanking of the samples, showed that in the regions with low accumulation of tumor marker (5-ALA induced PpIX) and insignificant changes perceived visually, that the light scattering signal, registered at a small distance between the light source and the receiver and that mostly depends on the changes occurring at the subcellular level, has the highest contrast compared to the normal white matter of the brain. Thus, the diagnostic value of analyzing the light-scattering properties of neural tissues in the perifocal zone of glial tumors has been demonstrated.

This work was financially supported by the Ministry of Science and Higher Education of the Russian Federation (Agreement No. 075-15-2021-1343 dated October 4, 2021).

REFERENCES

1. Vasefi F., MacKinnon N., Farkas D. L. et al. Review of the potential of optical technologies for cancer diagnosis in neurosurgery: a step toward intraoperative neurophotonics, *Neurophotonics*, 2016, vol. 4(1), pp. 011010. doi: 10.1117/1.NPh.4.1.011010.
2. Goryaynov S. A., Okhlopkov V. A., Golbin D. A. et al. Fluorescence Diagnosis in Neurooncology: Retrospective Analysis of 653 Cases, *Frontiers in Oncology*, 2019, vol. 9, pp. 830. doi: 10.3389/fonc.2019.00830.
3. Goryaynov S. A., Buklina S. B., Khapov I. V. et al. 5-ALA-guided tumor resection during awake speech mapping in gliomas located in eloquent speech areas: Single-center experience, *Frontiers in Oncology*, 2022, vol. 12, pp. 940951. doi: 10.3389/fonc.2022.940951.
4. Rynda A. Yu., Olyushin V. E., Rostovtsev D. M. et al. Fluorescent diagnostics with chlorin e6 in surgery of low-grade glioma, *Biomedical Photonics*, 2021, vol. 10(4), pp. 35–43. doi: 10.24931/2413-9432-2021-10-4-35-43.
5. Rynda A. Yu., Olyushin V. E., Rostovtsev D. M. et al. Results of microsurgical resection of glioblastomas under endoscopic and fluorescent control, *Biomedical Photonics*, 2024, vol. 13(3), pp. 20–30. doi: 10.24931/2413-9432-2024-13-3-20-30.
6. Udeneev A. M., Kalyagina N. A., Reps V. F. et al. Photo and spectral fluorescence analysis of the spinal cord injury area in animal models, *Biomedical Photonics*, 2023, vol. 12(3), pp. 15–20. doi: 10.24931/2413-9432-2023-12-3-16-20.
7. Liu Y.-X., Yang Y.-S. Using Diffuse Reflectance Spectroscopy to Classify Tumor Tissue in Upper Gastrointestinal Cancers, *JAMA Surgery*, 2023, vol. 158(7), pp. 772. doi: 10.1001/jamasurg.2022.8430.
8. Baltussen E. J. M., Brouwer De Koning S. G., Sanders J. et al. Using Diffuse Reflectance Spectroscopy to Distinguish Tumor Tissue From Fibrosis in Rectal Cancer Patients as a Guide to Surgery, *Lasers in Surgery and Medicine*, 2020, vol. 52(7), pp. 604–611. doi: 10.1002/lsm.23196.
9. Grosenick D., Wabnitz H., Macdonald R. Diffuse near-infrared imaging of tissue with picosecond time resolution, *Biomedical Engineering / Biomedizinische Technik*, 2018, vol. 63(5), pp. 511–518. doi: 10.1515/bmt-2017-0067.
10. Rejmstad P., Johansson J. D., Haj-Hosseini N. et al. A method for monitoring of oxygen saturation changes in brain tissue using diffuse reflectance spectroscopy, *Journal of Biophotonics*, 2017, vol. 10(3), pp. 446–455. doi: 10.1002/jbio.201500334.
11. Skyrman S., Burström G., Lai M. et al. Diffuse reflectance spectroscopy sensor to differentiate between glial tumor and healthy brain tissue: a proof-of-concept study, *Biomedical Optics Express*, 2022, vol. 13(12), pp. 6470. doi: 10.1364/BOE.474344.
12. Li K., Wu Q., Feng S. et al. In situ detection of human glioma based on tissue optical properties using diffuse reflectance spectroscopy, *Journal of Biophotonics*, 2023, vol. 16(11), pp. e202300195. doi: 10.1002/jbio.202300195.
13. Potapov A. A., Goriaĭnov S. A., Loshchenov V. B. et al. Intraoperative combined spectroscopy (optical biopsy) of cerebral gliomas, *Zhurnal Voprosy Neirokhirurgii Imeni N.N. Burdenko*, 2013, vol. 77(2), pp. 3–10.
14. Romanishkin I., Savelieva T., Kosyrkova A. et al. Differentiation of glioblastoma tissues using spontaneous Raman scattering with dimensionality reduction and data classification, *Frontiers in Oncology*, 2022, vol. 12, pp. 944210. doi: 10.3389/fonc.2022.944210.
15. Ospanov A., Romanishkin I., Savelieva T. et al. Optical Differentiation of Brain Tumors Based on Raman Spectroscopy and Cluster Analysis Methods, *International Journal of Molecular Sciences*, 2023, vol. 24(19), pp. 14432. doi: 10.3390/ijms241914432.
16. Romanishkin I. D., Savelieva T. A., Ospanov A. et al. Classification of intracranial tumors based on optical-spectral analysis, *Biomedical Photonics*, 2023, vol. 12(3), pp. 4–10. doi: 10.24931/2413-9432-2023-12-3-4-10.
17. Stratonnikov A. A., Meerovich G. A., Ryabova A. V. et al. Application of backward diffuse reflection spectroscopy for monitoring the state of tissues in photodynamic therapy, *Quantum Electronics*, 2006, vol. 36(12), pp. 1103–1110. doi: 10.1070/QE2006v036n12ABEH013331.
18. Pominova D. V., Ryabova A. V., Skobeltsin A. S. et al. Spectroscopic study of methylene blue *in vivo*: effects on tissue oxygenation and tumor metabolism, *Biomedical Photonics*, 2023, vol. 12(1), pp. 4–13. doi: 10.24931/2413-9432-2023-12-1-4-13.
19. Jacques S. L., Pogue B. W. Tutorial on diffuse light transport, *Journal of Biomedical Optics*, 2008, vol. 13(4), pp. 041302. doi: 10.1117/1.2967535.
20. Bohren C. F., Huffman D. R. Absorption and Scattering of Light by Small Particles / C. F. Bohren, D. R. Huffman, 1 ed., Wiley, 1998. doi: 10.1002/9783527618156.
21. Wang L., Jacques S. L., Zheng L. MCML—Monte Carlo modeling of light transport in multi-layered tissues, *Computer Methods and Programs in Biomedicine*, 1995, vol. 47(2), pp. 131–146. doi: 10.1016/0169-2607(95)01640-F.

ЛИТЕРАТУРА

1. Vasefi F., MacKinnon N., Farkas D. L. et al. Review of the potential of optical technologies for cancer diagnosis in neurosurgery: a step toward intraoperative neurophotonics // Neurophotonics. – 2016. – Vol. 4. – № 1. – P. 011010.doi: 10.1117/1.NPh.4.1.011010.
2. Goryaynov S. A., Okhlopkov V. A., Golbin D. A. et al. Fluorescence Diagnosis in Neurooncology: Retrospective Analysis of 653 Cases // Frontiers in Oncology. – 2019. – Vol. 9. – P. 830.doi: 10.3389/fonc.2019.00830.
3. Goryaynov S. A., Buklina S. B., Khapov I. V. et al. 5-ALA-guided tumor resection during awake speech mapping in gliomas located in eloquent speech areas: Single-center experience // Frontiers in Oncology. – 2022. – Vol. 12. – P. 940951.doi: 10.3389/fonc.2022.940951.
4. Rynda A. Yu., Olyushin V. E., Rostovtsev D. M. et al. Fluorescent diagnostics with chlorin e6 in surgery of low-grade glioma // Biomedical Photonics. – 2021. – Vol. 10. – № 4. – P. 35–43.doi: 10.24931/2413-9432-2021-10-4-35-43.
5. Rynda A. Yu., Olyushin V. E., Rostovtsev D. M. et al. Results of microsurgical resection of glioblastomas under endoscopic and fluorescent control // Biomedical Photonics. – 2024. – Vol. 13. – № 3. – P. 20–30.doi: 10.24931/2413-9432-2024-13-3-20-30.
6. Udeneev A. M., Kalyagina N. A., Reps V. F. et al. Photo and spectral fluorescence analysis of the spinal cord injury area in animal models // Biomedical Photonics. – 2023. – Vol. 12. – № 3. – P. 15–20.doi: 10.24931/2413-9432-2023-12-3-16-20.
7. Liu Y.-X., Yang Y.-S. Using Diffuse Reflectance Spectroscopy to Classify Tumor Tissue in Upper Gastrointestinal Cancers // JAMA Surgery. – 2023. – Vol. 158. – № 7. – P. 772.doi: 10.1001/jamasurg.2022.8430.
8. Baltussen E. J. M., Brouwer De Koning S. G., Sanders J. et al. Using Diffuse Reflectance Spectroscopy to Distinguish Tumor Tissue From Fibrosis in Rectal Cancer Patients as a Guide to Surgery // Lasers in Surgery and Medicine. – 2020. – Vol. 52. – № 7. – P. 604–611.doi: 10.1002/lsm.23196.
9. Grosenick D., Wabnitz H., Macdonald R. Diffuse near-infrared imaging of tissue with picosecond time resolution // Biomedical Engineering / Biomedizinische Technik. – 2018. – Vol. 63. – № 5. – P. 511–518.doi: 10.1515/bmt-2017-0067.
10. Rejmstad P., Johansson J. D., Haj-Hosseini N. et al. A method for monitoring of oxygen saturation changes in brain tissue using diffuse reflectance spectroscopy // Journal of Biophotonics. – 2017. – Vol. 10. – № 3. – P. 446–455.doi: 10.1002/jbio.201500334.
11. Skyrman S., Burström G., Lai M. et al. Diffuse reflectance spectroscopy sensor to differentiate between glial tumor and healthy brain tissue: a proof-of-concept study // Biomedical Optics Express. – 2022. – Vol. 13. – № 12. – P. 6470.doi: 10.1364/BOE.474344.
12. Li K., Wu Q., Feng S. et al. In situ detection of human glioma based on tissue optical properties using diffuse reflectance spectroscopy // Journal of Biophotonics. – 2023. – Vol. 16. – № 11. – P. e202300195.doi: 10.1002/jbio.202300195.
13. Potapov A. A., Goriaĭnov S. A., Loshchenov V. B. et al. Intraoperative combined spectroscopy (optical biopsy) of cerebral gliomas // Zhurnal Voprosy Neirokhirurgii Imeni N.N. Burdenko. – 2013. – Vol. 77. – № 2. – P. 3–10.
14. Romanishkin I., Savelieva T., Kosyrkova A. et al. Differentiation of glioblastoma tissues using spontaneous Raman scattering with dimensionality reduction and data classification // Frontiers in Oncology. – 2022. – Vol. 12. – P. 944210.doi: 10.3389/fonc.2022.944210.
15. Ospanov A., Romanishkin I., Savelieva T. et al. Optical Differentiation of Brain Tumors Based on Raman Spectroscopy and Cluster Analysis Methods // International Journal of Molecular Sciences. – 2023. – Vol. 24. – № 19. – P. 14432.doi: 10.3390/ijms241914432.
16. Romanishkin I. D., Savelieva T. A., Ospanov A. et al. Classification of intracranial tumors based on optical-spectral analysis // Biomedical Photonics. – 2023. – Vol. 12. – № 3. – P. 4–10.doi: 10.24931/2413-9432-2023-12-3-4-10.
17. Stratonnikov A. A., Meerovich G. A., Ryabova A. V. et al. Application of backward diffuse reflection spectroscopy for monitoring the state of tissues in photodynamic therapy // Quantum Electronics. – 2006. – Vol. 36. – № 12. – P. 1103–1110.doi: 10.1070/QE2006v036n12ABEH013331.
18. Pominova D. V., Ryabova A. V., Skobeltsin A. S. et al. Spectroscopic study of methylene blue *in vivo*: effects on tissue oxygenation and tumor metabolism // Biomedical Photonics. – 2023. – Vol. 12. – № 1. – P. 4–13.doi: 10.24931/2413-9432-2023-12-1-4-13.
19. Jacques S. L., Pogue B. W. Tutorial on diffuse light transport // Journal of Biomedical Optics. – 2008. – Vol. 13. – № 4. – P. 041302.doi: 10.1117/1.2967535.
20. Bohren C. F., Huffman D. R. Absorption and Scattering of Light by Small Particles / C. F. Bohren, D. R. Huffman, 1., Wiley, 1998.doi: 10.1002/9783527618156.
21. Wang L., Jacques S. L., Zheng L. MCML—Monte Carlo modeling of light transport in multi-layered tissues // Computer Methods and Programs in Biomedicine. – 1995. – Vol. 47. – № 2. – P. 131–146.doi: 10.1016/0169-2607(95)01640-F.

22. Evolution of the Molecular Biology of Brain Tumors and the Therapeutic Implications ed. T. Lichtor, InTech, 2013. doi: 10.5772/50198.
23. Giese A., Bjerkvig R., Berens M. E. et al. Cost of Migration: Invasion of Malignant Gliomas and Implications for Treatment, *Journal of Clinical Oncology*, 2003, vol. 21(8), pp. 1624–1636. doi: 10.1200/JCO.2003.05.063.
24. Wang S., Meng M., Zhang X. et al. Texture analysis of diffusion weighted imaging for the evaluation of glioma heterogeneity based on different regions of interest, *Oncology Letters*, 2018 doi: 10.3892/ol.2018.8232.
25. Brunberg J. A., Chenevert T. L., McKeever P. E. et al. *In vivo* MR determination of water diffusion coefficients and diffusion anisotropy: correlation with structural alteration in gliomas of the cerebral hemispheres, *AJNR. American journal of neuroradiology*, 1995, vol. 16(2), pp. 361–371.
26. Sinha S., Bastin M. E., Whittle I. R. et al. Diffusion tensor MR imaging of high-grade cerebral gliomas, *AJNR. American journal of neuroradiology*, 2002, vol. 23(4), pp. 520–527.
27. Johansen-Berg H., Behrens T. E. J. Diffusion MRI: from quantitative measurement to in-vivo neuroanatomy / H. Johansen-Berg, T. E. J. Behrens, 1st ed ed., Amsterdam Boston: Elsevier/Academic Press, 2009.
28. Basic neurochemistry: principles of molecular, cellular, and medical neurobiology ed. S. T. Brady, G. J. Siegel, R. W. Albers et al., 8th ed ed., Amsterdam: Academic Press, 2012. 1 c.
29. Le Bihan D., Mangin J., Poupon C. et al. Diffusion tensor imaging: Concepts and applications, *Journal of Magnetic Resonance Imaging*, 2001, vol. 13(4), pp. 534–546. doi: 10.1002/jmri.1076.
30. Lu S., Ahn D., Johnson G. et al. Peritumoral diffusion tensor imaging of high-grade gliomas and metastatic brain tumors, *AJNR. American journal of neuroradiology*, 2003, vol. 24(5), pp. 937–941.
31. Goebell E., Paustenbach S., Vaeterlein O. et al. Low-Grade and Anaplastic Gliomas: Differences in Architecture Evaluated with Diffusion-Tensor MR Imaging, *Radiology*, 2006, vol. 239(1), pp. 217–222. doi: 10.1148/radiol.2383050059.
32. Cotter D., Mackay D., Landau S. et al. Reduced Glial Cell Density and Neuronal Size in the Anterior Cingulate Cortex in Major Depressive Disorder, *Archives of General Psychiatry*, 2001, vol. 58(6), pp. 545. doi: 10.1001/archpsyc.58.6.545.
33. Spacek J. Atlas of Ultrastructural Neurocytology at SynapseWeb [Website]. URL: https://synapseweb.clm.utexas.edu/atlas (accessed: 18.11.2024).
34. Cruz-Sánchez F. F., Ferreres J. C., Figols J. et al. Prognostic analysis of astrocytic gliomas correlating histological parameters with the proliferating cell nuclear antigen labelling index (PCNA-LI), *Histology and Histopathology*, 1997, vol. 12(1), pp. 43–49.
35. Nafe R., Schlote W. Densitometric Analysis of Tumor Cell Nuclei in lowgrade and high-grade Astrocytomas, *Electronic Journal of Pathology and Histology*, 2002, vol. 8(3).
36. Candolfi M., Curtin J. F., Nichols W. S. et al. Intracranial glioblastoma models in preclinical neuro-oncology: neuropathological characterization and tumor progression, *Journal of Neuro-Oncology*, 2007, vol. 85(2), pp. 133–148. doi: 10.1007/s11060-007-9400-9.
37. Nafe R., Herminghaus S., Pilatus U. et al. Morphology of proliferating and non-proliferating tumor cell nuclei in glioblastomas correlates with preoperative data from proton-MR-spectroscopy, *Neuropathology*, 2004, vol. 24(3), pp. 172–182. doi: 10.1111/j.1440-1789.2004.00547.x.
38. Schiffer Astrocytic Tumors I Berlin/Heidelberg: Springer-Verlag, 2006.p. 27–58. doi: 10.1007/1-4020-3998-0_5.
39. Sarkar C., Jain A., Suri V. Current concepts in the pathology and genetics of gliomas, *Indian Journal of Cancer*, 2009, vol. 46(2), pp. 108. doi: 10.4103/0019-509X.49148.
40. Pysh J. J., Khan T. Variations in mitochondrial structure and content of neurons and neuroglia in rat brain: An electron microscopic study, *Brain Research*, 1972, vol. 36(1), pp. 1–18. doi: 10.1016/0006-8993(72)90762-7.
41. Beauvoit B., Evans S. M., Jenkins T. W. et al. Correlation Between the Light Scattering and the Mitochondrial Content of Normal Tissues and Transplantable Rodent Tumors, *Analytical Biochemistry*, 1995, vol. 226(1), pp. 167–174. doi: 10.1006/abio.1995.1205.
42. Beauvoit B., Kitai T., Chance B. Contribution of the mitochondrial compartment to the optical properties of the rat liver: a theoretical and practical approach, *Biophysical Journal*, 1994, vol. 67(6), pp. 2501–2510. doi: 10.1016/S0006-3495(94)80740-4.
43. Beauvoit B., Chance B. Time-Resolved Spectroscopy of mitochondria, cells and tissues under normal and pathological conditions, *Molecular and Cellular Biochemistry*, 1998, vol. 184(1/2), pp. 445–455. doi: 10.1023/A:1006855716742.
44. Schmitt J. M., Kumar G. Turbulent nature of refractive-index variations in biological tissue, *Optics Letters*, 1996, vol. 21(16), pp. 1310. doi: 10.1364/OL.21.001310.

22. Evolution of the Molecular Biology of Brain Tumors and the Therapeutic Implications ed. T. Lichtor, InTech, 2013.doi: 10.5772/50198.
23. Giese A., Bjerkvig R., Berens M. E. et al. Cost of Migration: Invasion of Malignant Gliomas and Implications for Treatment // Journal of Clinical Oncology. – 2003. – Vol. 21. – № 8. – P. 1624–1636.doi: 10.1200/JCO.2003.05.063.
24. Wang S., Meng M., Zhang X. et al. Texture analysis of diffusion weighted imaging for the evaluation of glioma heterogeneity based on different regions of interest // Oncology Letters. – 2018.doi: 10.3892/ol.2018.8232.
25. Brunberg J. A., Chenevert T. L., McKeever P. E. et al. *In vivo* MR determination of water diffusion coefficients and diffusion anisotropy: correlation with structural alteration in gliomas of the cerebral hemispheres // AJNR. American journal of neuroradiology. – 1995. – Vol. 16. – № 2. – P. 361–371.
26. Sinha S., Bastin M. E., Whittle I. R. et al. Diffusion tensor MR imaging of high-grade cerebral gliomas // AJNR. American journal of neuroradiology. – 2002. – Vol. 23. – № 4. – P. 520–527.
27. Johansen-Berg H., Behrens T. E. J. Diffusion MRI: from quantitative measurement to in-vivo neuroanatomy / H. Johansen-Berg, T. E. J. Behrens, 1st ed., Amsterdam Boston: Elsevier/Academic Press, 2009.
28. Basic neurochemistry: principles of molecular, cellular, and medical neurobiology ed. S. T. Brady, G. J. Siegel, R. W. Albers et al., 8th ed., Amsterdam: Academic Press, 2012. 1 c.
29. Le Bihan D., Mangin J., Poupon C. et al. Diffusion tensor imaging: Concepts and applications // Journal of Magnetic Resonance Imaging. – 2001. – Vol. 13. – № 4. – P. 534–546.doi: 10.1002/jmri.1076.
30. Lu S., Ahn D., Johnson G. et al. Peritumoral diffusion tensor imaging of high-grade gliomas and metastatic brain tumors // AJNR. American journal of neuroradiology. – 2003. – Vol. 24. – № 5. – P. 937–941.
31. Goebell E., Paustenbach S., Vaeterlein O. et al. Low-Grade and Anaplastic Gliomas: Differences in Architecture Evaluated with Diffusion-Tensor MR Imaging // Radiology. – 2006. – Vol. 239. – № 1. – P. 217–222.doi: 10.1148/radiol.2383050059.
32. Cotter D., Mackay D., Landau S. et al. Reduced Glial Cell Density and Neuronal Size in the Anterior Cingulate Cortex in Major Depressive Disorder // Archives of General Psychiatry. – 2001. – Vol. 58. – № 6. – P. 545.doi: 10.1001/archpsyc.58.6.545.
33. Spacek J. Atlas of Ultrastructural Neurocytology at SynapseWeb [Электронный ресурс]. URL: https://synapseweb.clm.utexas.edu/atlas (accessed: 18.11.2024).
34. Cruz-Sánchez F. F., Ferreres J. C., Figols J. et al. Prognostic analysis of astrocytic gliomas correlating histological parameters with the proliferating cell nuclear antigen labelling index (PCNA-LI) // Histology and Histopathology. – 1997. – Vol. 12. – № 1. – P. 43–49.
35. Nafe R., Schlote W. Densitometric Analysis of Tumor Cell Nuclei in lowgrade and high-grade Astrocytomas // Electronic Journal of Pathology and Histology. – 2002. – Vol. 8. – № 3.
36. Candolfi M., Curtin J. F., Nichols W. S. et al. Intracranial glioblastoma models in preclinical neuro-oncology: neuropathological characterization and tumor progression // Journal of Neuro-Oncology. – 2007. – Vol. 85. – № 2. – P. 133–148.doi: 10.1007/s11060-007-9400-9.
37. Nafe R., Herminghaus S., Pilatus U. et al. Morphology of proliferating and non-proliferating tumor cell nuclei in glioblastomas correlates with preoperative data from proton-MR-spectroscopy // Neuropathology. – 2004. – Vol. 24. – № 3. – P. 172–182.doi: 10.1111/j.1440-1789.2004.00547.x.
38. Schiffer Astrocytic Tumors I Berlin/Heidelberg: Springer-Verlag, 2006. C. 27–58.doi: 10.1007/1-4020-3998-0_5.
39. Sarkar C., Jain A., Suri V. Current concepts in the pathology and genetics of gliomas // Indian Journal of Cancer. – 2009. – Vol. 46. – № 2. – P. 108. doi: 10.4103/0019-509X.49148.
40. Pysh J. J., Khan T. Variations in mitochondrial structure and content of neurons and neuroglia in rat brain: An electron microscopic study // Brain Research. – 1972. – Vol. 36. – № 1. – P. 1–18. doi: 10.1016/0006-8993(72)90762-7.
41. Beauvoit B., Evans S. M., Jenkins T. W. et al. Correlation Between the Light Scattering and the Mitochondrial Content of Normal Tissues and Transplantable Rodent Tumors // Analytical Biochemistry. – 1995. – Vol. 226. – № 1. – P. 167–174.doi: 10.1006/abio.1995.1205.
42. Beauvoit B., Kitai T., Chance B. Contribution of the mitochondrial compartment to the optical properties of the rat liver: a theoretical and practical approach // Biophysical Journal. – 1994. – Vol. 67. – № 6. – P. 2501–2510.doi: 10.1016/S0006-3495(94)80740-4.
43. Beauvoit B., Chance B. Time-Resolved Spectroscopy of mitochondria, cells and tissues under normal and pathological conditions // Molecular and Cellular Biochemistry. – 1998. – Vol. 184. – № 1/2. – P. 445–455.doi: 10.1023/A:1006855716742.
44. Schmitt J. M., Kumar G. Turbulent nature of refractive-index variations in biological tissue // Optics Letters. – 1996. – Vol. 21. – № 16. – P. 1310. doi: 10.1364/OL.21.001310.

EFFECT OF NON-INVASIVE FRACTIONAL PHOTOTHERMOLYSIS ON THE EFFICACY OF TRANSDERMAL PHOTOSENSITIZATION IN THE EXPERIMENT *IN VIVO*

Chernopyatov D.I.[1], Bgatova N.P.[1], Nikonov S.D.[2], Nimaev V.V.[1]
[1]Research Institute of Clinical and Experimental Lymphology – Branch of the Institute of Cytology and Genetics, Siberian Branch of Russian Academy of Sciences, Novosibirsk, Russia
[2]Novosibirsk Tuberculosis Research Institute, Novosibirsk, Russia

Abstract

In an *in vivo* pilot study, the efficiency of noninvasive fractional laser photothermolysis (NFLP) as a transdermal system for application photosensitization of mouse skin before photodynamic therapy (PDT) was studied. For NFLP, a laser (λ = 970 nm) with an average power of 4 W and a pulse frequency of 50 Hz was used. An area of the skin of the anterior abdominal wall of mice was irradiated. After NFLP, a photosensitizer (PS) based on chlorin e6 in the form of a gel (0.5%) was applied to the skin with an application time of 30 min. Then, laser PDT (λ = 662 nm) was performed with a power of 2 W in a scanning pulse-periodic mode with a frequency of 5 Hz and a light spot area on the skin of 1.2 mm^2. The results of histological examination, confocal and electron microscopy showed the features of transdermal distribution of chlorin e6 after NFLP. PS fluoresces in all skin layers and the subcutaneous fat layer, indicating its deep penetration into the hypodermis after NFLP compared to conventional cutaneous application. The advantages of NFLP as a transport system for successful penetration of the gel form of chlorin e6 through all skin layers are demonstrated. Electron microscopy showed transdermal transport of PS in the form of nanosized microspheres and particles absorbed by macrophages and fibroblasts. It was also shown for the first time that pulsed PDT after NFLP leads to the formation of nanosized foci of photodestruction up to the border of the reticular layer of the skin and the hypodermis.

Keywords: photothermolysis, transdermal drug transport, photosensitisation, chlorin e6, photodynamic therapy, fluorescence, confocal microscopy, electron microscopy, light microscopy.

Contacts: Chernopyatov D.I., e-mail: danila.chernopyatov@yandex.ru.

For citations: Chernopyatov D.I., Bgatova N.P., Nikonov S.D., Nimaev V.V. Effect of non-invasive fractional photothermolysis on the efficacy of transdermal photosensitization in the experiment *in vivo*, *Biomedical Photonics*, 2024, vol. 13, № 4, pp. 13–21. doi: 10.24931/2413–9432–2024–13–4–13–21

ВЛИЯНИЕ НЕИНВАЗИВНОГО ФРАКЦИОННОГО ФОТОТЕРМОЛИЗА НА ЭФФЕКТИВНОСТЬ ТРАНСДЕРМАЛЬНОЙ ФОТОСЕНСИБИЛИЗАЦИИ И ФОТОДИНАМИЧЕСКОЙ ТЕРАПИИ В ЭКСПЕРИМЕНТЕ *IN VIVO*

Д.И. Чернопятов[1], Н.П. Бгатова[1], С.Д. Никонов[2], В.В. Нимаев[1]
[1]Научно-исследовательский институт клинической и экспериментальной лимфологии – филиал Федерального государственного бюджетного научного учреждения «Федеральный исследовательский центр Институт цитологии и генетики Сибирского отделения Российской академии наук», Новосибирск, Россия
[2]Новосибирский научно-исследовательский институт туберкулёза, Новосибирск, Россия

Резюме

В пилотном исследовании *in vivo* изучена эффективность неинвазивного фракционного лазерного фототермолиза (НФЛФ), как трансдермальной системы для аппликационной фотосенсибилизации кожи мышей перед фотодинамической терапией (ФДТ). Для НФЛФ использовали лазер (λ = 970 нм) со средней мощностью 4 Вт и частотой импульсов 50 Гц. Проводили облучение участка кожи перед-

ней брюшной стенки мышей. После НФЛФ на кожу наносили фотосенсибилизатор (ФС) на основе хлорина е6 в виде геля (0,5 %) с временем аппликации 30 мин. Затем проводили лазерную ФДТ (λ = 662 нм) с мощностью 2 Вт в сканирующем импульсно-периодическом режиме с частотой 5 Гц и площадью светового пятна на коже 1,2 мм^2. Результаты гистологического исследования, конфокальной и электронной микроскопии показали особенности трансдермального распределения хлорина е6 после проведения НФЛФ. ФС флуоресцирует во всех слоях кожи и подкожно-жировом слое, что указывает на его глубокое проникновение в гиподерму после НФЛФ по сравнению с обычной накожной аппликацией. Продемонстрированы преимущества НФЛФ как транспортной системы для успешного проникновения гелевой формы хлорина е6 через все слои кожи. Электронная микроскопия показала трансдермальный транспорт ФС в виде наноразмерных микросфер и частиц, поглощаемых макрофагами и фибробластами. Также было впервые показано, что импульсная ФДТ после НФЛФ приводит к формированию наноразмерных очагов фотодеструкции вплоть до границы сетчатого слоя кожи и гиподермы.

Ключевые слова: фототермолиз, трансдермальный транспорт лекарств, фотосенсибилизация, хлорин е6, фотодинамическая терапия, флуоресценция, конфокальная микроскопия, электронная микроскопия, световая микроскопия.

Контакты: Чернопятов Д.И., e-mail: danila.chernopyatov@yandex.ru.

Для цитирования: Чернопятов Д.И., Бгатова Н.П., Никонов С.Д., Нимаев В.В. Влияние неинвазивного фракционного фототермолиза на эффективность трансдермальной фотосенсибилизации в эксперименте *in vivo* // Biomedical Photonics. – 2024. – Т. 13, № 4. – С. 13–21. doi: 10.24931/2413–9432–2024–13–4–13–21

Introduction

Photodynamic therapy (PDT) is a modern method of treating malignant neoplasms and precancerous conditions based on systemic and local administration of a photosensitizer (PS) and exposure to visible electromagnetic radiation in the presence of tissue oxygen. PS accumulates in pathological tissues and, under the influence of light of a certain wavelength, converts tissue oxygen into active oxygen species (ROS), which destroy pathologically altered cells (precancerous pathology, malignant neoplasms), bacteria and viruses [1-3].

The various effects of PDT include cell necrosis and apoptosis, vascular thrombosis, activation of the immune system and immunosuppression, stimulation of collagenogenesis, as well as antimicrobial and antiviral action. Owing to the development of laser and endoscopic equipment and the emergence of various PS, the range of PDT applications has expanded significantly in such areas as oncology, dermatology, cosmetology, gynecology, otolaryngology, dentistry, urology, ophthalmology and even the treatment of the new coronavirus infection [4-8].

The main goal of PDT of non-oncological diseases, in contrast to the treatment of malignant tumors, is the modulation of cellular functions by exposure to low-power light energy and low-dose PDT with anti-inflammatory, antimicrobial and reparative purposes. However, at present, there are no standardized protocols for PDT of non-oncological diseases [9, 10].

Over the past thirty years, three generations of PS have been developed for clinical use. Chlorin e6, which belongs to the second generation, is capable of generating ROS when irradiated with red light of 662 nm. Due to the hydrophobicity of chlorin e6 molecules, it can penetrate the peptide glycan layers of the walls of gram-positive bacteria, providing successful antimicrobial PDT, including against Mycobacterium tuberculosis [11-15].

Methods of local photosensitization, such as intradermal injection or application of gel forms of the drug, allow the accumulation of PS only in the case of a superficial location of the pathological lesion or for the purpose of reparative regeneration of the skin [16]. This makes PDT more targeted and reduces the risk of phototoxicity by reducing the dose of PS. However, deep penetration of PS is limited by the protective functions of the skin, which requires the development of new transdermal delivery systems (TDS) [17].

As an alternative, a new non-invasive version of fractional laser photothermolysis (FLP) is proposed as a TDS for skin photosensitization before the PDT procedure [18].

With NFLP, lasers with a wavelength of less than 2000 nm are used, emitting energy in pulses that leave the epidermis intact and, forming microthermal zones without destruction of the dermis, cause the synthesis of new collagen [19, 20].

Further efforts to develop minimally invasive phototherapeutic techniques with increased efficacy have led to the study of options combining FLP techniques with pulsed light therapy or with PDT with 5-aminolevulinic acid (5-ALA) [21].

Since the NFLP technology with a wavelength of λ = 970 nm has not previously been studied in relation to skin photosensitization with chlorin e6 for subsequent PDT procedures, we initiated an *in vivo* study of the features of the intradermal distribution of chlorin e6 when locally applied to healthy skin after NFLP.

Materials and Methods

Photosensitizer

The drug radachlorin (Rc) in the dosage form "RadaGel" (OOO "Radapharma", Moscow, Russia) containing sodium salt of chlorin e6, obtained from the chlorophyll of the alga Spirulina Plantensis using a patented method, was used as a photosensitizer.

Experiment. Animals

To study the intradermal distribution of Rc after NFLP, male HTAAAKR mice (SPF-vivarium nursery of the ICG SB RAS (Federal Research Center, Institute of Cytology and Genetics, Siberian Branch of the Russian Academy of Sciences, Novosibirsk, Russia) aged 3 months (n = 16) were used.

The studies were carried out in accordance with the requirements of Directive 2010/63/EU of the European Parliament and of the Council of the European Union on the protection of animals used for scientific purposes. The animals were kept on a standard diet with unlimited access to water and food. The experimental study protocol was approved at a meeting of the local ethics committee of the Research Institute of Clinical and Experimental Lymphology - branch of the ICG SB RAS on 08.07.2019 (protocol No. 151).

The animals were fixed in a supine position. A 1×1 cm area was selected on the shaved skin of the anterior abdominal wall of the animals, on which NFLP was performed using semiconductor laser "Lakhta Milon" (OOO "Kvalitek", Moscow, Russia) (λ = 970 nm) with an average power of 4 W in a scanning pulse-periodic mode with a pulse duration of 10 ms at a frequency of 50 Hz (t = 10 ms, f = 50 Hz) through a quartz-polymer light guide with a focusing lens (OOO "Polironic", Moscow, Russia). The diameter of the light spot at the focus was 1.2 mm, the energy dose density in the pulse was 25 J/cm^2. Fractional laser exposure to the skin lasted 30 s.

Rc in a concentration of 0.5% was applied with a sterile spatula at a dose of 0.1 g per 1 cm^2 of the selected skin area. The exposure of the drug on the skin was 30 min, after which its remains were removed with a sterile napkin.

PDT was performed with a "Lakhta Milon" semiconductor laser (OOO "Kvalitek", Moscow, Russia) (λ = 662 nm) and a power of 2 W in a scanning pulse-periodic mode with a laser pulse duration of 100 ms at a frequency of 5 Hz (t = 100 ms, f = 5 Hz) through an optical fiber with a lens focusing a light spot of 0.002 cm^2 on the skin, providing a laser energy density of 40 J/cm^2 on the tissue surface.

The animals were divided into 4 groups. Animals in the 1st group (n = 4) underwent NFLP of the abdominal wall skin. In the 2nd group (n = 4), similar preparation of the skin with NFLF was performed and Rc was applied. After 30 min, the remnants of PS were removed with a sterile napkin and PDT was performed. In the 3rd group (n = 4), Rc was applied to the skin of the animals for 30 min, then its remnants were removed with a napkin and PDT was performed. In the 4th group (n = 4), the shaved skin of the animals was not exposed to the effects.

After completion of the effects, euthanasia was performed by dislocation of the cervical vertebrae, then the anterior abdominal wall was excised and skin samples were prepared for histological examination, confocal and electron microscopy. The material was fixed in a 4% paraformaldehyde solution.

Confocal microscopy

Confocal microscopy was performed on cryosections of skin tissue. To prepare cryosections, skin samples were fixed with a 4% paraformaldehyde solution for 1 day, then washed with a cooled sodium phosphate buffer (PBS) solution and immersed in a 30% sucrose solution for 1 day. After that, the studied tissues were placed in foil with a TissueTek medium and frozen at -70°C.

Sections from frozen tissue were obtained on an HM 550OP cryostat (Zeiss, Germany) and prepared taking into account their transverse orientation for subsequent assessment of the depth of penetration of the PS. Images were obtained on a laser scanning microscope LSM 780 NLO AxioObserver Z1 (Zeiss, Germany) in the Collective Use Center for Microscopic Analysis of Biological Objects of the Institute of Cytology and Genetics SB RAS.

To analyze the fluorescence of PS in skin samples, confocal microscopy was performed with fluorescence excitation at a wavelength of λ = 458 nm. Fluorescence was recorded at a wavelength of λ = 675 nm. The images obtained by confocal microscopy were processed using the Zeiss Efficient Navigation (ZEN) 2010 microscope software. The recorded fluorescence values of the preparation were expressed in optical units (r.u.).

For each animal, the fluorescence value of optical sections in each skin layer was calculated using the microscope software. After that, the data for each individual were aggregated and calculations were performed.

Light and electron microscopy

To assess the structure of the epidermis, papillary and reticular layers of the skin, samples were prepared by fixing in a 4% paraformaldehyde solution prepared on Hanks' medium, then fixed for 1 hour in a 1% osmium tetroxide (OsO_4) solution on a phosphate buffer (pH = 7.4), dehydrated in ethyl alcohol of increasing concentration and embedded in Epon. Semi-thin sections of 1 μm thickness were obtained on a Leica EM UC7 ultramicrotome (Leica Microsystems, Germany), stained with toluidine blue and examined using a LEICA DME light microscope (Leica Microsystems, Germany). Digital micrographs were obtained using the AVerTV6 computer program.

For examination of skin samples in an electron microscope, ultrathin sections of 70-100 nm thickness were obtained using a Leica EM UC7 ultramicrotome (Leica Microsystems, Germany) and stained with uranyl acetate and lead citrate. Digital photographs of skin fragments were obtained at a magnification of ×30,000 with JEM 1400 electron microscope (JEOL, Tokyo, Japan) and analyzed using ImageJ software (National Institutes of Health, Bethesda, MD, USA). Microscopic analysis was

performed at the Multidisciplinary Center for Microscopy of Biological Objects at the Institute of Cytology and Genetics SB RAS (Novosibirsk, Russia).

Morphometry

Morphometric analysis of digital photographs of ultrathin skin sections (25 fields of view in each group at a magnification of x15,000) was performed using Image J software (Wayne Rasband, USA). The sizes of Rc in the cytoplasm of epithelial cells, fibroblasts and in the interstitium were determined.

Statistical processing

Since the study was preliminary and the number of samples in each group was 4 units, which does not allow making confident conclusions about the presence of observed patterns in the population regardless of the choice between parametric and nonparametric criteria, in order to indicate the direction for further work, it was decided to use sample means and standard deviations as descriptive statistics (and, accordingly, parametric criteria for intergroup comparisons), since it seems that for a given number of objects, such statistics will be a more visual and informative characteristic of the sample than the mode, median and interquartile range. The calculation of the average values of fluorescence intensity and standard deviation (μ, σ) in each group was performed using the Statistica v.10 program (Statsoft, USA). Pairwise comparisons of groups were performed using the Student's criterion.

Separately, it should be notet that we received an insignificant number of observations, and these results justify the need to conduct a study with a larger number of objects.

Statistical analysis of the data obtained when determining the size of Rc particles was performed using the Statistica v.10 computer program (Statsoft, USA). The Kolmogorov–Smirnov statistical test was used to check the variation series for normality. The results of the ultrastructural analysis did not meet the criteria for normal distribution, so the description of the quantitative characteristics is presented as a median and the first and third quartiles – Me (Q1; Q3).

Results

Confocal Microscopy

During confocal microscopy of skin samples from group 4 (control) and from group 1 after NFLP, we did not detect any obvious tissue fluorescence (Fig. 1A, B), and the numerical values of fluorescence intensity correspond to weak autofluorescence of endogenous chromophores, with the exception of all epidermis samples after NFLP, which were deprived of the ability to fluoresce due to photobleaching under the influence of pulsed infrared laser radiation of 970 nm (Table).

In groups 2 and 3, pronounced fluorescence was noted, which in group 2 was much more intense than in group 3 (Fig. 1). Evaluating the distribution of Rc in the skin layers by fluorescence intensity in numerical values of r.u., it was possible to determine that the maximum fluorescence in the skin samples in group 3 reached 2500 r.u. in the epidermal layer and sharply decreased to 600 r.u. at the border of the reticular layer.

Micrographs of skin samples in group 2, obtained after NFLP with subsequent application photosensitization of Rc, demonstrate an increase in the transdermal distribution of PS, which is confirmed by fluorescence in all layers of the skin with the highest intensity in the epidermal and papillary layers.

Thus, in the epidermal layer, the maximum possible fluorescence intensity value for recording by a microscope was recorded at 4095 r.u., which turned out to be 1.7 times greater than in group 3 with conventional application of PS. At the border of the epidermal and reticular layers, the fluorescence intensity reached 2000 r.u., which exceeded the maximum values in the third group by 3.3 times.

It should be noted that after NFLP with application photosensitization, deeper penetration of Rc into the hypodermis occurs, where fluorescence up to 500 r.u. is preserved, also spreading in the subcutaneous fat layer (Fig. 1D).

This fact confirms the property of non-invasive pulsed laser energy at a wavelength of 970 nm, focused on the epidermis, to increase the transport of chlorine series PS through all layers of the skin in 30 minutes of application exposure of the drug.

The aggregate data on the comparative quantitative characteristics of the fluorescence intensity of the skin

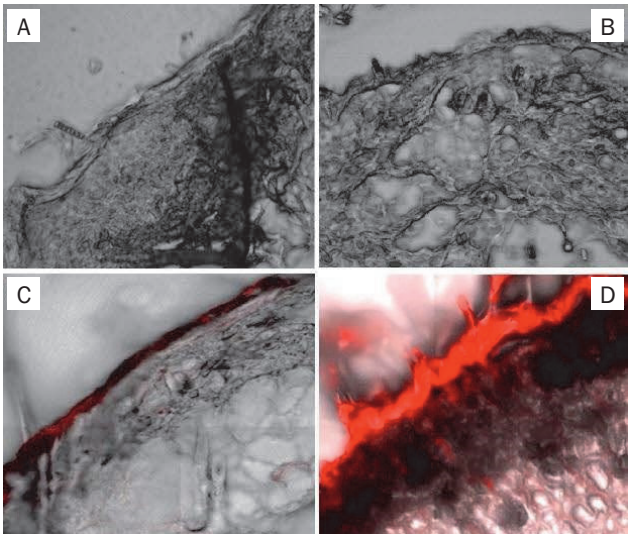

Рис. 1. Конфокальная микроскопия образцов кожи: A – контроль (группа 4); B – НФЛФ (группа 1); C – ФС+ФДТ (группа 3); D – НФЛФ+ФС+ФДТ (группа 2).
Fig. 1. Confocal microscopy of skin samples: A – control (group 4);. B – NFLP (group 1); C – PS +PDT (group 3); D – NFLP+PS+PDT (group 2).

Таблица
Интенсивность флуоресценции слоёв кожи исследуемых групп
Table
Fluorescence intensity of skin layers in the studied groups

Группы Groups	Воздействие Impact	Интенсивность флуоресценции Fluorescence intensity			
		Эпидермис + сосочковый слой (о.е.) Epidermis + papillary layer (o.u.) μ,σ	Сетчатый слой (о.е.) The mesh layer (o.u.) μ,σ	Гиподерма (о.е.) Hypoderma (o.u.) μ,σ	Все слои (о.е.) All layers (o.u.) μ,σ
1 (n = 4)	НФЛФ NFLP	0	2,74; 1,32	3,13; 1,77	2,8; 1,06
2 (n = 4)	НФЛФ + ФС + ФДТ NFLP+PS+PDT	3487,56; 150,64*	140,22; 16,48*	16,03; 2,78	240,35; 26,45*
3 (n = 4)	ФС + ФДТ PS+PDT	633,38; 92,31*	22,68; 4,77*	9,76; 1,75	41,44; 6,15*
4 (n = 4)	Контроль Control	7,36; 6,23	0,98; 0,61	0	1,5; 0,69

*p < 0,05

layers of the studied groups are presented in the form of a table. At $p < 0.05$, significant differences from the control group were noted.

Comparison of the results of skin photosensitization demonstrates obvious advantages of preliminary NFLP, which creates conditions for the penetration of chlorin e6 through all layers of the dermis to the subcutaneous fat layer, which was confirmed by an increase in the fluorescence intensity of PS in all layers by 5.8 times, in the papillary layer by 5 times, in the reticular layer by 6 times (table).

Light Microscopy

Light microscopy examination of skin samples allowed to register the peculiarity of structural changes in the compared groups that occur under the influence of non-invasive laser energy pulses focused on the stratum corneum.

Comparing the control samples from group 4 with the samples from group 1, we were convinced that after NFLP there were no thermal damages and the differentiation and cellular composition of the epidermis were preserved, but after non-invasive laser exposure there was a compaction of the papillary layer of the skin and edema of the reticular layer (Fig. 2B).

In group 3, after pulsed PDT, there was a significant compaction of the papillary and reticular layers with a violation of their differentiation (Fig. 2C).

Exposure of the skin to NFLP followed by pulsed PDT in the second group led to compaction of the reticular layer of the skin while maintaining the differentiation and cellular composition of the epidermis (Fig. 2D).

Thus, according to light microscopy data, the presented variants of laser energy effects, devoid of damaging effects on the skin, have a number of different effects, represented by compaction of only the papillary

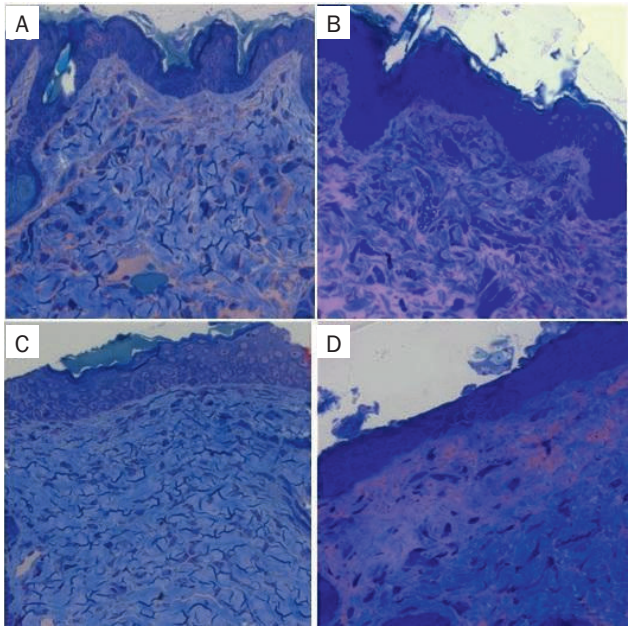

Рис. 2. Световая микроскопия (увеличение x400, окраска толуидиновым синим): A – контроль (группа 4); B – после НФЛФ (группа 1); C – после ФДТ+ФС (группа 3); D – после НФЛФ+ФС+ФДТ (группа 2).
Fig. 2. Light microscopy (magnification x400, stained with toluidine blue): A – control (group 4); B – after NFLP (group 1); C – after PDT+PS (group 3); D – after NFLP +PS+PDT (group 2).

layer after NFLP, deeper compaction of the papillary and reticular layers after PDT, and the deepest compaction of the reticular layer after a combination of NFLP with subsequent PDT.

Electron microscopy

Electron microscopy allowed to characterize the changes in the skin after non-invasive laser treatment at the ultrastructural level, to see the features of the extra- and intracellular distribution of Rc in the skin structures, and to confirm the passage of laser energy through all layers of the skin by the photodynamic reactions that took place.

In group 1, after NFLP without the use of PS, we noted the compaction of epithelial cells, the papillary layer and structures located on the border of the papillary and reticular layers of the skin (Fig. 3C, D).

In animals of group 3, after cutaneous application of Rc, its uneven distribution in the skin layers was recorded in the form of spherical particles with an average size of 536.0 (436.0; 668.5) nm. The maximum accumulation of the drug occurred in the epithelial layer (Fig. 4A).

When assessing the effects of pulsed PDT in group 3, a relatively low density of formation of foci of photodestruction in the epithelium and papillary layer of the dermis was noted with a high density of Rc particles absorbed by epithelial cells.

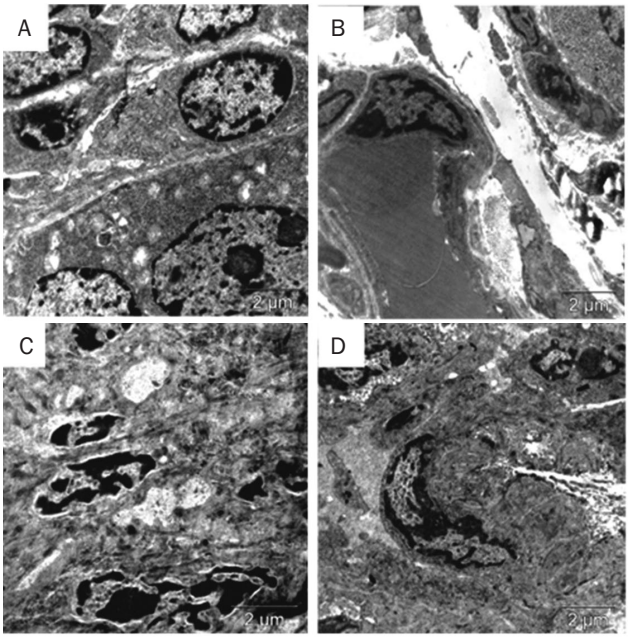

Рис. 3. Ультраструктурная организация кожи животных в контроле и после НФЛФ, электронная микроскопия: A-B – контроль (группа 4); A – ультраструктура эпителия; B – структура сосочкового слоя дермы; C-D – после НФЛФ (группа 2); повышение плотности эпителия (C) и сосочкового слоя дермы (D).

Fig. 3. Ultrastructural organization of animal skin in control and after NFLP. Electron microscopy: A-B – control (group 4); A – ultrastructure of the epithelium; B – structure of the papillary dermis; C-D – after NFLP (group 2); increased density of the epithelium (C) and papillary dermis (D).

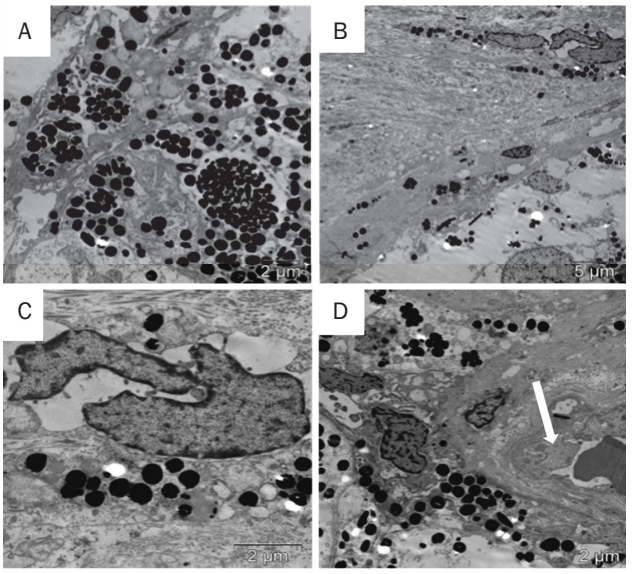

Рис. 4. Ультраструктурная организация кожи после аппликационной фотосенсибилизации ФС и последующей импульсной ФДТ (группа 3): A – накопление в эпителии массы интактных частиц ФС; B – наличие интактных частиц ФС и разрозненных очагов фотодеструкции; C – накопление ФС и очагов фотодеструкции в цитоплазме макрофага; D – частицы ФС находятся в сосочковом слое дермы и отсутствуют в цитоплазме эндотелия кровеносного сосуда (стрелка).

Fig. 4. Ultrastructural organization of the skin after application photosensitization with PS and subsequent pulsed PDT (Group 3): A – accumulation of a mass of intact PS; B – the presence of intact sl PS particles and isolated foci of photodestruction; C – PS and foci of photodestruction in the cytoplasm of the macrophage; D – PS particles are located in the papillary layer of the dermis and are absent in the cytoplasm of the endothelium of the blood vessel (arrow).

We believe that in this group of animals that did not receive preliminary NFLP, photodynamic effects are realized to a lesser extent due to the shielding of the energy of laser pulses absorbed by skin pigments and excess PS on the stratum corneum of the epidermis.

This assumption was confirmed after studying the results of electron microscopy of skin samples from group 2 mice after NFLP with application photosensitization and pulsed PDT.

We found that after NFLP, successful accumulation of Rc particles occurs in epithelial cells, and the subsequent photodynamic reaction is represented by a significant number of scattered vesicle-like foci of photodestruction with an average size of 681.0 (174.5; 1485.0) nm (Fig. 5A).

Similar in size and spherical shape, multiple foci of photodestruction were recorded in the interstitium of not only the papillary layer, but also in the reticular layer of the dermis (Fig. 5B, C).

The obtained data indicate that the preparation of the skin with NFLP significantly improves the penetration of Rc in the form of spherical microaggregates into all layers

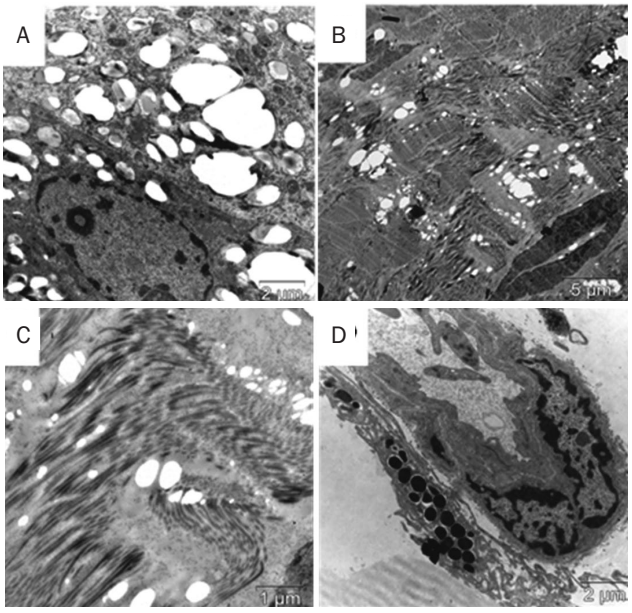

Рис. 5. Электронная микроскопия. Структура кожи в первый день после НФЛФ, аппликационной фотосенсибилизации ФС и импульсной ФДТ (группа 2): А – эпителий с множественными везикулоподобными очагами фотодеструкций; В и С – интерстиций сетчатого слоя дермы содержит скопления сферических очагов фотодеструкций; D – накопление частиц интактных микросфер ФС в цитоплазме фибробласта.
Fig. 5. Electron microscopy. Skin structure on the first day after NFLP, application photosensitization of PS and pulsed PDT (group 2): A – epithelium with multiple areas of photodamage, B and C – the interstitium of the reticular layer of the dermis contains clusters of spherical foci of photodestruction. D – accumulation of particles of intact PS microspheres in the cytoplasm of fibroblasts.

of the dermis, reaching the cytoplasm of the fibroblasts of the reticular layer at the border with the subcutaneous fat (Fig. 5D).

The effect of formation of multiple foci of photodestruction in the depth of the reticular layer in the hypodermis, characteristic only of cases from group 2 (Fig. 5C), indicates an increase in the efficiency of PDT after NFLP due to weakening of the epidermal shielding and compaction of the reticular layer (Fig. 2B, D), improving the light transmission of the skin, and an increase in the energy density of light pulses to levels that excite PS molecules to the triplet state in deeper layers of the skin.

Therefore, after NFLP, the energy of photons in the PDT process penetrates significantly deeper and, consequently, increases the medicinal activity of Rc in group 2 with the initially identical applied dose of PS in the compared groups 2 and 3.

An important fact is that we have recorded that by the beginning of the PDT procedure, PS does not move into the vascular sector of the intact skin and for this reason, microthrombosis of vessels, characteristic of PDT of tumors, is prevented (Fig. 4D).

Discussion

Local application of PS is associated with limitations due to the barrier function of the skin, especially the stratum corneum, which prevents their absorption. When PS is applied to healthy skin, the depth of its penetration is limited by the stratum corneum and does not exceed 12 ± 5 μm during 1 hour of cutaneous exposure [22].

In the search for optimal transdermal systems, non-ablative photothermolysis with a 1550 nm laser was successfully tested to increase the penetration of 5-ALA in PDT of acne [21]. As studies have shown, non-ablative laser techniques, devoid of invasiveness, minimally damage the stratum corneum [19,20,23].

In our study, we sought to find out whether non-invasive photothermolysis improves the penetration of PS into the deep layers of the skin and increases the effectiveness of PDT. The experiment was aimed at creating a multimodal effect on the skin using laser energy that improved light transmission and transdermal transport of PS with chlorin e6.

We chose laser radiation at a wavelength of 970 nm, focused on the stratum corneum with a pulse frequency of 50 Hz. This allowed to achieve partial damage to the stratum corneum, which weakened the reflection of energy during PDT and caused photobleaching of chromophores in the skin. The NFLP parameters ensured energy delivery through the lens, concentrating the power of 4 W in the focus on the epidermis without tissue coagulation, which led to photobiomodulation effects with activation of macrophages and fibroblasts for phagocytosis and transport of Rc granules.

The results showed that preliminary exposure to NFLP actually increases the depth of PS penetration in healthy skin without significant damage. Unlike traditional ablative FLP (AFLP), NFLP causes only point microtraumas, activating phagocytic cells that capture PS and transport it to the hypodermis.

The energy of the infrared laser pulse for traditional AFLP is such that it creates a column of damaged tissues to a certain depth, while the use of NFLP through a focusing lens leads only to the formation of a point light spot on the stratum corneum of the epidermis with subsequent scattering of the light beam in the deeper parts of the skin, which eliminates thermal damage.

Probably, pulsed laser action focused on the stratum corneum and epidermis, absorbed by skin pigments and hemoglobin in superficial capillaries and hair follicles, causes point microtraumas and secondary activation of phagocytic cells, which capture PS and actively transport it down to the hypodermis. The study is devoted to improving skin permeability using NFLP at a wavelength of $\lambda = 970$ nm for photosensitization in PDT.

Experiments on mice revealed features of Rc distribution when locally applied to skin prepared with NFLP. Although NFLP does not damage the epidermis,

confocal microscopy showed a loss of autofluorescence by the epidermis. This may indicate a photobleaching reaction of endogenous chromophores and an increase in the light transmission of the compacted epithelium.

Electron microscopy confirmed the increase in light transmission in the foci of photodestruction in the deep layers of the dermis revealed after PDT. Confocal microscopy showed an increase in the penetration of Rc into all layers of the dermis after the preparation of NFLP with an increase in its fluorescence intensity by 5.8 times. Electron microscopy demonstrated intradermal transport of Rc in the form of microspheres and their absorption by macrophages and fibroblasts, which is important for successful PDT.

Conclusion

We assume that NFLP activates the migration of phagocytic cells to the damaged area, which facilitates the transport of PS into the deep layers of the skin. Despite the demonstration of a new TDS for successful skin photosensitization, our study was not powerful enough to study the features of delayed skin reactions to pulsed PDT in the long-term period, which requires additional study.

Preliminary results of the pilot study emphasize the importance of studying tissue reactions to laser exposure at the micro level, which will open up new prospects for the use of NFLP as a transdermal system for drug delivery. We expect that the study will be useful for further development of PDT methods.

REFERENCES

1. Sviatchenko V.A., Nikonov S.D., Mayorov A.P., Gelfond M.L., Loktev V.B. Antiviral photodynamic therapy: Inactivation and inhibition of SARS-CoV-2 *in vitro* using methylene blue and Radachlorin. *Photodiagnosis and Photodynamic Therapy*, 2021, Vol. 33, p. 102112.
2. Wainwright M. Photosensitisers in biomedicine. *Chichester: John Wiley & Sons*, 2009.
3. Gunaydin G., Gedik M.E., Ayan S. Photodynamic therapy: Current limitations and novel approaches. *Frontiers in Chemistry*, 2021, Vol. 9, p. 691697.
4. Park Y.K., Park C.H. Clinical efficacy of photodynamic therapy. *Obstetrical & Gynecological Science*, 2016, Vol. 59 (6), pp. 479-488.
5. Awan M.A., Tarin S.A. Review of photodynamic therapy. *The Surgeon*, 2006, Vol. 4 (4), pp. 231-236.
6. Niculescu A.G., Grumezescu A.M. Photodynamic Therapy — An Up-to-Date Review. *Applied Sciences*, 2021, Vol. 11 (8), p. 3626.
7. Zakharenko A.A., Hamid A.H., Svechkova A.A., Belyaev M.A., Vovin K.N., Prudnikov A.V. The use of endoscopic photodynamic therapy in the complex treatment of malignant neoplasms of the stomach (literature review). *Bulletin of Surgery named after I.I. Grekov*, 2022, Vol. 181(4), pp. 5-12.
8. Kubrak T., Karakuła M., Czop M., Kawczyk-Krupka A., Aebisher D. Advances in Management of Bladder Cancer — The Role of Photodynamic Therapy. *Molecules*, 2022, Vol. 27 (4), p. 731.
9. Queirós C., Garrido P.M., Maia Silva J., Filipe P. Photodynamic therapy in dermatology: beyond current indications. *Dermatologic Therapy*, 2020, Vol. 33 (6), p. e13997.
10. Karrer S., Szeimies R.-M. Photodynamische Therapie Nichtonkologischer Indikationen. *Hautarzt*, 2007, Vol. 58 (7), pp. 585-596.
11. Van Straten D., Mashayekhi V., De Bruijn H. S., Oliveira S., Robinson D. J. Oncologic photodynamic therapy: Basic principles, current clinical status and future directions. *Cancers*, 2017, Vol. 9 (1), p. 19.
12. Hak A., Ali M.S., Sankaranarayanan S.A., Shinde V.R., Rengan A.K. Chlorin e6: a promising photosensitizer in photo-based cancer nanomedicine. *ACS Applied Bio Materials*, 2023, Vol. 6 (2), pp. 349-364.
13. Zhang D., Wu M., Zeng Y., Wu L., Wang Q., Han X., Liu X., Liu J. Chlorin e6 conjugated poly(dopamine) nanospheres as PDT/PTT dual-modal therapeutic agents for enhanced cancer therapy. *ACS Applied Materials & Interfaces*, 2015, Vol. 7 (15), pp. 8176-8187.
14. Bredikhin D.A., Nikonov S.D., Cherednichenko A.G., Petrenko T.I. Photodynamic inactivation of Mycobacterium tuberculosis with radachlorin *in vitro*. *Tuberculosis and lung diseases*, 2018, Vol. 96 (1), pp. 5-10.

ЛИТЕРАТУРА

1. Sviatchenko V.A., Nikonov S.D., Mayorov A.P., Gelfond M.L., Loktev V.B. Antiviral photodynamic therapy: Inactivation and inhibition of SARS-CoV-2 *in vitro* using methylene blue and Radachlorin // Photodiagnosis and Photodynamic Therapy. – 2021. – Vol. 33. – P. 102112.
2. Wainwright M. Photosensitisers in biomedicine // Chichester: John Wiley & Sons. – 2009.
3. Gunaydin G., Gedik M.E., Ayan S. Photodynamic therapy: Current limitations and novel approaches // Frontiers in Chemistry. – 2021. – Vol. 9. – P. 691697.
4. Park Y.K., Park C.H. Clinical efficacy of photodynamic therapy // Obstetrical & Gynecological Science. – 2016. – Vol. 59 (6). – P. 479-488.
5. Awan M.A., Tarin S.A. Review of photodynamic therapy // The Surgeon. – 2006. – Vol. 4 (4). – P. 231-236.
6. Niculescu A.G., Grumezescu A.M. Photodynamic Therapy — An Up-to-Date Review // Applied Sciences. – 2021. – Vol. 11 (8). – P. 3626.
7. Захаренко А.А., Хамид А.Х., Свечкова А.А., Беляев М.А., Вовин К.Н., Прудников А.В. Применение эндоскопической фотодинамической терапии в комплексном лечении злокачественных новообразований желудка (обзор литературы) // Вестник хирургии им. И.И. Грекова. – 2022. – Т. 181, № 4. – С. 5-12.
8. Kubrak T., Karakuła M., Czop M., Kawczyk-Krupka A., Aebisher D. Advances in Management of Bladder Cancer — The Role of Photodynamic Therapy // Molecules. – 2022. – Vol. 27 (4). – P. 731.
9. Queirós C., Garrido P.M., Maia Silva J., Filipe P. Photodynamic therapy in dermatology: beyond current indications // Dermatologic Therapy. – 2020. – Vol. 33 (6). – P. e13997.
10. Karrer S., Szeimies R.-M. Photodynamische Therapie Nichtonkologischer Indikationen // Hautarzt. – 2007. – Vol. 58 (7). – P. 585-596.
11. Van Straten D., Mashayekhi V., De Bruijn H. S., Oliveira S., Robinson D. J. Oncologic photodynamic therapy: Basic principles, current clinical status and future directions // Cancers. – 2017. – Vol. 9 (1). – P. 19.
12. Hak A., Ali M.S., Sankaranarayanan S.A., Shinde V.R., Rengan A.K. Chlorin e6: a promising photosensitizer in photo-based cancer nanomedicine // ACS Applied Bio Materials. – 2023. – Vol. 6 (2). – P. 349-364.
13. Zhang D., Wu M., Zeng Y., Wu L., Wang Q., Han X., Liu X., Liu J. Chlorin e6 conjugated poly(dopamine) nanospheres as PDT/PTT dual-modal therapeutic agents for enhanced cancer therapy // ACS Applied Materials & Interfaces. – 2015. – Vol. 7 (15). – P. 8176-8187.
14. Бредихин Д.А., Никонов С.Д., Чередниченко А.Г., Петренко Т.И. Фотодинамическая инактивация Mycobacterium tuberculosis радахлорином *in vitro* // Туберкулёз и болезни лёгких. – 2018. – Т. 96, № 1. – С. 5-10.

15. Mathur A., Parihar A. S., Modi S., Kalra A. Photodynamic therapy for ESKAPE pathogens: an emerging approach to combat antimicrobial resistance (AMR). *Microbial Pathogenesis*, 2023, Vol. 183, p. 106307.
16. Panova O.S., Dubensky V.V., Dubensky V.V., Petunina V.V., Beimanova M.A., Sanchez E.A., Gelfond M.L., Shilov B.V., Belkharoeva R.H. Photodynamic reparative regeneration of the skin using an external photosensitizer gel based on chloride e6. *Biomedical Photonics*, 2021, Vol. 10 (3), pp. 4-11.
17. Manstein D., Herron G.S., Sink R.K., Tanner H., Anderson R.R. Fractional photothermolysis: a new concept for cutaneous remodeling using microscopic patterns of thermal injury. *Lasers in Surgery and Medicine*, 2004, Vol. 34 (4). pp. 426-438.
18. Nimaev V.V., Nikonov S.D., Bredikhin D.A., Mayorov A.P., Chernopyatov D.I. Method of photodynamic therapy with intradermal photosensitization: patent for invention RU 2750975 C1. 07.07.2021. The application. No. 2020124765 07/15/2020; publ.07.07.2021.
19. Habbema L., Verhagen R., Van Hal R. et al. Minimally invasive non-thermal laser technology using laser-induced optical breakdown for skin rejuvenation. *Journal of Biophotonics*, 2012, Vol. 5(3–4), pp. 194-199.
20. Hædersdal M., Sakamoto F. H., Farinelli W. A., Doukas A. G., Tam J., Anderson R. R. Fractional CO2 laser-assisted drug delivery. *Lasers in Surgery and Medicine*, 2010, Vol. 42 (2), pp. 113-122.
21. Qureshi S., Lin J. Y. Utilizing non-ablative fractional photothermolysis prior to ALA-photodynamic therapy in the treatment of acne vulgaris: a case series. *Lasers in Medical Science*, 2017, Vol. 32, pp. 729-732.
22. Lohan S.B., Kröger M., Schleusener J., Darvin M.E., Lademann J., Streit I., Meinke M.C. Characterization of radical types, penetration profile and distribution pattern of the topically applied photosensitizer THPTS in porcine skin *ex vivo*. *European Journal of Pharmaceutics and Biopharmaceutics*, 2021, Vol. 162, pp. 50-58.
23. Laubach H. J., Tannous Z., Anderson R. R., Manstein D. Skin responses to fractional photothermolysis. *Lasers in Surgery and Medicine*, 2006, Vol. 38 (2), pp. 142-149.

15. Mathur A., Parihar A. S., Modi S., Kalra A. Photodynamic therapy for ESKAPE pathogens: an emerging approach to combat antimicrobial resistance (AMR) // Microbial Pathogenesis. – 2023. – Vol. 183. – P. 106307.
16. Панова О.С., Дубенский В.В., Дубенский В.В., Петунина В.В., Бейманова М.А., Санчес Э.А., Гельфонд М.Л., Шилов Б.В., Белхароева Р.Х. Фотодинамическая репаративная регенерация кожи с применением наружного геля-фотосенсибилизатора на основе хлорина е6 // Biomedical Photonics. – 2021. – Т. 10, № 3. – С. 4-11.
17. Manstein D., Herron G.S., Sink R.K., Tanner H., Anderson R.R. Fractional photothermolysis: a new concept for cutaneous remodeling using microscopic patterns of thermal injury // Lasers in Surgery and Medicine. – 2004. – Vol. 34 (4). – P. 426-438.
18. Нимаев В.В., Никонов С.Д., Бредихин Д.А., Майоров А.П., Чернопятов Д.И. Способ фотодинамической терапии с интрадермальной фотосенсибилизацией: патент на изобретение RU 2750975 C1. 07.07.2021. Заяв. № 2020124765 15.07.2020; опубл.07.07.2021.
19. Habbema L., Verhagen R., Van Hal R. et al. Minimally invasive non-thermal laser technology using laser-induced optical breakdown for skin rejuvenation // Journal of Biophotonics. – 2012. – Vol. 5(3–4). – P. 194-199.
20. Hædersdal M., Sakamoto F. H., Farinelli W. A., Doukas A. G., Tam J., Anderson R. R. Fractional CO2 laser-assisted drug delivery // Lasers in Surgery and Medicine. – 2010. – Vol. 42 (2). – P. 113-122.
21. Qureshi S., Lin J. Y. Utilizing non-ablative fractional photothermolysis prior to ALA-photodynamic therapy in the treatment of acne vulgaris: a case series // Lasers in Medical Science. – 2017. – Vol. 32. – P. 729-732.
22. Lohan S.B., Kröger M., Schleusener J., Darvin M.E., Lademann J., Streit I., Meinke M.C. Characterization of radical types, penetration profile and distribution pattern of the topically applied photosensitizer THPTS in porcine skin *ex vivo* // European Journal of Pharmaceutics and Biopharmaceutics. – 2021. – Vol. 162. – P. 50-58.
23. Laubach H. J., Tannous Z., Anderson R. R., Manstein D. Skin responses to fractional photothermolysis // Lasers in Surgery and Medicine. – 2006. – Vol. 38 (2). – P. 142-149.

ORIGINAL ARTICLES

DOXORUBICIN ENHANCES THE ANTITUMOR EFFICACY OF SONODYNAMIC THERAPY WITH PHOTOSENSITIZER PHOTOLON IN AN *IN VIVO* EXPERIMENT

Tzerkovsky D.A.[1], **Adamenko N.D.**[2]
[1]N.N. Alexandrov National Cancer of Belarus, Minsk, Republic of Belarus
[2]Vitebsk State University named after P.M. Masherov, Vitebsk, Republic of Belarus

Abstract

The antitumor effectiveness of sonodynamic therapy (SDT) with a chemotherapeutic drug and a photosensitizer (PS) of the chlorine series was studied in an *in vivo* experiment. The work was performed on 60 white nonlinear rats, divided into 2 series of 30 individuals each. Pliss lymphosarcoma, transplanted subcutaneously, was used as a tumor strain. Photolon was administered intravenously in a single dose of 2.5 mg/kg 2.5-3 hours before ultrasound exposure, and doxorubicin was administered intraperitoneally in a single dose of 5 mg/kg 0.5 hours before ultrasound exposure performed using the «Phyaction U» apparatus, generating radiation with a frequency of 1.04 MHz, intensities of 0.5 and 1.5 W/cm^2 and lasting 5 minute. The study groups in each series included 5 rats: control, ultrasound, doxorubicin, photolon + ultrasound, doxorubicin + ultrasound, photolon + doxorubicin + ultrasound. To assess antitumor effectiveness, criteria generally accepted in experimental oncology were used: average volume of tumors ($V_{av.}$, cm^3), absolute tumor growth rate (K, units), tumor growth inhibition coefficient (TGI, %), frequency of complete tumor regressions (CR, %), the average life expectancy of rats (ALE, days), the coefficient of increase in the average life expectancy of rats (%) and the median overall survival (days). Differences were considered statistically significant at a significance level of $p<0.05$. In the first and second series of experiments, the most effective modes were the use of photolon, doxorubicin and ultrasound with a frequency of 1.04 MHz and intensities of 0.5 and 1.5 W/cm^2, respectively. The proposed combination of therapeutic interventions made it possible to statistically significantly ($p<0.05$) increase the indicators of TGI, PR and ALE compared to the control and each of the components of the method separately. SDT methods developed and tested in *in vivo* experiments are characterized by high antitumor efficacy.

Keywords: Pliss lymphosarcoma, doxorubicin, photolon, ultrasound, sonodynamic therapy.

Contacts: Tzerkovsky D.A., tzerkovsky@mail.ru.

For citations: Tzerkovsky D.A., Adamenko N.D. Doxorubicin enhanced the antitumor efficacy of sonodynamic therapy with photosensitizer photolon in an *in vivo* experiment, *Biomedical Photonics*, 2024, vol. 13, № 4, pp. 22–32. doi: 10.24931/2413–9432–2024–13–4–22–32

СОНОДИНАМИЧЕСКАЯ ТЕРАПИЯ С ДОКСОРУБИЦИНОМ И ФОТОСЕНСИБИЛИЗАТОРОМ ФОТОЛОН В ЭКСПЕРИМЕНТЕ *IN VIVO*

Д.А. Церковский[1], **Н.Д. Адаменко**[2]
[1]Республиканский научно-практический центр онкологии и медицинской радиологии им. Н.Н. Александрова, Минск, Республика Беларусь
[2]Витебский государственный университет им. П.М. Машерова, Витебск, Республика Беларусь

Резюме

Исследована противоопухолевая эффективность сонодинамической терапии (СДТ) с химиотерапевтическим лекарственным средством (ХЛС) и фотосенсибилизатором (ФС) хлоринового ряда в эксперименте *in vivo*. Работа выполнена на 60 белых нелинейных крысах, распределенных на 2 серии по 30 особей в каждой. В качестве опухолевого штамма использовали лимфосаркому Плисса, перевиваемую подкожно. Фотолон вводили внутривенно однократно в дозе 2,5 мг/кг за 2,5-3 ч до ультразвукового воздействия, а доксорубицин – внутрибрюшно однократно в дозе 5 мг/кг за 0,5 ч до ультразвукового воздействия, осуществляемого с помощью аппарата «Phyaction U», генерирующего излучение с частотой 1,04 МГц, интенсивностями 0,5 и 1,5 Вт/см^2 и продолжительностью 5 мин. Группы исследования в каждой из серий включали по 5 крыс: контроль, ультразвук, доксорубицин, фотолон + ультразвук, доксорубицин + ультразвук, фотолон + доксорубицин + ультразвук. Для оценки противоопухолевой эффективности использовались общепринятые

в экспериментальной онкологии критерии: средний объем опухолей ($V_{ср}$, $см^3$), коэффициент абсолютного прироста опухолей (К, отн. ед.), коэффициент торможения роста опухолей (ТРО, %), частота полных опухолевых регрессий (ПР, %), средняя продолжительность жизни крыс (СПЖ, сут), коэффициент увеличения средней продолжительности жизни крыс (УПЖ, %) и медиана общей выживаемости (сут). Различия считали статистически значимыми при уровне значимости $p<0,05$. В первой и второй сериях экспериментов наиболее эффективными режимами было применение фотолон, доксорубицин и ультразвука с частотой 1,04 МГц и интенсивностями 0,5 и 1,5 $Вт/см^2$ соответственно. Предложенное сочетание терапевтических воздействий позволило статистически значимо ($p<0,05$) увеличить показатели ТРО, ПР и УПЖ по сравнению с контролем и каждым из компонентов метода в отдельности. Разработанные и апробированные в экспериментах *in vivo* методики СДТ характеризуются высокой противоопухолевой эффективностью.

Ключевые слова: лимфосаркома Плисса, доксорубицин, фотолон, ультразвук, сонодинамическая терапия.

Контакты: Церковский Д.А., tzerkovsky@mail.ru.

Для цитирования: Церковский Д.А., Адаменко Н.Д. Сонодинамическая терапия с доксорубицином и фотосенсибилизатором фотолон в эксперименте *in vivo* // Biomedical Photonics. – 2024. – Т. 13, № 4. – С. 22–32. doi: 10.24931/2413–9432–2024–13–4–22–32

Inrtoduction

The search for and testing of new methods for treating malignant neoplasms at the preclinical stage of research with their subsequent implementation in practical healthcare is a key aspect of experimental and clinical oncology. It is well known that the gold standard for treating patients with malignant neoplasms is surgery, radiation therapy and chemotherapy. A number of alternative methods based on the influence of physical factors on tumor cells and tissues also have a certain therapeutic potential. Such methods primarily include laser therapy, cryotherapy, hyperthermia, high-intensity focused ultrasound, etc. From a scientific point of view, it is relevant to study the possibility of combined use of ultrasound radiation (US) and various classes of drugs.

According to a number of authors, the effect of ultrasound with a pulse frequency of 0.5-3 MHz and an intensity of 0.5-5 W/cm^2 can increase the cytotoxicity of various chemotherapeutic drugs. Researchers associate this fact with an increase in the permeability of cell membranes and the implementation of the effects of cavitation, hyperthermia and sono-induced free-radical oxidation of the biological structures of the tumor cell [1, 2]. A new direction in experimental oncology is called "sonodynamic therapy" (SDT), and the drugs used are called sonosensitizers (SS). The SS class primarily includes radiosensitizers (dimexide, metronidazole) and a number of chemotherapeutic agents (bleomycin, adriamycin, cisplatin, etoposide, 5-fluorouracil, etc.) [3].

At the same time, in the late 80s of the 20th century, Japanese scientists led by T. Yumita conducted preclinical studies on tumor cell cultures, proving the presence of sonosensitizing properties in another class of drugs, such as photosensitizers (PS), which until then had been actively used for photodynamic therapy. In 1990, the first results were published confirming the high antitumor efficacy of SDT with hematoporphyrin [4].

In recent years, the results of numerous *in vitro* and *in vivo* studies have been published, indicating the high antitumor efficacy of SDT with PS in the treatment of a number of nosological forms of malignant neoplasms (breast cancer, lung, intestine, pancreas, soft tissue sarcoma, skin melanoma, osteosarcoma, leukemia, glioma) [5, 6, 7, 8]. A relevant and promising area of scientific research is the combined use of SDT with drugs that have fundamentally different mechanisms for implementing an antitumor response when activated by ultrasound, namely, PS and chemotherapeutic drugs [9, 10, 11, 12, 13].

There are a small number of publications in the foreign literature devoted to the study of this issue, most of which were carried out in *in vitro* experiments. So, H.J. Gao et al. (2010) (Department of Clinical Oncology, Guangzhou General Hospital of Guangzhou Command, People's Republic of China) assessed the effectiveness of SDT with chlorine e6 in doses from 0.05 to 1.6 mg/ml and adriamycin in doses from 0.1 to 0.4 g/ml on human breast cancer cell culture *MDA-MB-231*. The use of US with a frequency of 1 MHz and intensities from 0.5 to 2 W/cm^2 after preliminary addition of PS to the cell culture followed by the addition of adriamycin after sonodynamic exposure caused a statistically significant reduction in the number of viable tumor cells compared to each of the components of the proposed scheme ($p<0.05$) [9].

L. Liang et al. (2013) (State Key Laboratory of Bioreactor Engineering, Shanghai Key Laboratory of Chemical Biology, People's Republic of China) in an experiment on a culture of human cholangiocarcinoma tumor cells *QBC939* proved a dose-dependent increase in the cytotoxicity of hematoporphyrin and doxorubicin monomethyl ester when combined with US. Doxorubicin was used in doses of 0.0625; 0.125; 0.25; 0.5; 1; 2 and 4 μg/ml, and PS - 5, 10, 20, 40 and 80 μg/ml. Local ultrasonic influence on tumor cells, sensitized with the help of these drugs, was carried out with a frequency of 1.2 MHz and intensities from 0.5 to 2 W/cm^2. The authors used various combinations of drugs and ultrasound modes. The results obtained indicate a statistically significant increase in the number of non-viable tumor cells due

to the toxic effect of a significantly higher percentage of reactive oxygen species and significant activation of cell apoptosis when using ultrasound with high doses of both drugs. In addition, the expression of *p53*, *Fas*, *Bax* and *caspase-3* were significantly upregulated in cells exposed to the combination therapy [10].

T. Osaki et al. (2016) (Joint Department of Veterinary Clinical Medicine, Japan) studied the sonodynamic properties of 5-aminolevulinic acid (5-ALA) and bleomycin in combination with US with frequencies of 1 and 3 MHz, and intensities from 1 to 3 W/cm^2 in an experiment on mouse mammary cell culture. Thus, when using US with a frequency of 1 MHz and intensities of 1, 2 and 3 W/cm^2, the number of viable tumor cells decreased by 34.30%, 50.90% and 60.16%, respectively. When bleomycin was added to the cell culture with its further insonation, it led to a significant reduction in this indicator: 0.09%, 0.32% and 0.17%, respectively. Additionally, the authors report that the use of US with a frequency of 3 MHz, regardless of the radiation intensity and exposure modes, did not lead to positive results [11].

The same team of authors obtained similar results in an experiment on cell culture and laboratory animals with intestinal carcinoma of *Colon-26* mice with the combined use of bleomycin, aluminum disulfonate phthalocyanine and low-intensity US. PS was used in doses of 1, 5 and 10 μg/ml, bleomycin - in doses of 1, 5 and 10 μg/ml. Ultrasonic exposure was carried out with a frequency of 3 MHz and intensities from 1 to 3 W/cm^2, the frequency of ultrasonic pulses, depending on the series of experiments, varied from 5% to 100%. The number of viable cells in the «Bleomycin + SDT» group was statistically significantly lower compared to that in groups with different doses of PS (1, 5 and 10 μg/ml) when used in combination with US ($p=0.0498$; $p=0.0405$ and $p=0.0219$; respectively). The studied indicator in the combination therapy group «PS + bleomycin + SDT» was statistically lower than in the groups «PS + SDT» and «Bleomycin + SDT» ($p<0.05$) [12].

In the *in vivo* part of the study, performed on linear BALB/c mice with a subcutaneous model of intestinal carcinoma *Colon-26*, the high antitumor efficacy of combination therapy was proven. The study design included the following groups: intact control; PS; bleomycin; US; PS + US; bleomycin + US and PS + bleomycin + US (combination therapy). PS was administered once intraperitoneally at a dose of 20 mg/ml 18 hours before ultrasound exposure of transplanted tumors. Bleomycin – once intraperitoneally at a dose of 25 mg/ml 0.5 hours before ultrasound exposure of transplanted tumors. The SDT session was carried out with an ultrasound frequency of 3 MHz (50%) and intensity of 3 W/cm^2. The criteria for assessing effectiveness were the volume of tumors, calculated on the 12th day after the start of therapeutic interventions, and histological examination data. The authors registered a statistically significant inhibition of the growth of transplanted tumors in the group of combination therapy using drugs in the indicated doses compared with each component of the treatment regimen ($p<0.05$) and the control. According to a morphological study, this fact was associated with both a direct cytotoxic effect and lethal damage to tumor cells and tissues due to disruption of the blood supply to tumors due to disruption of the integrity and patency of the blood vessels feeding them ($p<0.05$) [12].

In a study by R. Xu et al. (2020) (Department of Breast Surgery, The First Affiliated Hospital, People's Republic of China) studied the antitumor efficacy of the combined use of high-intensity US with an intensity of 4 W/cm^2 in combination with silicon nanoparticles with doxorubicin and chlorin e6. In the *in vivo* experiment, we used linear BALB/c nude mice with subcutaneously inoculated human breast cancer *MDA-MB-231*. The data obtained indicate a significant inhibition of growth and a decrease in the weight of experimental tumors when using a combination treatment regimen compared with each of its components ($p<0.05$) [13].

The purpose of this work is to study the antitumor effectiveness of the SDT method with photolon and doxorubicin using low- and high-intensity US.

Materials and methods

Laboratory animals

The pilot study was performed on 60 white nonlinear outbred male rats obtained from the vivarium of N.N. Alexandrov National Cancer Centre of Belarus, with a body weight from 150 to 300 g, aged 2.5-3 months. The duration of quarantine before inclusion in the experiment was 14 days. The rats were kept under standard conditions of food and drink rations *ad libitum*, with 12-hour illumination, at a temperature of 18–22°C and a humidity of 55–60% in individual cages, 5 individuals in each. The conditions for keeping rats in the laboratory, as well as humidity, temperature, and lighting in the room, complied with the current sanitary rules for the design, equipment and maintenance of vivariums [14, 15, 16].

Tumor strain

Pliss lymphosarcoma (PLS) obtained as a cell culture (Russian Collection of Cell Cultures, Institute of Cytology RAS, St. Petersburg, Russian Federation) was used as a tumor strain.

Tumor model

PLS cell culture was inoculated subcutaneously in rats. Subcutaneous inoculation of the experimental study included the introduction under the skin of the left inguinal region of 0.5 ml of a suspension of tumor cells in 20% Hanks solution, obtained after taking and homogenizing tumor pieces from a donor rat. PLS is one of the rapidly growing tumors with a short latent period. In this regard, rats with PLS were included in the

experiment on the 5th day after transplantation, when the diameter of the tumor node, on average, was 5 mm.

Ethical aspects

Experimental studies were carried out in accordance with international legislation and the regulatory legal acts in force in the Republic of Belarus for conducting experimental studies with laboratory animals [17, 18, 19].

The nature of the studies performed was consistent with the principles of «3Rs» developed by W.M. Russell and R.L. Berch (1959) [20].

The study was approved by the Ethics Committee of the N.N. Alexandrov National Cancer Center of Belarus (protocol № 180).

Before irradiation, rats were anesthetized (neuroleptanalgesia: 0.005% fentanyl solution + 0.25% droperidol solution, in a ratio of 2:1, 0.2 ml per 100 g of body weight, intramuscularly). After the end of the observation period, the rats were sacrificed using generally accepted methods of euthanasia (*aether pro narcosi*) in compliance with the humane methods of handling laboratory animals.

Chemotherapy drug

The injection form of lyophilized doxorubicin powder (DOX) (RUE «Belmedpreparaty», Minsk, Republic of Belarus) was used as a chemotherapeutic drug. The DOX were dissolved in a 0.9% sodium chloride solution and administered on the 5th day after tumor transplantation with LSP once, intraperitoneally, at a dose of 5 mg/kg.

Photosensitizer

As a drug, an injectable form of PS based on chlorin e6 photolon (RUE «Belmedpreparaty», Minsk, Republic of Belarus, registration number 16/11/886 dated November 08, 2016, 100 mg) was used. Before use, PS powder was diluted with 0.9% sodium chloride solution and administered once by intravenous infusion into the tail vein of a rat in a darkened room at a dose of 2.5 mg/kg.

Sonodynamic therapy

A session of local ultrasound therapy (US) was carried out once using a device («Phyaction U», Gymna Yniphy, Belgium) using an applicator with a emitting surface area of 5 cm^2 with a frequency of 1.04 MHz, intensities of 0.5 and 1.5 W/cm^2 and lasting 5 minutes in continuous mode after preliminary hair depilation and surface treatment experimental tumor with a special gel. The ultrasound session began 2.5–3 hours after photolon administration, and intraperitoneal administration of DOX was carried out 0.5 hours before irradiation.

Study design

All therapeutic effects were carried out on the 5th day after LSP grafting, upon reaching the diameter of the tumor node of at least 5 mm. The control group consisted of rats with a transplanted tumor, which were not administered PS, DOX and were not irradiated (control). All rats were randomly distributed at each stage of the study into 6 groups of 5 individuals each (Tables 1, 2).

Таблица 1
Дизайн экспериментального исследования (серия 1)
Table 1
Experimental study design (series 1)

Наименование группы Groups	Количество крыс в группе, n Number of rats in the group, n
Контроль Control	5
ДОКС 5 мг/кг DOX 5 mg/kg	5
УЗТ 1,04 МГц; 0,5 Вт/см^2 UT 1.04 MHz; 0.5 W/cm^2	5
ДОКС 5 мг/кг + УЗТ 1,04 МГц; 0,5 Вт/см^2 DOX 5 mg/kg + US 1.04 MHz; 0.5 W/cm^2	5
ФС 2,5 мг/кг + УЗТ 1,04 МГц; 0,5 Вт/см^2 PS 2.5 mg/kg + US 1.04 MHz; 0.5 W/cm^2	5
ФС 2,5 мг/кг + ДОКС 5 мг/кг + УЗТ 1,04 МГц; 0,5 Вт/см^2 PS 2.5 mg/kg + DOX 5 mg/kg + US 1.04 MHz; 0.5 W/cm^2	5

*ДОКС – доксорубицин; УЗТ – ультразвуковая терапия; ФС – фотосенсибилизатор.
*DOX – doxorubicin; US – ultrasound therapy; PS – photosensitizer.

Таблица 2
Дизайн экспериментального исследования (серия 2)
Table 2
Experimental study design (series 2)

Наименование группы Groups	Количество крыс в группе, n Number of rats in the group, n
Контроль Control	5
ДОКС 5 мг/кг DOX 5 mg/kg	5
УЗТ 1,04 МГц; 1,5 Вт/см^2 UT 1.04 MHz; 1.5 W/cm^2	5
ДОКС 5 мг/кг + УЗТ 1,04 МГц; 1,5 Вт/см^2 DOX 5 mg/kg + US 1.04 MHz; 1.5 W/cm^2	5
ФС 2,5 мг/кг + УЗТ 1,04 МГц; 1,5 Вт/см^2 PS 2.5 mg/kg + US 1.04 MHz; 1.5 W/cm^2	5
ФС 2,5 мг/кг + ДОКС 5 мг/кг + УЗТ 1,04 МГц; 1,5 Вт/см^2 PS 2.5 mg/kg + DOX 5 mg/kg + US 1.04 MHz; 1.5 W/cm^2	5

*ДОКС – доксорубицин; УЗТ – ультразвуковая терапия; ФС – фотосенсибилизатор.
*DOX – doxorubicin; US – ultrasound therapy; PS – photosensitizer.

Criteria for evaluating antitumor efficacy

The antitumor efficacy of the interventions was assessed according to the indicators generally accepted in experimental oncology, which characterize the dynamics of changes in the average tumor volume ($V_{av.}$, cm^3), as well

as the change in the coefficient of absolute tumor growth (K) and the index of tumor growth inhibition (TGI, %). The growth dynamics of transplanted tumors was recorded starting from the 6th day after transplantation of the PLS tumor strain for 2 weeks with an interval of 2–3 days.

Tumor volume was calculated using the following Shreks formula (1):

$$V = \frac{\pi}{6} \times d1 \times d2 \times d3\ , \qquad (1)$$

where:

d1,2,3 – three mutually perpendicular tumor diameters (in cm);

π/6 = 0.52 – a constant value;

V – the volume of the tumor (in cm^3).

The coefficient of absolute tumor growth (K) was calculated by the following formula (2):

$$K = \frac{Vt - V_0}{V_0}, \qquad (2)$$

where:

V_0 – the initial volume of the tumor (before exposure);

Vt – the tumor volume for a certain period of observation.

The coefficient of tumor growth inhibition (TGI) was calculated by the following formula (3):

$$TGI = \frac{Vcontrol - Vexpeirence}{Vcontrol} \times 100\%, \qquad (3)$$

where:

$V_{control}$ – the average volume of the tumor in the control group (in cm^3);

$V_{experience}$ – the average volume of the tumor in the main group (in cm^3).

The minimally significant criterion demonstrating the effectiveness of the treatment of transplanted tumors was considered TGI > 50%.

The frequency of complete tumor regressions (CR) was assessed 60 days after the end of exposure by the absence of visual and palpatory signs of tumor growth.

$$CR\ frequency = \frac{Number\ of\ animals\ without\ tumors}{Number\ of\ animals\ in\ group} \times$$

$$\times\ 100\%. \qquad (4)$$

The evaluation of the antitumor effect by increasing the lifespan was carried out at the end of the experiment and the death of all rats. The average life expectancy (ALE, days) in the groups was determined and the indicators of life expectancy increase (LEI, %) were calculated using the formula [5]:

$$LEI = \frac{ALEexperiment - ALEcontrol}{ALEcontrol} \times 100\%, \qquad (5)$$

where:

LEI – an indicator of the increase in the life expectancy of dead rats (in %);

$ALE_{experiment}$ – the average life expectancy of dead rats in the experimental groups (per day);

$ALE_{control}$ – the average life expectancy of dead rats in the control group (per day).

The minimum significant indicator of LEI demonstrating the effectiveness of treatment of transplanted tumors was considered to be 50%.

Statistical processing of the obtained data

Statistical processing of data ($V_{av.}$, coefficients K and TGI) was carried out using application packages Excel (version 2010), Origin Pro (version 7.0) and Statistica (version 10.0). Data were presented as M±m (mean ± error of the mean). To assess the significance of differences, the nonparametric *Mann-Whitney U test* was used. Comparative analysis of survival rates was carried out using a nonparametric *log-rank test*. Differences were considered statistically significant at a significance level of $p<0.05$.

Results and discussion

The effectiveness of the interventions proposed in the Design was assessed based on the analysis of indicators characterizing the change in the dynamics of the linear sizes of transplanted tumors ($V_{av.}$, coefficients K and TGI).

Information about the dynamics of changes in $V_{av.}$ and, accordingly, the coefficients K and TGI associated with this indicator, when using the above effects in rats with LSP in series 1 of the experiment are presented in Table 3.

Combination therapy, including a single intra-abdominal injection of DOX at a dose of 5 mg/kg, followed 0.5 hours later by an US session with a frequency of 1.04 MHz and an intensity of 0.5 W/cm^2 according to the $V_{av.}$ Criterion was statistically significantly more effective compared to US alone (p=0.001; $V_{av.}$ in the group was 4.59 times less) and tended to increase efficiency compared to chemotherapy without radiation (p=0.86; $V_{av.}$ in the group 1.2 times less).

In turn, combination therapy, including a single intravenous injection of photolon at a dose of 2.5 mg/kg 2.5–3 hours and intraperitoneal administration of DOX at a dose of 5 mg/kg 0.5 hours before the ultrasound session with a frequency of 1.04 MHz and intensity 0.5 W/cm^2 according to the $V_{av.}$ criterion was statistically significantly more effective compared to the combined use of PS and US (p=0.004; $V_{av.}$ in the group was 9.84 times less) and tended to increase efficiency compared to the DOX + US regimen (p=0.61; $V_{av.}$ in the group was 1.94 times less).

When assessing long-term results in terms of the incidence of CR of tumors, high efficiency was noted both in the DOX group and in the combination therapy groups (DOX + US and PS + DOX + US). It is worth noting that in the PS + DOX + US group the most optimistic results were recorded according to the criteria for

lifespan and lifespan compared to the control group (ALE 52.0±5.1 days versus 18.0±1.0 days; LEI = 188.89%; p=0.00004). When comparing data on survival rates in this group with the results of groups in which the effects are components of a «triple» scheme, statistical significance was obtained for the differences in life

Таблица 3
Данные о динамике изменения линейных размеров опухолей в эксперименте на крысах с ЛСП

Table 3
Data on the dynamics of changes in the linear sizes of tumors in an experiment on rats with LSP

Наименование группы Groups	Критерии оценки противоопухолевого эффекта Criteria for assessing the antitumor effect					
	Средний объем опухолей ($V_{ср.}$), в см³ (M±m) 95% ДИ Average tumor volume ($V_{av.}$), cm³ (M±m) 95% CI					
	Коэффициент абсолютного прироста опухолей (К), в отн.ед. Absolute tumor growth rate (K), units					
	Коэффициент торможения роста опухолей (ТРО), в % Tumor growth inhibition coefficient (TGI), %					
	p vs. контроль p vs. control					
	сутки после перевивки days after transplantation					
	5	7	10	12	14	17
Контроль Control	0,03±0,01	1,61±0,53 0,6-2,6	11,23±2,05 7,2-15,2	19,92±3,04 14,0-25,9	41,91±4,08 33,9-49,9	57,89±4,45 49,2-66,6
	–	52,67	373,33	663,00	1396,00	1928,67
	–	–	–	–	–	–
	–	–	–	–	–	–
ДОКС DOX	0,02±0,01	0,90±0,42 0,1-1,7	2,03±1,48 0,9-4,9	3,04±2,59 2,0-8,1	5,19±4,02 2,7-13,1	9,17±7,05 4,6-23,0
	–	44,00	100,50	151,00	258,50	457,50
	–	44,10	81,92	84,74	87,62	84,16
	>0,05	0,32	0,0039	0,0014	0,00005	0,0001
УЗТ US	0,03±0,01	0,89±0,39 0,1-1,7	8,64±2,24 4,2-13,0	14,25±3,29 7,8-20,7	22,89±4,42 14,2-31,6	34,98±2,26 30,6-39,4
	–	28,67	287,00	474,00	762,00	1165,00
	–	44,72	23,06	28,46	45,38	39,58
	>0,05	0,29	0,41	0,23	0,009	0,0008
ДОКС + УЗТ DOX + US	0,03±0,01	0,33±0,06 0,2-0,4	1,33±1,27 1,2-3,8	4,15±4,07 3,8-12,1	5,91±5,09 4,1-15,9	7,62±5,88 3,9-19,1
	–	10,00	43,33	137,33	196,00	253,00
	–	79,50	88,16	79,17	85,89	86,84
	>0,05	0,035	0,0017	0,01	0,00018	0,00003
ФС + УЗТ PS + US	0,02±0,01	1,26±0,38 0,5-2,0	8,52±1,57 5,4-11,6	17,93±2,75 12,5-23,3	22,71±3,39 16,1-29,4	38,67±8,68 21,7-55,7
	–	62,00	425,00	895,50	1134,50	1932,50
	–	21,74	24,13	9,99	45,81	33,20
	>0,05	0,60	0,32	0,64	0,004	0,075
ФС + ДОКС + УЗТ PS + DOX + US	0,03±0,01	0,08±0,05 0,0-0,2	0,65±0,65 0,6-1,9	1,77±1,77 1,7-5,2	2,19±2,19 2,1-6,5	3,93±3,93 3,8-11,6
	–	1,67	20,67	58,00	72,00	130,00
	–	95,03	94,21	91,11	94,77	93,21
	>0,05	0,015	0,0005	0,0003	0,000003	0,000002

*ДОКС – доксорубицин; УЗТ – ультразвуковая терапия; ФС – фотосенсибилизатор.
*DOX – doxorubicin; US – ultrasound therapy; PS – photosensitizer.

expectancy rates and median overall survival (52.0±5.1 days and 49 days versus 19.0±0.0 days and 19 days for DOX + US (p=0.00005), and 20.4±0.6 day and 21 days for PS + US (p=0.00007), respectively) (Table 4).

Information about the dynamics of changes in $V_{av.}$ and, accordingly, the coefficients K and TGI associated with this indicator, when using the above effects in rats with LSP in series 2 of the experiment are presented in Table 5.

When carrying out combined therapy of transplanted LSP tumors in rats with a single intra-abdominal injection of DOX at a dose of 5 mg/kg, followed 0.5 hours later by an US session with a frequency of 1.04 MHz and an intensity of 1.5 W/cm^2, a moderately pronounced inhibition of tumor growth was noted in compared with US in mono mode ($V_{av.}$ in the group is 3.35 times less, p=0.0014) and with chemotherapy without radiation ($V_{av.}$ in the group was 1.19 times less, p=0.74).

Combination therapy based on a single intravenous injection of photolon at a dose of 2.5 mg/kg for 2.5–3 hours and intraperitoneal administration of DOX at a dose of 5 mg/kg 0.5 hours before an ultrasound session with a frequency of 1.04 MHz and intensity 1.5 W/cm^2, was characterized by greater antitumor efficacy in comparison with the combined use of PS and US ($V_{av.}$ in the group is 6.70 times less, p=0.0078) and DOX + US ($V_{av.}$ in the group is 2.34 times less, p=0.087).

60 days after the implementation of therapeutic interventions in the second series of experiments, the highest incidence of CR (40%) was noted in the combination therapy group (PS + DOX + US). When assessing the survival rates of dead rats, there was no statistical difference with the control in the groups, with the exception of DOX + US (p=0.043), (p<0.05) (Table 6).

In recent years, the interest of researchers in studying the possibility of using methods based on the action of physical factors in the schemes of combined, complex and multicomponent treatment of malignant neoplasms has significantly increased. Such methods include photodynamic therapy [21, 22, 23, 24], cryotherapy [25, 26], hyperthermia [27] and others. A promising direction of scientific research is to study the possibility of combined use of ultrasound and different classes of drugs (sonodynamic therapy, SDT).

The SDT methods with various classes of drugs developed in our study and tested *in vivo* experiments have high antitumor efficacy. The first and second series of experiments showed that two modes are the most effective: the use of photolon, DOX and US with a frequency of 1.04 MHz and intensities of 0.5 and 1.5 W/cm^2, respectively. The proposed combination of therapeutic effects made it possible to significantly inhibit the growth of transfused tumors (p<0.05), increase the frequency of CR (p<0.05) and optimize the survival rates of rats (p<0.05) with transfused tumors compared with the control and each of the components of the method separately.

The closest analogue to our study is the work of P. Xu (2020) (The First Affiliated Hospital, People's Republic of China), in which the authors studied the antitumor efficacy of high-intensity US with an intensity of 4 W/cm^2 in combination with silicon nanoparticles with doxorubicin and e6 chloride on a human breast

Таблица 4
Информация об отдаленных результатах исследования

Table 4
Information about long-term results of the study

Наименование группы Groups	Критерии оценки противоопухолевого эффекта Criteria for assessing the antitumor effect			p vs. контроль p vs. control
	Частота полных регрессий, % Frequency complete regressions, %	СПЖ, сут 95 ДИ, % Average life expectancy, days 95 CI, %	УПЖ, % Average life expectancy increase rate, days	
Контроль Control	0	18,0±1,0 16,0-20,0	–	–
ДОКС DOX	40	26,0±7,0 12,3-39,7	44,44	0,28
УЗТ US	0	19,0±0,0 19,0-19,0	5,55	0,33
ДОКС + УЗТ DOX + US	60	19,0±0,0 19,0-19,0	5,55	0,33
ФС + УЗТ PS + US	0	20,4±0,6 19,2-21,6	13,33	0,06
ФС + ДОКС + УЗТ PS + DOX + US	40	52,0±5,1 42,1-62,1	188,89	0,00004

*ДОКС – доксорубицин; УЗТ – ультразвуковая терапия; ФС – фотосенсибилизатор; СПЖ – средняя продолжительность жизни; УПЖ – коэффициент увеличения средней продолжительности жизни.
*DOX – doxorubicin; US – ultrasound therapy; PS – photosensitizer.

Таблица 5
Данные о динамике изменения линейных размеров опухолей в эксперименте на крысах с ЛСП

Table 5
Data on the dynamics of changes in the linear sizes of tumors in an experiment on rats with LSP

Наименование группы Groups	Критерии оценки противоопухолевого эффекта Criteria for assessing the antitumor effect					
	Средний объем опухолей ($V_{ср.}$), в см^3 (M±m) 95% ДИ Average tumor volume ($V_{av.}$), cm^3 (M±m) 95% CI					
	Коэффициент абсолютного прироста опухолей (K), в отн.ед. Absolute tumor growth rate (K), units					
	Коэффициент торможения роста опухолей (ТРО), в % Tumor growth inhibition coefficient (TGI), %					
	p vs. контроль p vs. control					
	сутки после перевивки days after transplantation					
	5	7	9	12	14	16
Контроль Control	0,012±0,002	1,63±0,22 1,2-2,1	11,43±1,42 8,6-14,2	21,81±1,63 18,6-25,0	54,19±2,95 48,4-60,0	66,11±2,89 60,4-71,8
	–	134,83	951,50	1816,50	4514,83	5508,17
	–	–	–	–	–	–
	–	–	–	–	–	–
ДОКС DOX	0,014±0,001	0,99±0,21 0,6-1,4	3,41±0,27 2,9-3,9	6,56±0,72 5,1-8,0	8,66±1,19 6,3-11,0	9,75±1,42 7,0-12,5
	–	69,71	242,57	467,57	617,57	695,43
	–	39,26	70,17	69,92	84,02	85,25
	>0,05	0,059	0,0002	0,000003	0,00000	0,00000
УЗТ US	0,012±0,002	1,03±0,19 0,7-1,4	3,93±0,83 2,3-5,6	15,02±2,86 9,4-20,6	26,47±3,54 19,5-33,4	27,51±4,00 19,7-35,4
	–	84,83	326,50	1250,67	2204,83	2291,50
	–	36,81	65,62	31,13	51,15	58,39
	>0,05	0,063	0,0008	0,063	0,00009	0,00008
ДОКС + УЗТ DOX + US	0,011±0,001	0,32±0,07 0,2-0,5	0,85±0,22 0,4-1,3	5,05±1,49 2,1-8,0	7,19±1,96 3,3-11,0	8,22±2,18 3,9-12,5
	–	28,09	76,27	458,10	652,64	746,27
	–	80,34	92,56	76,85	86,73	87,57
	>0,05	0,0001	0,00001	0,00001	0,00000	0,00000
ФС + УЗТ PS + US	0,011±0,002	0,65±0,25 0,2-1,1	2,54±0,72 1,1-4,0	12,12±3,67 4,9-19,3	21,36±5,92 9,8-33,0	23,53±6,04 11,7-35,4
	–	58,09	229,91	1100,82	1940,82	2138,09
	–	60,12	77,78	44,43	60,58	64,41
	>0,05	0,013	0,0002	0,034	0,0004	0,00005
ФС + ДОКС + УЗТ PS + DOX + US	0,011±0,002	0,33±0,08 0,2-0,5	0,83±0,29 0,3-1,4	2,14±0,67 0,8-3,5	3,41±1,12 1,2-5,6	3,51±1,24 1,1-5,9
	–	29,00	74,45	193,55	309,00	318,09
	–	79,75	92,74	90,18	93,71	94,69
	>0,05	0,0002	0,00002	0,00000	0,00000	0,00000

*ДОКС – доксорубицин; УЗТ – ультразвуковая терапия; ФС – фотосенсибилизатор.
*DOX – doxorubicin; US – ultrasound therapy; PS – photosensitizer

Таблица 6
Информация об отдаленных результатах исследования
Table 6
Information about long-term results of the study

Наименование группы Groups	Критерии оценки противоопухолевого эффекта Criteria for assessing the antitumor effect			p vs. контроль p vs. control
	Частота полных регрессий, % Frequency complete regressions, %	СПЖ, сут 95 ДИ, % Average life expectancy, days 95 CI, %	УПЖ, % Average life expectancy increase rate, days	
Контроль Control	0	19,0±0,0 19,0-19,0	–	–
ДОКС DOX	20	21,3±1,3 18,8-23,8	12,11	0,11
УЗТ US	0	19,0±0,0 19,0-19,0	0,00	1,00
ДОКС + УЗТ DOX + US	0	22,2±1,4 19,7-25,1	16,84	0,043
ФС + УЗТ PS + US	20	20,0±0,0 20,0-20,0	5,26	1,00
ФС + ДОКС + УЗТ PS + DOX + US	40	20,0±0,0 20,0-20,0	5,26	1,00

*ДОКС – доксорубицин; УЗТ – ультразвуковая терапия; ФС – фотосенсибилизатор; СПЖ – средняя продолжительность жизни; УПЖ – коэффициент увеличения средней продолжительности жизни.
*DOX – doxorubicin; US – ultrasound therapy; PS – photosensitizer.

cancer tumor model *MDA-MB-231*. The data obtained indicate a significant inhibition of growth and a decrease in the mass of experimental tumors when using the combined treatment regimen compared with each of its components ($p<0.05$) [13]. Nevertheless, the use of higher US intensities in this study may be associated with a greater risk of serious adverse reactions and the predominant realization of the effects of hyperthermia rather than sonochemical reactions.

Systematization and analysis of the above publications of foreign researchers allowed us to conclude that the use of PS and chemotherapy drugs in combination with US radiation (sonodynamic effect) was characterized by a synergistic increase in the antitumor effectiveness of combined therapy compared with each of its components, which was confirmed by a statistically significant increase in the number of non-viable tumor cells and inhibition of the growth of transfused tumors in laboratory animals. The mechanism of action of chemotherapy drugs (doxorubicin, adriamycin, bleomycin) used in the listed *in vitro/in vivo* studies consists in interaction with DNA, formation of free radicals and direct action on cell membranes with suppression of nucleic acid synthesis. Ultrasound exposure to tumor cells sensitized by these drugs can significantly increase their active therapeutic concentration by affecting the permeability of tumor cell membranes. In the case of sonodynamic activation of PS, sonochemical reactions mediated by the influence of ultrasound occur in the structures of tumor cells due to the toxic effects of significantly increasing amounts of reactive oxygen species formed during sonodynamic modification of PS molecules. An important role is played by the effects of ultrasound itself, such as cavitation and local hyperthermia, leading to both direct and indirect damage to tumors due to disruption of the functional state and integrity of blood vessels that feed tumor tissues.

Considering that in the available literature sources we have found only a few publications devoted to the study of the effectiveness of the combined use of PS and chemotherapy drugs in combination with ultrasonic radiation, the implementation of further research in this area is an urgent and promising area of scientific work. It is advisable to perform experiments on a larger number of tumor models (subcutaneous, orthotopic). Equally important is the study of the antitumor effectiveness of SDT methods with a large number of PS and chemotherapy drugs, as well as the implementation of studies aimed at exploring the possibilities of using subtherapeutic doses of drugs in order to reduce the frequency and severity of adverse reactions.

CONCLUSION

The methods of SDT with various classes of drugs developed in our study make it possible to expand the range of therapeutic options in experimental and clinical oncology.

The work was carried out with financial support from the Belarusian Republican Foundation for Basic Research (Grant No. M21M-031).

REFERENCES

1. Costley D., McEwan C., Fowley C., et al. Treating cancer with sonodynamic therapy: A review. *Int. J. Hyperthermia*, 2015, vol. 32(2), pp. 107–117. doi: 10.3109/02656736.2014.992484.
2. Escoffre J.M. and Bouakaz A.B. Therapeutic ultrasound. – Switzerland: Springer, 2016. – 459 p.
3. Rosenthal I., Sostaric J.Z., Riesz R. Sonodynamic therapy – a review of the synergistic effects of drugs and ultrasound. *Ultrasonics Sonochem.*, 2004, vol. 11, pp. 349–363. doi: 10.1016/j.ultsonch.2004.03.004.
4. Yumita T., Nishigaki R., Umemura K., et al. Synergetic effect of ultrasound and hematoporphyrin on sarcoma 180. *J. Jpn. Cancer Res.*, vol. 1990, vol. 81, pp. 304–308. doi: 10.1111/j.1349-7006.1990.tb02565.x.
5. McHale A.P., Callan J.F., Nomikou N., et al. Sonodynamic therapy: concept, mechanism and application to cancer treatment. *Adv. Exp. Med. Biol.*, 2016, vol. 880, pp. 429–450. doi: 10.1007/978-3-319-22536-4_22.
6. Xu M., Zhou L., Zheng L., et al. Sonodynamic therapy-derived multimodal synergistic cancer therapy. *Cancer Lett.*, 2021, vol. 497, pp. 229–242. doi: 10.1016/j.canlet.2020.10.037.
7. Tzerkovsky D.A., Protopovuch Ya.L., Stupak D.S. Sonodynamic and sono-photodynamic therapy in oncology. *Biomedical Photonics*, 2019, vol. 8(2), pp. 31–46. https://doi.org/10.24931/2413-9432-2019-8-2-31-46.
8. Liao S., Cai M., Zhu R., et al. Antitumor effect of photodynamic therapy/sonodynamic therapy/sono-photodynamic therapy of chlorin e6 and other applications. *Mol. Pharm.*, 2023, vol. 20(2), pp. 875–885. doi: 10.1021/acs.molpharmaceut.2c00824.
9. Gao H.J., Zhang W.M., Wang X.H., et al. Adriamycin enhances the sonodynamic effect of chlorin e6 against the proliferation of human breast cancer MDA-MB-231 cells *in vitro*. *Nan. Fang Yi Ke Da Xue Xue Bao.*, 2010, vol. 30(10), pp. 2291–2294.
10. Liang L., Xie S., Jiang L., et al. The combined effects of hematoporphyrin monomethyl ether-SDT and doxorubicin on the proliferation of QBC939 cell lines. *Ultrasound. Med. Biol.*, 2013, vol. 39(1), pp. 146–160. doi: 10.1016/j.ultrasmedbio.2012.08.017.
11. Osaki T., Ono M., Uto Y., et al. Sonodynamic therapy using 5-aminolevulinic acid enhances the efficacy of bleomycin. *Ultrasonics*, 2016, vol. 67, pp. 76–84. doi: 10.1016/j.ultras.2016.01.003.
12. Osaki T., Ono M., Uto Y., et al. Bleomycin enhances the efficacy of sonodynamic therapy using aluminum phthalocyanine disulfonate. *Ultrason. Sonochem.*, 2016, vol. 28, pp. 161–168. doi: 10.1016/j.ultsonch.2015.07.013.
13. Xu P., Yao J., Li Z., et al. Therapeutic effect of doxorubicin-chlorin e6-loaded mesoporous silica nanoparticles combined with ultrasound on triple-negative breast cancer. *Int. J. Nanomedicine*, 2020, vol. 15, pp. 2659–2668. doi: 10.2147/IJN.S243037.
14. Sanitary rules and regulations 2.1.2.12-18-2006 «Design, equipment and maintenance of experimental biological clinics (vivariums)» (Resolution of the Chief State Sanitary Doctor of the Republic of Belarus, dated October 31, 2006, №. 131) (in Russian).
15. State standard 33216-2014 «Guide to the maintenance and care of laboratory animals. Rules for keeping and caring for laboratory rodents and rabbits» (in Russian).
16. State standard 33215-2014 «Guide to the care and maintenance of laboratory animals. Rules for equipment of premises and organization of procedures» (in Russian).
17. European Convention for the Protection of Vertebrate Animals Used for Experimental or Other Scientific Purposes (Strasbourg, France, dated March 18, 1986) as amended in accordance with the provisions of the Protocol (ETS №. 170, dated December 2, 2005) (in Russian).
18. Directive 2010/63/EU of the European Parliament and the European Union for the protection of animals used for scientific purposes (dated September 22, 2010) (in Russian).
19. Technical Code 125-2008 «Good Laboratory Practice» (Resolution of the Ministry of Health of the Republic of Belarus №. 56, dated March 28, 2008) (in Russian).
20. Hubrecht R.C., Carter E. The 3Rs and humane experimental technique: implementing change. *Animals (Basel),* 2019, vol. 9(10), pp. 1–10. doi: 10.3390/ani9100754.

ЛИТЕРАТУРА

1. Costley D., McEwan C., Fowley C., et al. Treating cancer with sonodynamic therapy: A review // Int. J. Hyperthermia. – 2015. – Vol. 32(2) – P. 107–117. doi: 10.3109/02656736.2014.992484.
2. Escoffre J.M. and Bouakaz A.B. Therapeutic ultrasound. – Switzerland: Springer, 2016. – 459 p.
3. Rosenthal I., Sostaric J.Z., Riesz R. Sonodynamic therapy – a review of the synergistic effects of drugs and ultrasound // Ultrasonics Sonochem. – 2004. – Vol. 11. – P. 349–363. doi: 10.1016/j.ultsonch.2004.03.004.
4. Yumita T., Nishigaki R., Umemura K., et al. Synergetic effect of ultrasound and hematoporphyrin on sarcoma 180 // J. Jpn. Cancer Res. – Vol. 81. – 1990. – P. 304–308. doi: 10.1111/j.1349-7006.1990.tb02565.x.
5. McHale A.P., Callan J.F., Nomikou N., et al. Sonodynamic therapy: concept, mechanism and application to cancer treatment // Adv. Exp. Med. Biol. – 2016. – Vol. 880. – P. 429–450. doi: 10.1007/978-3-319-22536-4_22.
6. Xu M., Zhou L., Zheng L., et al. Sonodynamic therapy-derived multimodal synergistic cancer therapy // Cancer Lett. – 2021. – Vol. 497. – P. 229–242. doi: 10.1016/j.canlet.2020.10.037.
7. Tzerkovsky D.A., Protopovuch Ya.L., Stupak D.S. Sonodynamic and sono-photodynamic therapy in oncology // Biomedical Photonics. – 2019. – Vol. 8(2). – P. 31–46. https://doi.org/10.24931/2413-9432-2019-8-2-31-46.
8. Liao S., Cai M., Zhu R., et al. Antitumor effect of photodynamic therapy/sonodynamic therapy/sono-photodynamic therapy of chlorin e6 and other applications // Mol. Pharm. – 2023. – Vol. 20(2). – P. 875–885. doi: 10.1021/acs.molpharmaceut.2c00824.
9. Gao H.J., Zhang W.M., Wang X.H., et al. Adriamycin enhances the sonodynamic effect of chlorin e6 against the proliferation of human breast cancer MDA-MB-231 cells *in vitro* // Nan. Fang Yi Ke Da Xue Xue Bao. – 2010. – Vol. 30(10). – P. 2291–2294.
10. Liang L., Xie S., Jiang L., et al. The combined effects of hematoporphyrin monomethyl ether-SDT and doxorubicin on the proliferation of QBC939 cell lines // Ultrasound. Med. Biol. – 2013. – Vol. 39(1). – P. 146–160. doi: 10.1016/j.ultrasmedbio.2012.08.017.
11. Osaki T. et al. Sonodynamic therapy using 5-aminolevulinic acid enhances the efficacy of bleomycin // Ultrasonics. – 2016. – Vol. 67. – P. 76–84.
12. Osaki T., Ono M., Uto Y., et al. Bleomycin enhances the efficacy of sonodynamic therapy using aluminum phthalocyanine disulfonate // Ultrason. Sonochem. – 2016. – Vol. 28. – P. 161–168. doi: 10.1016/j.ultras.2016.01.003.
13. Xu P., Yao J., Li Z., et al. Therapeutic effect of doxorubicin-chlorin e6-loaded mesoporous silica nanoparticles combined with ultrasound on triple-negative breast cancer // Int. J. Nanomedicine. – 2020. – Vol. 15. – P. 2659–2668. doi: 10.2147/IJN.S243037.
14. Санитарные правила и нормы 2.1.2.12-18-2006 «Устройство, оборудование и содержание экспериментально-биологических клиник (вивариев)» (Постановление Главного государственного санитарного врача Республики Беларусь, от 31.10.2006 г. № 131).
15. ГОСТ 33216-2014 «Руководство по содержанию и уходу за лабораторными животными. Правила содержания и ухода за лабораторными грызунами и кроликами».
16. ГОСТ 33215-2014 «Руководство по содержанию и уходу за лабораторными животными. Правила оборудования помещений и организации процедур».
17. Европейская конвенция о защите позвоночных животных, используемых для экспериментов или в иных научных целях (г. Страсбург, Франция, от 18.03.1986 г.) с изменениями в соответствии с положениями Протокола (СЕД № 170 от 02.12. 2005 г.).
18. Директива 2010/63/EU Европейского парламента и Европейского союза по охране животных, используемых в научных целях (от 22.09.2010 г.).
19. 19.ТПК 125-2008 «Надлежащая лабораторная практика» (Постановление Министерства здравоохранения Республики Беларусь № 56 от 28.03.2008 г.).
20. Hubrecht R.C., Carter E. The 3Rs and humane experimental technique: implementing change // Animals (Basel). – 2019. – Vol. 9(10). – P. 1–10. doi: 10.3390/ani9100754.

21. Olyushin V.E., Kukanov K.K., Nechaeva A.S., et. al. Photodynamic therapy in neurooncology. *Biomedical Photonics*, 2023, vol. 12(3), pp. 25–35. doi: 10.24931/2413-9432-2023-12-3-25-3518.
22. Panaseykin Y.A., Kapinus V.N., Filonenko E.V., et al. Photodynamic therapy in treatment of squamous cell carcinoma of oral cavity with chlorine e6 photosensitizer with long-term follow up. *Biomedical Photonics*, 2024, vol. 13(1), pp. 28–38. https://doi.org/10.24931/2413-9432-2023-13-1-28-38.
23. Tseimakh A.E., Mitshenko A.N., Kurtukov V.A., et al. Effectiveness of palliative photodynamic therapy for unresectable biliary cancer. Systematic review and meta-analysis. *Biomedical Photonics*, 2024, vol. 13(2), pp. 34–42. https://doi.org/10.24931/2413-9432-2024-13-2-34-42.
24. Trushina O.I., Filonenko E.V., Novikova E.G., et al. Photodynamic therapy in the prevention of HPV-induced recurrences of precancer and initial cancer of the cervix. *Biomedical Photonics*, 2024, vol. 13(3), pp. 42–46. https://doi.org/10.24931/241-9432-2024-13-3-42-46.
25. Ciambella C.C., Takabe K. Cryotherapy in the treatment of early-stage breast cancer. *World J. Oncol*., 2024, vol. 15(5), pp. 737–743. doi: 10.14740/wjon1909.
26. Pio F., Murdock A., Fuller R.E., et al. The role of whole-gland and focal cryotherapy in recurrent prostate cancer. *Cancers (Basel)*, 2024, vol. 16(18), pp. 3325. doi: 10.3390/cancers16183225.
27. Peeters H., van Zwol E.M., Brancato L., et al. Systematic review of the registered clinical trials for oncological hyperthermia treatment. *Int. J. Hyperthermia*, 2022, vol. 39(1). – pp. 806–812. doi: 10.1080/02656736.2022.2076292.

21. Olyushin V.E., Kukanov K.K., Nechaeva A.S., et. al. Photodynamic therapy in neurooncology // Biomedical Photonics. – 2023. – Vol. 12(3). – P. 25–35. doi: 10.24931/2413-9432-2023-12-3-25-3518.
22. Panaseykin Y.A., Kapinus V.N., Filonenko E.V., et al. Photodynamic therapy in treatment of squamous cell carcinoma of oral cavity with chlorine e6 photosensitizer with long-term follow up // Biomedical Photonics. – 2024. – Vol. 13(1). – P. 28–38. https://doi.org/10.24931/2413-9432-2023-13-1-28-38.
23. Tseimakh A.E., Mitshenko A.N., Kurtukov V.A., et al. Effectiveness of palliative photodynamic therapy for unresectable biliary cancer. Systematic review and meta-analysis // Biomedical Photonics. – 2024. – Vol. 13(2). – P. 34–42. https://doi.org/10.24931/2413-9432-2024-13-2-34-42.
24. Trushina O.I., Filonenko E.V., Novikova E.G., et al. Photodynamic therapy in the prevention of HPV-induced recurrences of precancer and initial cancer of the cervix // Biomedical Photonics. – 2024. – Vol. 13(3). P. 42–46. https://doi.org/10.24931/241-9432-2024-13-3-42-46.
25. Ciambella C.C., Takabe K. Cryotherapy in the treatment of early-stage breast cancer // World J. Oncol. – 2024. – Vol. 15(5). – P. 737–743. doi: 10.14740/wjon1909.
26. Pio F., Murdock A., Fuller R.E., et al. The role of whole-gland and focal cryotherapy in recurrent prostate cancer // Cancers (Basel). – 2024. – Vol. 16(18). – P. 3325. doi: 10.3390/cancers16183225.
27. Peeters H., van Zwol E.M., Brancato L., et al. Systematic review of the registered clinical trials for oncological hyperthermia treatment // Int. J. Hyperthermia. – 2022. – Vol. 39(1). – P. 806–812. doi: 10.1080/02656736.2022.2076292.

PHOTODYNAMIC THERAPY OF CUTANEOUS SQUAMOUS CELL CARCINOMA

Filonenko E.V.[1], **Ivanova-Radkevich V.I.**[2]
[1]P.A. Herzen Moscow Oncology Research Center – branch of FSBI NMRRC of the Ministry of Health of the Russian Federation, Moscow, Russia
[2]Peoples' Friendship University of Russia (RUDN University), Moscow, Russia

Abstract

Photodynamic therapy has traditionally been used and approved in many countries for the treatment of intraepithelial forms of cutaneous squamous cell carcinoma and precancer - actinic keratosis and Bowen's disease. However, recently a number of studies have been conducted that suggest a possible expansion of the boundaries of photodynamic therapy for cutaneous squamous cell carcinoma. Several authors have suggested a therapeutic effect of photodynamic therapy for superficial, microinvasive and well-differentiated cutaneous squamous cell carcinoma. We reviewed publications on the website https://pubmed.ncbi.nlm.nih.gov devoted to this problem. Analysis of the research results shows that photodynamic therapy can achieve high efficiency and good cosmetic results in patients with microinvasive cutaneous squamous cell carcinoma, and in some cases even with an invasive form, and can be considered as an alternative to surgical treatment in patients with contraindications to surgery.

Keywords: photodynamic therapy, cutaneous squamous cell carcinoma, 5-aminolevulinic acid, 5-aminolevulinic acid methyl ester, chlorin e6.

Contacts: Filonenko E.V., e-mail: elena.filonenko@list.ru.

For citations: Filonenko E.V., Ivanova-Radkevich V.I. Photodynamic therapy of cutaneous squamous cell carcinoma, *Biomedical Photonics*, 2024, vol. 13, no. 4, pp. 33–39. doi: 10.24931/2413–9432–2024–13–4–33–39

ФОТОДИНАМИЧЕСКАЯ ТЕРАПИЯ БОЛЬНЫХ ПЛОСКОКЛЕТОЧНЫМ РАКОМ КОЖИ

Е.В. Филоненко[1], **В.И. Иванова-Радкевич**[2]
[1]«Московский научно-исследовательский онкологический институт им. П.А. Герцена – филиал ФГБУ «Национальный медицинский исследовательский центр радиологии» Министерства здравоохранения Российской Федерации, Москва, Россия
[2]Российский Университет дружбы народов, Москва, Россия

Резюме

Фотодинамическая терапия традиционно применяется и одобрена во многих странах для лечения внутриэпителиальных форм плоскоклеточного рака и предрака – актинического кератоза и болезни Боуэна. Однако в последнее время был проведен ряд исследований, позволяющих сделать предположение о возможном расширении границ применения фотодинамической терапии при плоскоклеточном раке кожи. Несколькими авторами было высказано предположение о терапевтическом эффекте фотодинамической терапии при поверхностном, микроинвазивном и хорошо дифференцированном плоскоклеточном раке кожи. Мы провели обзор публикаций на сайте https://pubmed.ncbi.nlm.nih.gov, посвященных этой проблеме. Анализ результатов исследований показывает, что фотодинамическая терапия может позволить достичь высокой эффективности и хороших косметических результатов у пациентов с микроинвазивным плоскоклеточным раком кожи, а в ряде случаев – даже с инвазивной формой, и может быть рассмотрена, как альтернатива хирургическому лечению у пациентов с противопоказаниями к оперативному вмешательству.

Ключевые слова: фотодинамическая терапия, плоскоклеточный рак кожи, 5-аминолевулиновая кислота, метиловый эфир 5-аминолевулиновой кислоты, хлорин е6.

Контакты: Филоненко Е.В., e-mail: elena.filonenko@list.ru.

Для цитирования: Филоненко Е.В., Иванова-Радкевич В.И. Фотодинамическая терапия больных плоскоклеточным раком кожи // Biomedical Photonics. – 2024. – Т. 13, № 4. – С. 33–39. doi: 10.24931/2413–9432–2024–13–4–33–39

Introduction

Cutaneous squamous cell carcinoma (cSCC) is the second most common non-melanocytic skin tumor after basal cell carcinoma. In the Russian Federation (as in many countries around the world), when analyzing cancer statistics, cSCC is not taken into account separately from other non-melanocytic skin tumors, however, according to some data, cSCC accounts for up to 15-20% of all skin cancer cases [1]. In 2023, the incidence of non-melanocytic malignant skin neoplasms in Russia was 305.5 cases per 100 thousand population [2]. Thus, according to indirect estimates, the incidence of cSCC is about 60 cases per 100 thousand population.

Clinical manifestations

The lesions of cSCC most often have a dense structure with a smooth surface or look like a hyperkeratotic papule or plaque, in the center of which an ulcer may be located. In some cases, the lesion of cSCC may look like a non-healing ulcerated wound that bleeds with minimal trauma [3].

Stages of dissemination

The main precursor of cSCC is actinic keratosis (AK). These two pathologies can be considered as different stages of development of one pathological process with transformation of epidermal keratinocytes [4]. The main ways of development and dissemination of cSCC are local infiltration and proliferation. In some cases, dissemination can occur along nerves and blood and lymphatic vessels. cSCC is characterized by a fairly high frequency of metastasis to the lymph nodes – an average of 3% [5,6]. Most authors note that the risk of metastasis in patients with weakened immunity is higher than with normal functioning of the immune system [7].

The frequency of degeneration of AK foci into cSCC varies significantly from one study to another. On average, it is believed that in about 60% of cases, cSCC develops in the area of AK foci, and there is a clear relationship between the number of actinic keratosis formations and the risk of malignant transformation. However, although AK is considered a risk factor and a possible marker for subsequent invasive cSCC, it should be noted that a number of authors provide data that up to half of AK lesions disappear on their own within 1 year [8].

Non-invasive forms of cSCC (in situ) include Bowen's disease and erythroplasia of Queyrat. When the invasion of the papillary dermis occurs, it is called microinvasive cSCC; when the tumor spreads further into the skin, cSCC is considered invasive [9,10].

Diagnosis

There are several biopsy techniques for taking samples of lesions that may be skin cancer. Initial tissue sampling is usually done by curettage if the lesion is raised, or by punch biopsy of the most abnormal areas of the skin [3].

Therapy

The standard treatment for invasive cSCC is surgical removal of the tumor lesion. However, for some patients, the possibility of surgical removal of the cSCC lesion may be limited due to age, general health, concomitant anticoagulant or immunosuppressive therapy, and allergy to local anesthetics. For such patients, the development of other treatment methods is relevant. According to some guidelines, if surgical removal of the cSCC lesion is not possible, there is a possibility of treating low-risk tumors with radiation therapy. However, as many studies show, radiation therapy is not effective enough for cSCC. In addition, post-radiation skin syndrome may worsen over time, and radiation therapy is usually not prescribed to patients under 55 years of age [3,8,9]. Treatment with cryotherapy, imiquimod, and 5-fluorouracil is associated with poor outcome and a high recurrence rate [11].

Another alternative treatment for cSCC is photodynamic therapy (PDT). PDT demonstrates high efficiency and is approved in Russia and abroad for the treatment of many tumor and precancerous skin diseases [12-15]. In particular, our recent review showed that PDT can be considered as one of the first-line treatment options for in situ cSCC. An analysis of articles devoted to PDT in monotherapy in patients with Bowen's disease demonstrated that PDT is more effective and safer than 5-fluorouracil and cryotherapy and is well tolerated by patients with minimal side effects and an excellent cosmetic result, which is important for patients with non-invasive cSCC lesions on the face and exposed skin areas [16].

However, at present, there is insufficient evidence from large randomized multicenter studies regarding the efficacy of PDT as a treatment for invasive cSCC [17] and there is insufficient evidence to support the routine use of local PDT in cSCC [18]. There are only a few studies evaluating the efficacy and tolerability of PDT for microinvasive and invasive cSCC. According to some authors, although local PDT is quite effective for superficial lesions of cSCC, it is less effective for thicker tumors, mainly due to inefficient absorption of 5-aminolevulinic acid (5-ALA) and its derivatives, uneven distribution of photoactive protoporphyrin IX, and limited penetration of light into deeper tumor tissues [18].

The table provides summary data on the effectiveness of PDT in patients with microinvasive and invasive cSCC. The articles were searched on the website https://pubmed.ncbi.nlm.nih.gov for the period 1995-2024 using the keywords "invasive OR minimally invasive OR microinvasive" AND "cutaneous squamous cell carcinoma" AND "photodynamic therapy".

In a randomized clinical study by Choi S.H. et al., 24 patients with microinvasive cSCC underwent 2 courses of

Таблица
Сводные данные результативности применения фотодинамической терапии у пациентов с микроинвазивным и инвазивным плоскоклеточным раком кожи

Table
Summary of the effectiveness of photodynamic therapy of microinvasive and invasive cutaneous squamous cell carcinoma

Авторы Authors	Число пациентов / количество очагов / No. of patients/ No. of lesions		Фотосенсибилизатор Photosensitizer	Режим облучения Light wavelength	Количество курсов ФДТ Number of PDT courses	Эффективность ФДТ PDT efficiency	Нежелательные реакции Adverse reactions
Calzavara-Pinton P.G. et al., 2008 [10]	71 очаг 71 lesions	Микроинвазивный и инвазивный ПКРК Microinvasive and invasive cSCC	МЭ-АЛК за 3 ч до облучения MAL 3 hours before irradiation	37 Дж/см^2 37 J/cm^2	2 курса с интервалом 1 нед. 2 courses with an interval of 1 week	Полная регрессия очагов через 3 мес: микроинвазивного ПКРК 80,0%, инвазивного ПКРК – 45,2%. Полная регрессия очагов через 24 мес: микроинвазивного ПКРК 57,5%, инвазивного ПКРК – 25,8%. Complete regression of foci after 3 months: microinvasive cSCC 80.0%, invasive cSCC – 45.2%. Complete regression of foci after 24 months: microinvasive cSCC 57.5%, invasive cSCC – 25.8%	Эритрема, отек, слабые болевые ощущения во время светового воздействия Erythema, swelling, mild pain during light exposure
Choi S. H. et al., 2017 [19]	24 пациента 24 patients	Микроинвазивный ПКРК Microinvasive cSCC	МЭ-АЛК за 3 ч до облучения MAL 3 hours before irradiation	37 Дж/см^2 37 J/cm^2	2 курса с интервалом 1 нед. 2 courses with an interval of 1 week	Полная регрессия очагов микроинвазивного ПКРК через 3 месяца 52,4%. Число рецидивов через 24 месяца – 63,6% Complete regression of microinvasive cSCC after 3 months 52.4%. The number of relapses after 24 months is 63.6%	Нет данных No data
Kubler A.C. et al., 2001 [20]	25 пациентов 25 patients	ПКРК губы Tis, T1, T2/N0/M0 cSCC of lips Tis, T1, T2/N0/M0	Темопорфин 0,15 мг/кг за 96 ч до облучения Temoporfin 0.15 mg/kg 96 hours before irradiation	20 Дж/см^2 20 J/cm^2	1 курс 1 course	Полная регрессия очагов ПКРК через 3 месяца 96%. Рецидивы через 4 (1 пациент) и 18 мес (1 пациент) Complete regression of cSCC foci after 3 months 96%. Relapses after 4 (1 patient) and 18 months (1 patient)	Нет данных No data
Капинус В.Н. и соавт. Kapinus V.N. et al., 2014 [21]	51 пациент 51 patients	ПКРК Т1-3 cSCC T1-3	Фотолон (хлорин е6) 1,1-1,6 мг/кг внутривенно Photolon (chlorin e6) 1.1-1.6 mg/kg intravenously	100-600 Дж/см^2 100-600 J/cm^2	1-2 курса 1-2 courses	Полная регрессия у 91,7% пациентов, частичная регрессия – у 8,3%. При сроке наблюдения от 6 мес до 5 лет рецидивы были диагностированы у 31,2% пациентов Complete regression in 91.7% of patients, partial regression – in 8.3%. With an observation period of 6 months to 5 years, relapses were diagnosed in 31.2% of patients	Нет данных No data

Fargnole M.C. et al., 2015 [22]	1 пациент 1 patient	Микроинвазивный ПКРК губы Microinvasive cSCC of lips	МЭ-АЛК за 3 ч до облучения MAL 3 hours before irradiation	37 Дж/см^2 37 J/cm^2	2 курса 2 courses	Полная регрессия. 24 мес наблюдения без рецидива Complete regression. 24 months of observation without relapse	Нет данных No data
Sotiriou E. et al., 2010 [23]	1 пациент 1 patient	Инфильтративный ПКРК щеки Infiltrative cSCC of the cheek	5-АЛК за 4 ч до облучения, внутриочаговое введение 5-ALA 4 hours before irradiation, intralesional administration	100 Дж/см^2 100 J/cm^2	1 курс 1 course	Полная регрессия. 16 мес наблюдения без рецидива Complete regression. 16 months of observation without relapse	Нет данных No data
Li Q. et al., 2010 [24]	1 пациент 1 patient	Инвазивный ПКРК головы (толщина опухоли 5,5 мм) Invasive cSCC of the head (tumor thickness 5.5 mm)	Местно 5-АЛК за 6 ч до облучения Locally 5-ALA 6 hours before irradiation	100 Дж/см^2 100 J/cm^2	7 курсов 7 courses	Полная регрессия, наблюдение без рецидива 12 мес Complete regression, 12 months of observation without relapse	Нет данных No data
Rossi R. et al., 2004 [25]	1 пациент 1 patient	ПКРК века cSCC of the eyelid	Местно 5-АЛК за 4 ч до облучения Locally 5-ALA 4 hours before irradiation	80 Дж/см^2 80 J/cm^2	1 курс 1 course	Полная регрессия, наблюдение без рецидива 6 мес Complete regression, 6 months of observation without relapse	Нет данных No data
Струнки Д.Н. и соавт. Strunkin D.N. et al., 2017 [26]	1 пациент 1 patient	ПКРК щеки 4х4 см (прорастание в кожу, инфильтрация подкожной сетчатки) cSCC of the cheek 4x4 cm (ingrowth into the skin, infiltration of the subcutaneous retina)	Внутривенно 0,8 мг/кг фотодитазина (хлорин е6) за 2,5 ч до облучения Intravenously 0.8 mg/kg photoditazine (chlorin e6) 2.5 hours before irradiation	300-350 Дж/см^2 300-350 J/cm^2	1 курс 1 course	Частичная регрессия через 2 мес Partial regression after 2 months	Нет данных No data

*ПКРК – плоскоклеточный рак кожи, 5-АЛК – 5-аминолевулиновая кислота, МЭ-АЛК – метиловый эфир 5-аминолевулиновой кислоты
*cSCC – cutaneous squamous cell carcinoma, 5-ALA – 5-aminolevulinic acid, MAL – 5-aminolevulinic acid methyl ester

PDT with 5-ALA [19]. The study also included 21 patients who underwent 1 course of PDT with preliminary treatment of the cSCC lesion with an ablative fractional laser. The overall complete response rate 3 months after 2 courses of PDT was 52.4%. It should be noted that the use of an ablative laser increased this figure to 84.2%. However, both treatment approaches did not have significant differences in terms of cosmetic results, side effects, or pain intensity.

Calzavara-Pinton P.G. et al. reported the efficacy of PDT with 5-ALA in the treatment of cSCC depending on the depth of invasion [10]. The authors of the article staged cSCC taking into account the level of invasion according to Clark, which shows to what layer of the skin the tumor has spread. The authors assigned level I to cSCC in situ (Bowen's disease), level II (invasion into the papillary dermis) to microinvasive cSCC, and levels III-V to invasive cSCC. The results of the study confirmed the higher efficacy of PDT in relation to microinvasive cSCC (level II according to Clark, invasion into the papillary dermis) compared to invasive variants of cSCC (level III and IV according to Clark). Complete regression 3 months after 2 courses of PDT was achieved in 80.0% of cases of microinvasive cSCC and only in 45.2% of cases of invasive cSCC (Clark levels III and IV). For comparison, when using PDT in patients with cSCC in situ (Bowen's disease), the frequency of complete regressions was slightly higher than in the case of the microinvasive form of the tumor – 87.8%. With long-term observation, the effect in patients with the microinvasive form of cSCC was significantly more stable than in patients with invasive cSCC: after 24 months, complete regression was preserved in 57.5% of cases of microinvasive cSCC and in 25.8% of cases of the invasive form of the disease.

One of the largest studies of the effectiveness of PDT in cSCC (51 patients) was conducted in Russia [21]. Patients underwent PDT after intravenous administration of photolon, a photosensitizer based on chlorin e6. In 24 patients (47.1%), the diagnosis was made for the first time, 27 patients (52.9%) were treated for continued growth or relapse of cSCC after radiation therapy, surgery, cryodestruction, and combined treatment. Among patients with primary cSCC, T1 was established in 7 (29.2%), T2 in 16 (66.7%), and T3 in 1 (4.2%) people. Among these patients, complete regression of tumor foci was achieved in 91.7% of patients and partial in 8.3%. Among patients with recurrent cSCC, the tumor sizes ranged from 2.0 to 5.0 cm in 40.7%, and 5.0 cm or more in 59.3%. Among these patients, complete regression was achieved only in 59.3% of cases, partial regression in 33.3%, and no effect in 7.4%. With an observation period of 6 months to 5 years, recurrent CCRC were diagnosed in 31.2% of patients.

Another large study involving 25 patients from 5 centers in 3 countries was published by Kubler et al. [20]. This was a prospective, open-label, multicenter study conducted on patients with early-stage lip cSCC. The authors used temoporfin (0.15 mg/kg intravenously) as a photosensitizer. The interval between the administration of the photosensitizer and irradiation (20 J/cm^2) was 4 days. The complete response rate at 3 months after treatment was 96%. During the dynamic observation, relapse of cSCC was registered in 2 patients: 4 and 18 months after treatment.

The remaining publications we found were reports of individual clinical observations in which PDT demonstrated high efficacy against microinvasive cSCC (Table).

Discussion

As is known, the method of choice in the treatment of patients with cSCC is surgical removal of tumor foci [3,5,9]. However, for a significant cohort of patients, there are limitations in performing surgical intervention. This may be due to the age of the patients, somatic status, or concomitant therapy. For this cohort of patients, the development of non-invasive methods for influencing cSCC foci is relevant. The use of iquimod and 5-fluorouracil often does not achieve acceptable efficiency [11,16]. Superficial ablative techniques such as electrodissection and curettage, cryotherapy, and the use of CO_2 laser have not shown high efficiency and, thus, the validity of their use for the treatment of invasive cSCC is highly questionable [11]. The use of chemotherapy and radiation therapy are associated with multiple side effects. PDT in the treatment of non-invasive cSCC has a number of advantages, which include relatively less invasiveness, high selectivity for tumor tissue, no serious side effects, good cosmetic results, low recurrence rates, and relative safety for elderly patients and patients with comorbid conditions for which surgical intervention is inappropriate [10,19-26]. Despite all these advantages, PDT still requires some modifications to be successfully used in invasive cSCC [10]. The main reason for the low efficiency of local PDT in invasive cSCC may be insufficient penetration of the topically applied photosensitizer through tumor tissue or insufficient local bioavailability and, as a result, decreased cellular absorption. Studies to increase the efficiency of photosensitizers in relation to cSCC are mainly aimed at developing methods to increase drug penetration and achieve the desired concentration of the photosensitizer in the tumor lesion. To increase the delivery of photosensitizer to tumor cells, a combination of PDT with various methods of physical action and optimization of medicinal forms of photosensitizers is used, facilitating the penetration of the photosensitizer deep into the tissue [11].

For example, in the study by Sotiriou E. et al., intralesional administration of the photosensitizer was used to achieve the maximum concentration of the drug in the tumor focus [20]. This approach allowed achieving

complete regression of the infiltrative cSCC focus after just 1 course of PDT with 5-aminolevulinic acid methyl ester, and the relapse-free observation period was 16 months. Another promising direction is the use of nanoforms for encapsulation of the photosensitizer [27,28].

A number of studies have attempted to increase the efficacy of PDT for invasive cSCC by combining it with other physical or chemotherapeutic modalities. As discussed earlier, Choi S.H. et al. [16] showed that pretreatment of cSCC lesions with an ablative laser resulted in complete regression in more cases than PDT monotherapy, although no significant differences were observed in both cases in terms of cosmetic outcomes, adverse events, or pain intensity. Another study showed in cell culture experiments that metformin pretreatment could inhibit metabolic changes in cSCC cells during PDT treatment and reduce tumor cell survival, and this effect was confirmed in *in vivo* experiments where metformin pretreatment increased the efficacy of PDT with intratumoral administration of MAL [29]. Anand F. et al. demonstrated increased accumulation of photoactive protoporphyrin IX in cSCC cells after 3-day pretreatment of tumor lesions with 5-fluorouracil [30], which resulted in greater tumor cell death. Another mechanism, according to the authors, may be related to the fact that exposure to 5-fluorouracil could cause changes in the expression of key enzymes of protoporphyrin IX metabolism, including coproporphyrinogen oxidase and ferrochelatase.

Regarding the efficacy of various photosensitizers used for PDT of invasive cSCC, the number of studies in this area is not large enough to speak of a statistically significant difference, but there is an obvious trend towards higher efficacy when using photosensitizers based on chlorin e6 [10,19-21].

Conclusion

Photodynamic therapy can achieve high efficiency and good cosmetic results in patients with microinvasive cSCC, and in some cases even with the invasive form, and can be considered as an alternative to surgical treatment in patients with contraindications to surgery. In invasive cSCC, the use of photosensitizers based on chlorin e6 is preferable, as they demonstrate higher efficiency.

REFERENCES

1. Rogers H.W., Weinstock M.A., Harris A.R., Hinckley M.R., Feldman S.R., Fleischer A.B., Coldiron B.M. Incidence estimate of nonmelanoma skin cancer in the United States, 2006. *Arch Dermatol*, 2010, Vol. 146(3), pp. 283-287.
2. Edited by A.D. Kaprin, V.V. Starinsky, A.O. Shakhzadova. The state of cancer care for the Russian population in 2023. – Moscow: *P.A. Herzen Moscow State Medical Research Institute – branch of the Federal State Budgetary Institution "NMIC of Radiology" of the Ministry of Health of the Russian Federation*, 2024, p. 262.
3. Firnhaber J.M. Basal cell and cutaneous squamous cell carcinomas: diagnosis and treatment. *American family physician*, 2020, Vol. 102(6), pp. 339-346.
4. Rosen T., Lebwohl M.G. Prevalence and awareness of actinic keratosis: barriers and opportunities. *Journal of the American Academy of Derma-tology*, 2013, Vol. 68(1), pp. S2-S9.
5. Karia P.S., Han J., Schmults C.D. Cutaneous squamous cell carcinoma: estimated incidence of disease, nodal metastasis, and deaths from disease in the United States, 2012. *Journal of the American Academy of Dermatology*, 2013, Vol. 68(6), pp. 957-966.
6. Ignatova A.V. Actual problems of treatment of locally advanced and metastatic squamous cell skin cancer, *Modern oncology,* 2021, Vol. 23(1), pp. 94-98.
7. Nehal K.S., Bichakjian C.K. Update on keratinocyte carcinomas. *New England Journal of Medicine*, 2018, Vol. 379(4), pp. 363-374.
8. Dirschka T. et al. Real-world approach to actinic keratosis management: practical treatment algorithm for office-based dermatology. *Journal of Dermatological Treatment*, 2017, Vol. 28(5), pp. 431-442.
9. Clinical recommendations of the Russian Federation 2020 «Squamous cell skin cancer».
10. Calzavara-Pinton P. G. et al. Methylaminolaevulinate-based photodynamic therapy of Bowen's disease and squamous cell carcinoma. *British Journal of Dermatology*, 2008, Vol. 159(1), pp. 137-144.
11. Keyal U. et al. Present and future perspectives of photodynamic therapy for cutaneous squamous cell carcinoma. *Journal of the American Academy of Dermatology*, 2019, Vol. 80(3), pp. 765-773.

ЛИТЕРАТУРА

1. Rogers H.W., Weinstock M.A., Harris A.R., Hinckley M.R., Feldman S.R., Fleischer A.B., Coldiron B.M. Incidence estimate of nonmelanoma skin cancer in the United States, 2006 // Arch Dermatol. – 2010. – Vol. 146(3). – P. 283-287.
2. Под ред. А.Д. Каприна, В.В. Старинского, А.О. Шахзадовой. Состояние онкологической помощи населению России в 2023 году. – Москва: МНИОИ им. П.А. Герцена – филиал ФГБУ «НМИЦ радиологии» Минздрава России. – 2024. – С. 262.
3. Firnhaber J.M. Basal cell and cutaneous squamous cell carcinomas: diagnosis and treatment // American family physician. – 2020. – Vol. 102(6). – P. 339-346.
4. Rosen T., Lebwohl M.G. Prevalence and awareness of actinic keratosis: barriers and opportunities // Journal of the American Academy of Dermatology. – 2013. – Vol. 68(1). – P. S2-S9.
5. Karia P.S., Han J., Schmults C.D. Cutaneous squamous cell carcinoma: estimated incidence of disease, nodal metastasis, and deaths from disease in the United States, 2012 // Journal of the American Academy of Dermatology. – 2013. – Vol. 68(6). – P. 957-966.
6. Игнатова А.В. Актуальные проблемы лечения местно-распространенного и метастатического плоскоклеточного рака кожи // Современная онкология. – 2021. – Т. 23. – №. 1. – С. 94-98.
7. Nehal K.S., Bichakjian C.K. Update on keratinocyte carcinomas // New England Journal of Medicine. – 2018. – Vol. 379(4). – P. 363-374.
8. Dirschka T. et al. Real-world approach to actinic keratosis management: practical treatment algorithm for office-based dermatology // Journal of Dermatological Treatment. – 2017. – Vol. 28(5). – P. 431-442.
9. Клинические рекомендации РФ 2020 «Плоскоклеточный рак кожи».
10. Calzavara-Pinton P.G. et al. Methylaminolaevulinate-based photodynamic therapy of Bowen's disease and squamous cell carcinoma // British Journal of Dermatology. – 2008. – Vol. 159(1). – P. 137-144.
11. Keyal U. et al. Present and future perspectives of photodynamic therapy for cutaneous squamous cell carcinoma // Journal of the American Academy of Dermatology. – 2019. – Vol. 80(3). – P. 765-773.

12. Filonenko E.V., Okushko S.S. Actinic keratosis (review of literature). *Biomedical Photonics*, 2022, Vol. 11(1), pp. 37-48. doi: 10.24931/2413–9432–2022–11-1-37-48.
13. Kaprin A.D., Ivanova-Radkevich V.I., Urlova A.N., Asratov A.T., Gushchina Yu.,Sh., Libo L., Xiaojun C., Filonenko E.V. Photodynamic therapy opportunities for the treatment of erythroplasia of Queyrat. *Biomedical Photonics*, 2020, Vol. 9(1), pp. 34-41. doi: 10.24931/2413–9432–2020–9-1–34–41
14. Filonenko E.V., Ivanova-Radkevich V.I. Photodynamic therapy in the treatment of extramammary Paget disease. *Biomedical Photonics*, 2022, Vol. 11(3), pp. 24-34. doi: 10.24931/2413–9432–2022–11-3-24–34.
15. Filonenko E.V., Ivanova-Radkevich V.I. Photodynamic therapy in the treatment of patients with mycosis fungoides. *Biomedical Photonics*, 2022, Vol. 11(1), pp. 27-36. doi: 10.24931/2413–9432–2022–11-1-27-37
16. Filonenko E.V., Ivanova-Radkevich V.I. Photodynamic therapy of patients with Bowen's disease. *Biomedical Photonics*, 2024, Vol. 12(4). – pp. 22-29.
17. Wong T.H. et al. British Association of Dermatologists and British Photodermatology Group guidelines for topical photodynamic therapy 2018. *British Journal of Dermatology*, 2019, Vol. 180(4), pp. 730-739.
18. Xu M., Kong L., Jamil M. Advancements in skin cancer treatment: focus on photodynamic therapy: a review. *American Journal of Cancer Research*, 2024, Vol. 14(10), pp. 5011.
19. Choi S.H., Kim K.H., Song K.H. Effect of methyl aminolevulinate photodynamic therapy with and without ablative fractional laser treatment in patients with microinvasive squamous cell carcinoma: a randomized clinical trial. *JAMA dermatology*, 2017, Vol. 153(3), pp. 289-295.
20. Kübler A. C. et al. Treatment of squamous cell carcinoma of the lip using Foscan-mediated photodynamic therapy. *International journal of oral and maxillofacial surgery*, 2001, Vol. 30(6), pp. 504-509.
21. Kapinus V.N., Kaplan M.A., Spichenkova I.S., Shubina A.M., Yaroslavtseva-Isaeva E.V. Photodynamic therapy of epithelial malignant neoplasms of the skin. *Photodynamic therapy and photodiagnostics*, 2014, Vol. 3(3), pp. 9-14.
22. Fargnoli M.C. et al. Photodynamic therapy for the treatment of microinvasive squamous cell carcinoma of the lower lip: a case report. *Giornale italiano di dermatologia e venereologia: organo ufficiale, Societa italiana di dermatologia e sifilografia*, 2014, Vol. 150(3), pp. 331-335.
23. Sotiriou E., Apalla Z., Ioannides D. Complete resolution of a squamous cell carcinoma of the skin using intralesional 5-aminolevulinic acid photodynamic therapy intralesional PDT for SCC. *Photodermatology, Photoimmunology & Photomedicine*, 2010, Vol. 26(5), pp. 269-271.
24. Li Q. et al. Clearance of a thick invasive squamous cell carcinoma after multiple treatments with topical photodynamic therapy. *Photomedicine and Laser Surgery*, 2010, Vol. 28(5), pp. 703-706.
25. Rossi R. et al. Squamous cell carcinoma of the eyelid treated with photodynamic therapy. *Journal of chemotherapy*, 2004, Vol. 16(3), pp. 306-309.
26. Strunkin D.N., Zharikova I.P., Kozhevnikov Yu.A., Zadontseva N.S. Photodynamic therapy of squamous cell carcinoma of the cheek skin (clinical observation). *Biomedical Photonics*, 2017, Vol. 6(2), pp. 38-40.
27. Wang X. et al. Treating cutaneous squamous cell carcinoma using 5-aminolevulinic acid polylactic-co-glycolic acid nanoparticle-mediated photodynamic therapy in a mouse model. *International journal of nanomedicine*, 2015, pp. 347-355.
28. Shi L. et al. *In vitro* evaluation of 5-aminolevulinic acid (ALA) loaded PLGA nanoparticles. *International Journal of Nanomedicine*, 2013, pp. 2669-2676.
29. Mascaraque-Checa M. et al. Metformin overcomes metabolic reprogramming-induced resistance of skin squamous cell carcinoma to photodynamic therapy. *Molecular metabolism*, 2022, Vol. 60, pp. 101496.
30. Anand S. et al. Fluorouracil enhances photodynamic therapy of squamous cell carcinoma via a p53-independent mechanism that increases protoporphyrin IX levels and tumor cell death. *Molecular cancer therapeutics*, 2017, Vol. 16(6), pp. 1092-1101.

12. Filonenko E.V., Okushko S.S. Actinic keratosis (review of literature) // Biomedical Photonics. – 2022. – Vol. 11(1). – P. 37-48. doi: 10.24931/2413–9432–2022–11-1-37-48.
13. Kaprin A.D., Ivanova-Radkevich V.I., Urlova A.N., Asratov A.T., Gushchina Yu., Sh., Libo L., Xiaojun C., Filonenko E.V. Photodynamic therapy opportunities for the treatment of erythroplasia of Queyrat // Biomedical Photonics. – 2020. – Vol. 9(1). – P. 34-41. doi: 10.24931/2413–9432–2020–9-1–34–41
14. Filonenko E.V., Ivanova-Radkevich V.I. Photodynamic therapy in the treatment of extramammary Paget disease // Biomedical Photonics. – 2022. – Vol. 11(3). – P. 24-34. doi: 10.24931/2413–9432–2022–11-3-24–34
15. Filonenko E.V., Ivanova-Radkevich V.I. Photodynamic therapy in the treatment of patients with mycosis fungoides // Biomedical Photonics. – 2022. – Vol. 11(1). – P. 27-36. doi: 10.24931/2413–9432–2022–11-1-27-37
16. Филоненко Е. В., Иванова-Радкевич В. И. Фотодинамическая терапия пациентов с болезнью Боуэна // Biomedical Photonics. – 2024. – Т. 12, №. 4. – С. 22-29.
17. Wong T. H. et al. British Association of Dermatologists and British Photodermatology Group guidelines for topical photodynamic therapy 2018 // British Journal of Dermatology. – 2019. – Vol. 180(4). – P. 730-739.
18. Xu M., Kong L., Jamil M. Advancements in skin cancer treatment: focus on photodynamic therapy: a review // American Journal of Cancer Research. – 2024. – Vol. 14(10). – P. 5011
19. Choi S.H., Kim K.H., Song K.H. Effect of methyl aminolevulinate photodynamic therapy with and without ablative fractional laser treatment in patients with microinvasive squamous cell carcinoma: a randomized clinical trial // JAMA dermatology. – 2017. – Vol. 153(3). – P. 289-295.
20. Kübler A. C. et al. Treatment of squamous cell carcinoma of the lip using Foscan-mediated photodynamic therapy // International journal of oral and maxillofacial surgery. – 2001. – Vol. 30(6). – P. 504-509.
21. Капинус В.Н., Каплан М.А., Спиченкова И.С., Шубина А.М., Ярославцева-Исаева Е.В. Фотодинамическая терапия эпителиальных злокачественных новообразований кожи // Фотодинамическая терапия и фотодиагностика. – 2014. – Т. 3, № 3. – С. 9-14.
22. Fargnoli M.C. et al. Photodynamic therapy for the treatment of microinvasive squamous cell carcinoma of the lower lip: a case report // Giornale italiano di dermatologia e venereologia: organo ufficiale, Societa italiana di dermatologia e sifilografia. – 2014. – Vol. 150(3). – P. 331-335.
23. Sotiriou E., Apalla Z., Ioannides D. Complete resolution of a squamous cell carcinoma of the skin using intralesional 5-aminolevulinic acid photodynamic therapy intralesional PDT for SCC // Photodermatology, Photoimmunology & Photomedicine. – 2010. – Vol. 26(5). – P. 269-271.
24. Li Q. et al. Clearance of a thick invasive squamous cell carcinoma after multiple treatments with topical photodynamic therapy // Photomedicine and Laser Surgery. – 2010. – Vol. 28(5). – P. 703-706.
25. Rossi R. et al. Squamous cell carcinoma of the eyelid treated with photodynamic therapy // Journal of chemotherapy. – 2004. – Vol. 16(3). – P. 306-309.
26. Стрункин Д.Н., Жарикова И.П., Кожевников Ю.А., Задонцева Н.С. Фотодинамическая терапия плоскоклеточного рака кожи щеки (клиническое наблюдение) // Biomedical Photonics. – 2017. – Т. 6, № 2. – С. 38-40.
27. Wang X. et al. Treating cutaneous squamous cell carcinoma using 5-aminolevulinic acid polylactic-co-glycolic acid nanoparticle-mediated photodynamic therapy in a mouse model // International journal of nanomedicine. – 2015. – P. 347-355.
28. Shi L. et al. *In vitro* evaluation of 5-aminolevulinic acid (ALA) loaded PLGA nanoparticles // International Journal of Nanomedicine. – 2013. – P. 2669-2676.
29. Mascaraque-Checa M. et al. Metformin overcomes metabolic reprogramming-induced resistance of skin squamous cell carcinoma to photodynamic therapy // Molecular metabolism. – 2022. – Vol. 60. – P. 101496.
30. Anand S. et al. Fluorouracil enhances photodynamic therapy of squamous cell carcinoma via a p53-independent mechanism that increases protoporphyrin IX levels and tumor cell death // Molecular cancer therapeutics. – 2017. – Vol. 16(6). – P. 1092-1101.

MACHINE LEARNING METHODS FOR SPECTRALLY-RESOLVED IMAGING ANALYSIS IN NEURO-ONCOLOGY

Savelieva T.A.[1,2], Romanishkin I.D.[1], Ospanov A.[2], Linkov K.G.[1], Goryajnov S.A.[3], Pavlova G.V.[3,4], Pronin I.N.[3], Loschenov V.B.[1,2]
[1]Prokhorov General Physics Institute of the Russian Academy of Sciences, Moscow, Russia
[2]National Research Nuclear University MEPhI, Moscow, Russia
[3]N.N. Burdenko National Medical Research Center of Neurosurgery, Moscow, Russia
[4]Institute of Higher Nervous Activity and Neurophysiology of the Russian Academy of Sciences, Moscow, Russia

Abstract

To reduce the frequency of relapses after surgical removal a brain tumor, it is critically important to completely remove all affected areas of the brain without disrupting the functionality of vital organs. Therefore, intraoperative differential diagnostics of micro-areas of tumor tissue with their subsequent removal or destruction is an urgent task that determines the success of the operation as a whole. Optical spectroscopy has shown its advantages over the past decade when used as a tool for intraoperative metabolic navigation. And one of the most promising options for the development of this technology is spectrally-resolved imaging. Currently, methods of spectrally-resolved imaging in diffusely reflected light have been developed, for example, mapping the degree of hemoglobin oxygen saturation, as well as fluorescence visualization systems, for both endogenous fluorophores and special fluorescent markers. These systems allow rapid analysis of tissue by the composition of chromophores and fluorophores, which allows the neurosurgeon to differentiate tumor and normal tissues, as well as functionally significant areas, during surgery. No less mandatory are the methods of using spectrally resolved visualization based on mapping characteristics obtained from Raman spectra, but due to the smaller cross-section of the process, these methods are used *ex vivo*, as a rule, for urgent analysis of fresh tissue samples. In this paper, we focus on both the physical foundations of such methods and a very important aspect of their application - machine learning (ML) methods for image processing and tissues' classification.

Keywords: optical spectroscopy, spectrally-resolved imaging, intracranial tumors, machine learning, fluorescence intraoperative navigation, fluorescence endomicroscopy, Raman microscopy, CARS, Stimulated Raman Histology, hyperspectral images.

Contacts: Savelieva T.A., e-mail: savelevat@gmail.com.

For citations: Savelieva T.A., Romanishkin I.D., Ospanov A., Linkov K.G., Goryajnov S.A., Pavlova G.V., Pronin I.N., Loschenov V.B. Machine learning methods for spectrally-resolved imaging analysis in neuro-oncology, *Biomedical Photonics*, 2024, vol. 13, no. 4, pp. 40–54. doi: 10.24931/2413–9432–2024–13–4–40–54

МЕТОДЫ МАШИННОГО ОБУЧЕНИЯ ДЛЯ АНАЛИЗА СПЕКТРАЛЬНО-РАЗРЕШЕННЫХ ИЗОБРАЖЕНИЙ В НЕЙРООНКОЛОГИИ

Т.А. Савельева[1,2], И.Д. Романишкин[1], А. Оспанов[2], К.Г. Линьков[1], С.А. Горяйнов[3], Г.В. Павлова[3,4], И.Н. Пронин[3], В.Б. Лощенов[1,2]
[1]Институт общей физики им. А.М. Прохорова Российской академии наук, Москва, Россия
[2]Национальный исследовательский ядерный университет «МИФИ», Москва, Россия
[3]НМИЦ нейрохирургии имени академика Н. Н. Бурденко, Москва, Россия
[4]Институт высшей нервной деятельности и нейрофизиологии Российской академии наук, Москва, Россия

Резюме

При проведении хирургических операций по удалению опухолей мозга критически важной для снижения частоты рецидивов является полнота удаления всех пораженных участков мозга без нарушения функциональности жизненно важных органов. Поэтому дифференциальная диагностика микроучастков опухолевой ткани с последующим их удалением или деструкцией является актуальной

задачей, определяющей успех операции в целом. Оптическая спектроскопия за последние десятилетие показала свои преимущества при использовании в качестве инструмента интраоперационной метаболической навигации. И одним из наиболее многообещающих вариантов развития этой технологии является спектрально-разрешенная визуализация. В настоящий момент разработаны методики как спектрально-разрешенной визуализации в диффузно-отраженном свете, позволяющие, например, картировать распределение сатурации гемоглобина кислородом в зоне интереса, так и системы визуализации флуоресценции, как эндогенной, так и индуцированной введением в организм пациента флуоресцентных маркеров. Эти системы обеспечивают быстрый анализ тканей по составу исследуемых хромофоров и флуорофоров, позволяя нейрохирургу во время операции дифференцировать опухолевые и нормальные ткани, а также функционально значимые зоны. Не менее важным направлением применения спектрально-разрешенной визуализации являются методы, основанные на картировании характеристик, получаемых из спектров комбинационного рассеяния, однако, в силу меньшего сечения процесса эти методики используются *ex vivo*, как правило, для срочного анализа только что удаленных образцов тканей. В настоящей работе мы сделаем фокус как на физических основаниях таких методов, так и на весьма важном аспекте их применения – методах машинного обучения для обработки таких изображений и классификации тканей.

Ключевые слова: оптическая спектроскопия, спектрально-разрешенная визуализация, внутричерепные опухоли, машинное обучение, флуоресцентная интраоперационная навигация, флуоресцентная эндомикроскопия, микроскопия комбинационного рассеяния, CARS, стимулированная Рамановская гистология, гиперспектральные изображения.

Контакты: Савельева Т.А., e-mail: e-mail: savelevat@gmail.com.

Для цитирования: Савельева Т.А., Романишкин И.Д., Оспанов А., Линьков К.Г., Горяйнов С.А., Павлова Г.В., Пронин И.Н., Лощенов В.Б. Методы машинного обучения для анализа спектрально-разрешенных изображений в нейроонкологии // Biomedical Photonics. – 2024. – Т. 13, № 4. – С. 40–54. doi: 10.24931/2413–9432–2024–13–4–40–54

Principles of formation of spectrally resolved images

Speaking about spectrally resolved imaging in biomedical applications, it is necessary to have a good understanding of what physical effects of light interaction with biological tissues lead to the formation of these images and why spectral resolution of the recorded signals is required (Fig. 1).

Light incident on a biological object can be reflected from the surface (Fresnel reflectance signal Rf) or pass through without interaction with tissue components (transmission Tc, so-called ballistic photons), but we do not consider these trivial cases in this review. From the diagnostic point of view, we are interested in those variants of light interaction with the tissue that we observe in its volume. First of all, it is necessary to keep in mind that most biological tissues are highly scattering, so light is scattered in tissues many times (this interaction is described by such an optical parameter of tissues as the scattering coefficient μ_s, which is a value inverse to the photon path length in the tissue between scattering acts). Light scattering depends on the size of scattering particles relative to the wavelength of incident light, as well as their concentration, i.e. we can judge about the structural features of tissues by this parameter. We can estimate the value of the scattering coefficient by the

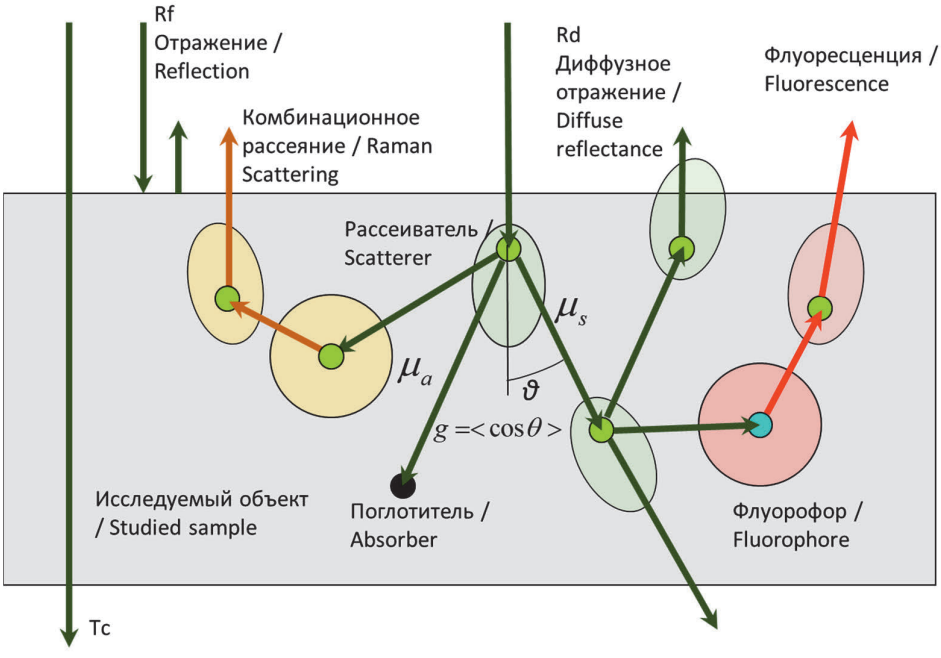

Рис. 1. Взаимодействие света с биологическими тканями.
Fig. 1. Interaction of light with biological tissues.

diffuse scattering signal (in the case of registration from the same side of the tissue from which the illumination was performed, we speak of diffuse reflectance Rd). Another important type of interaction is the absorption of light by the tissue. After light passes through the tissue, we obtain the diffuse reflectance spectrum due not only to light scattering, but also to absorption, since part of the light does not reach the receiver due to absorption, and part due to the fact that it was scattered in other directions. Therefore, from the diffuse reflectance signal, by decomposing the spectrum, it is also possible to extract the absorption spectrum of the tissue, and hence the information about the content of major absorbers, for example, hemoglobin. No less important from the diagnostic point of view is such type of interaction as fluorescence of molecules when they absorb the incident light. We distinguish between Stokes fluorescence (with energy loss due to internal relaxation) and anti-Stokes fluorescence (with energy gain), but the first variant is more probable and is much more often used in medical applications. In this case, while light scattering can occur with different probabilities at different angles (generalized scattering phase functions are indicated by colored ellipses in Fig. 1), the fluorescence signal is emitted isotropically along the direction. However, after that, the fluorescence emission also travels through the medium, scattering and absorbing repeatedly. Thus, when recording the fluorescence spectrum from biological tissues, we must remember that it has been affected by absorption and scattering and in some cases will require correction for these factors. A less probable process, but very valuable from a diagnostic point of view, is the effect of Raman scattering of light. Raman scattering is a physical process in which not only the direction of the incident light but, more importantly, the energy of the light changes as a result of the interaction. As in the case of fluorescence, we distinguish between the Stokes (energy loss) and anti-Stokes (energy gain) components of Raman scattering. Since the probability of Stokes scattering is much higher for thermodynamic reasons, we observe it most often, while the observation of the anti-Stokes component requires special technical solutions, which will be discussed below. Since the energy shift in Raman scattering is associated with vibrational sublevels of molecules, this signal allows us to estimate the molecular composition of tissues without introducing additional markers.

Spectrally resolved imaging systems can be divided into multispectral and hyperspectral imaging (MSI and HSI). Familiar examples of spectrally resolved imaging in everyday life are human color vision and the color cameras of our smartphones. The three color channels allow these systems to be classified as multispectral systems. Multispectral images typically contain between 3 and 10 bands. If more filters with narrower bandwidths are used, such a system can be called hyperspectral. Thus, the main difference between multispectral and hyperspectral images is the number of bands and their width [1].

In fact, in spectrally resolved visualization, instead of a single image, we register a hypercube of size H×W×L (frame height and width, as well as wavelength), i.e. a set of images, each of which corresponds to the brightness distribution in a certain spectral range. In this case, each spatial pixel of such an image contains information about the spectral distribution at a given point in the field of view (Fig. 2).

The two main categories of spectral imaging methods are scan-based and wide-field imaging. Point scanning (whisk-broom) methods (Fig. 3A) capture spectral data pixel by pixel. Although this method provides high spectral resolution, it requires H×W iterations to obtain a hypercube, which is time-consuming for megapixel images and limits their use for capturing static scenes and/or small fields of view. Linear scanning (push-broom) methods (Fig. 3B) use a linear detector oriented perpendicular to the scanning direction (e.g., row detec-

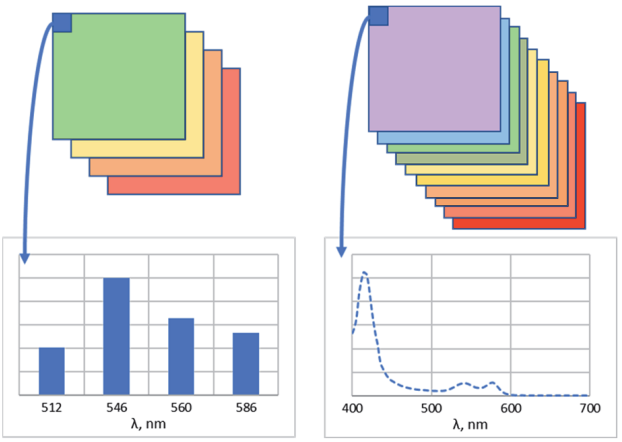

Рис. 2. Различие мультиспектральных и гиперспектральных изображений.
Fig. 2. Difference between multispectral and hyperspectral images.

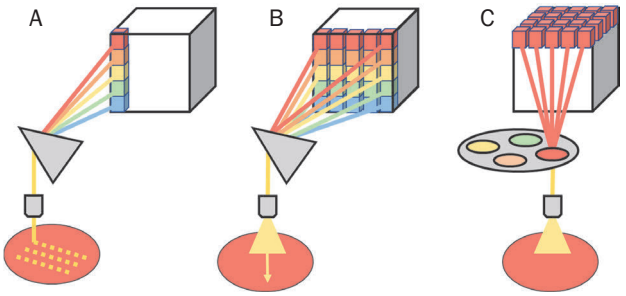

Рис. 3. Различные методы получения гиперспектральных данных (A – точечное сканирование, B – линейное сканирование, C – спектральное сканирование).
Fig. 3. Different methods of obtaining hyperspectral data (A – point scanning, B – line scanning, C – spectral scanning).

tors scan along columns), and spectral data are collected row by row. This approach reduces the number of registrations to the number of rows or columns in the image, which significantly decreases the registration time compared to point scanners. These are the most common systems that are widely used in HSI applications [2].

Wide-field imaging is a method of simultaneously illuminating and, consequently, detecting the entire field of view in an array of points (pixels of the detector array). Compared to scan-based imaging methods, wide-field imaging eliminates the need for mechanical scanning and allows a large area to be imaged in a single scan.

Spectral scanning methods (Fig. 3C) are essentially related to wide-field imaging as they allow one spectral channel in a hyperspectral cube to be imaged at a time. For this purpose, it is possible to use a tunable bandpass spectral filter for sequential acquisition of two-dimensional images in each spectral channel. It is possible to implement this principle through filters at the receiver, as well as time multiplexing of light sources, for example. Snapshot methods provide a hyperspectral cube with full spatial and spectral information in a single exposure. Snapshot acquisition is achieved by multiplexing the sensor with spatial separation in spatial and spectral dimensions. It can be several cameras separated by beam splitters, mosaically arranged filters on the detector matrix or separation of the detector matrix into macro zones for different filters.

Video fluorescent systems

At the end of the 20th century, W. Stummer [3] presented the results of the study of fluorescence of 5-ALA-induced protoporphyrin IX (Pp IX) in patients with glioblastoma, which initiated a new round of interest in fluorescence in surgical practice. Pp IX is not injected itself, but accumulates in tumor tissues as a product of the metabolism of 5-aminolevulinic acid, which is used as a drug for administration. This determines a number of its interesting properties as a tumor marker [4–6]. Another porphyrin-based fluorescent tumor marker chlorin e6 is promising for application in neuro-oncology [7]. Since then, the use of Pp IX and chlorin e6 has become widespread in neurosurgery [8, 9] and has gone beyond an exclusively spectroscopic technique – in many neurosurgical clinics and departments, fluorescence video navigation is a routine part of brain and spinal cord tumor removal [10].

Fluorescence is the emission of light by an atom or molecule in an electronically excited state (in particular, due to light absorption) (Fig. 4). Fluorescence is one variant of the radiative relaxation of a molecule from an excited state.

Video systems for fluorescence navigation in neurosurgery can currently be divided into wide field of view and microscopic systems.

The principle of working of systems with a wide field of view is to illuminate the entire area of interest with a light source, the wavelength of which coincides with one of the maxima in the absorption spectrum of the detected fluorescent markers. For example, protoporphyrin IX, which is widely used in neurosurgery, has a strong absorption band in the violet region, the so-called Soret band, as well as a Q-band of absorption closer to the window of biological transparency, therefore, light sources with wavelengths coinciding with all local absorption maxima of this molecule can be used for its excitation. For fluorescence detection a cross filter system is necessary: an illuminating filter suppressing the excitation light in the spectral range of fluorescence registration, and an imaging filter installed before the photodetector suppressing the excitation light, which is necessary because fluorescence is several orders of magnitude lower in intensity than the light that excites it.

Among the systems with a wide field of view, the Opmi Pentero Carl Zeiss microscope with Blue 400 mode, which allows to observe fluorescence of Pp IX when excited by violet light, is actively used in neurosurgical practice. The main limitation of using this mode is the presence of blood in the wound, which absorbs visible light in the short-wave region, preventing it from penetrating deeper – to the tissues under study. This limitation can be avoided by using an excitation source not in the short-wave range of the spectrum, in which most of the biological molecules absorb light, but, for example, in the first window of biological transparency in the red region, as it was proposed in [11]. The authors created an endoscopic system for visualizing the distribution of

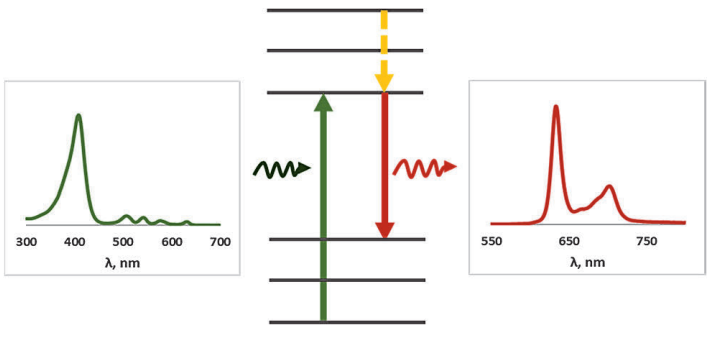

Рис. 4. Диаграмма Яблонского с энергетическими переходами, иллюстрирующими принцип поглощения света молекулой и испускания флуоресценции в стоксовой области.
Fig. 4. Jablonski diagram with energy transitions illustrating the principle of light absorption by a molecule and fluorescence emission in the Stokes region.

Pp IX that combines full-color and fluorescence imaging and calculates the concentration of the photosensitizer under study in the central region. A system combining a neurosurgical aspirator and the technique of fiber-optic spectroscopy and spectrally resolved endoscopy during surgeries for brain tumor removal was also based on this technical solution [12]. In this implementation, a fixed distance from the endoscope end face to the tissue allows calibrating the system by fluorescence level and quantifying the fluorophore concentration in the tissue by signal brightness. Research is also underway on the use of photo and spectral fluorescence analysis of the area of spinal cord injury [13] or tumors [14].

In [15], a spectrally resolved video fluorescence system integrated into a commercial neurosurgical microscope is presented that allows quantitative estimation of Pp IX content by correcting the effects of optical absorption and tissue scattering in the detected fluorescence signal.

Despite the fact that the best delineation of tumor tissues by fluorescent dye can be observed in high-grade tumors, a large amount of work is also devoted to fluorescence navigation in the removal of intracranial low-grade tumors [16].

Intraoperative microscopy (microscopic imaging with cellular and subcellular spatial resolution and millimeter field of view) is also used as a tool for intraoperative surgical navigation in brain tumor resection. Confocal microscopy or confocal laser endomicroscopy (CLE) [17] using portable probes provide *in vivo* registration of microstructural images, allowing intraoperative visualization of structures at depth, in three dimensions, with histological detail (depending on the fluorescent markers used). It is based on the principle of optical scanning by laser beam of the entire field of view and registration of fluorescent emission through small apertures (pinholes) placed in the path of light for selective display of photons from a certain focal plane.

The first results of using the Optiscan FIVE 1 fiber-optic confocal system (Optiscan Pty Ltd, Australia) for neurosurgery were published in [18] in 2010. This device contains a miniature fiber-optic probe, excitation and fluorescence radiation are transmitted through a single fiber. The system provides non-invasive image registration by optical sectioning at a known depth. The system has been validated in C57/BL6 laboratory animals with GL26 glioblastoma. Fluorescein (0.1% Pharmalab, Australia) and acriflavine (0.05% Sigma Chemicals, Australia) were used as fluorescent dyes. Another example of using the Optiscan system on animals with C6 glioma and fluorescein as a dye was published in [19]. In addition to fluorescein, the authors also used acriavin, indocyanine green and fluorescein isothiocyanate as dyes. Their results allowed morphological analysis and correlated well with classical histological images of the same tumor sections. Another work using the Optiscan intraoperative confocal microscopy system was performed by Martirosyan et al. on animals with C6 gliomas and indocyanine green as a fluorescent marker [20].

A study of the method of confocal laser endomicroscopy with fluorescein was conducted in clinical conditions on a sample of 33 patients with brain tumors [21]. A definite breakthrough in this direction was the study [22] conducted in clinical conditions on patients with benign glial tumors using Pp IX as a fluorescent marker; at the same time, due to the peculiarities of the drug accumulation in cells, it was not a question of morphological analysis, as it was demonstrated in the works with fluorescein. The differences between tumor and normal tissue were determined by the number of luminous cells in the field of view. However, even in this case, it is possible to detect some correlation between the intraoperative picture and the histologic picture obtained in the laboratory. The work [23] was also performed in clinical conditions using the same endomicroscope, but fluorescein administered intravenously immediately before the endomicroscope analysis procedure was used as a marker. The results obtained correlated well with data from classical pathomorphology. A distinctive feature of this work is the rather broad coverage of different types of intracranial tumors. Various artifacts of the intraoperative confocal system, particularly shear artifacts and blood shielding of the signal, are also discussed in this paper.

In [24], two contrast agents, fluorescein and 5-ALA induced protoporphyrin IX with excitation in the blue range of the spectrum, were used for confocal laser endomicroscopy (Cellvisio system, Maune Kea Technologies, Paris, France). This device uses a fiber optic bundle as a sensor, in which each fiber functions as a pinhole. One disadvantage of this device is the inability to adjust the depth of focus, and another is the autofluorescence of the fiber material when excited at 405 nm, making it difficult to use for excitation of 5-ALA Pp IX in the Soret band [25]. The study was performed on a sample of 9 patients, of which 6 had open surgery and 3 had stereotactic biopsy.

Summarizing the features of confocal laser endomicroscopy systems, it can be seen that structural analysis close to classical pathomorphology is achieved using fluorescein. In this case, fluorescein is predominantly an extracellular contrast agent, penetrating only through the disrupted blood-brain barrier. When malignant gliomas are observed, it provides an intense fluorescent background. Cells and intracellular structures are identified as transparent or darker structures on the fluorescent background. Erythrocytes are visualized against the background in the same way. If the distal end of the probe is not cleaned, artifacts from blood can reduce image quality and affect the analysis. These

disadvantages suggest the advantages of using dyes that are excitable and fluorescent in the red and near-infrared, such as Pp IX and indocyanine green. Pp IX is a more tumor-specific dye.

The main obstacle to the widespread use of laser confocal scanning microscopy in intraoperative analysis is the scanning principle itself. Sufficiently long scanning time (on average about 1 second for 1 frame for different systems) leads to the appearance of shear artifacts and to a decrease in the decoding properties of the obtained images. A system combining a spectrally resolved quantitative imaging device with a wide field of view and a fluorescence endomicroscope is described in [26]. Spectral resolution is achieved by using a tunable liquid crystal filter with a half-width of 20 nm in the range of 400–720 nm. The system already mentioned above, Cellvizio (Mauna Kea Technologies), is used as a fluorescence endomicroscope. In [27], it was shown that over a wide range of fluorophore concentrations, the ability of a video system using red light to excite fluorescence at different depths along the image axis up to 6 mm below the surface allows resolution of multiple fluorescent foci at a distance of 2 mm in the same plane or at different depths along the image axis at a distance of 3 mm. Second-generation CLE systems, such as the ZEISS CONVIVO (Carl Zeiss Meditec AG, Oberkochen, Germany), have been specifically designed for neurosurgical use and have undergone a number of clinical trials in recent years. CONVIVO has been used in animal models and in *ex vivo* and *in vivo* experiments, confirming its feasibility with fluorescein as a technology capable of providing real-time *in vivo* histopathologic data [28–31].

Hyperspectral imaging in diffuse-reflected light

Biological tissues are mostly strongly scattering media, i.e. light falling on them is multiply scattered by fluctuations of the refractive index in the medium. Part of the light returns to the detector, forming the so-called diffuse reflectance (DR) signal (Rd on Fig. 1). Since light is not only scattered in tissues, but part of it is also absorbed by tissue chromophores, the detected spectrum carries information about both scattering and absorbing properties of tissues. The main chromophore in the visible part of the spectrum is hemoglobin. Due to differences in the absorption spectrum of hemoglobin in oxygenated and reduced forms, it is also possible to estimate the local level of hemoglobin oxygen saturation using DR spectra.

The work [32] is devoted to the analysis of fresh *ex vivo* glioma samples using both a laboratory spectrophotometer and a hyperspectral system, which is based on spectral scanning of samples using illumination by a supercontinuum laser (SCL) filtered by acousto-optic tunable filters (AOTF). When comparing spectrophotometry and hyperspectral imaging data, significant differences were found between individual regions in two spectral ranges: between 510 and 660 nm (which can be attributed to variations in hemoglobin concentration and oxygenation) and between 780 and 880 nm (which can be either hemoglobin or cytochrome c oxidase).

The HELICoiD system is presented in [33, 34]. It consists of two hyperspectral cameras. The first one operates in the visible and near-infrared spectral range (400–1000 nm), and the second one operates in the near-infrared range (900–1700 nm). These cameras are connected to a scanning device with a push rod. The illumination system provides cold light from 400 to 2200 nm through an optical fiber connected to a quartz tungsten-halogen lamp. The hyperspectral system is based on the line-scanning method and provides a spectral resolution of 2–3 nm, allowing identification of tumor tissue and vascular structures. In [35], the authors performed a statistical analysis of hyperspectral images of brain tumor patients from the HELICoiD dataset to identify correlations between reflectance and absorption spectra of tissue chromophores, also finding a correlation with cytochrome. The authors of [36] showed that the spectral bands 440.5–465.96 nm, 498.71–509.62 nm, 556.91–575.1 nm, 593.29–615.12 nm, 636.94–666.05 nm, 698.79–731.53 nm, and 884.32–902.51 nm are the most relevant for classification of brain tumor tissues based on hyperspectral images.

Raman scattering-based visualization

One of the most actively developing areas of spectral analysis in neuro-oncology at present is Raman spectroscopy [37–39]. As mentioned above, Raman scattering not only changes the direction of the incident radiation, but the probability of this process is lower than in the case of elastic scattering, and both an increase in energy (anti-Stokes component) and a decrease (Stokes component) are possible (Fig. 5).

Raman spectroscopy has many applications in medicine due to its ability to characterize individual molecules and biological tissues. Characteristic shifts in the Raman spectrum correspond to specific vibrational modes of chemical bonds. For example, the symmetric stretching mode of -CH_2 plays an important role in the characterization of biomedical samples, allowing the detection of fatty acids [40].

Three characteristic spectral bands in the Raman spectrum were used in [41] to create a virtual RGB color scheme. Red (1004 cm^{-1} channel corresponding to phenylalanine), green (1300–1344 cm^{-1}, CH deformations in protein and collagen) and blue (1600 cm^{-1}, C=O and C=C of the 1st amide band, lipids and nucleic acids) color scales encoded the intensities in the corresponding Raman spectral bands. On such color maps it was possible to distinguish white matter, gray matter, and tumor tissue with a diagnostic accuracy of about 90%.

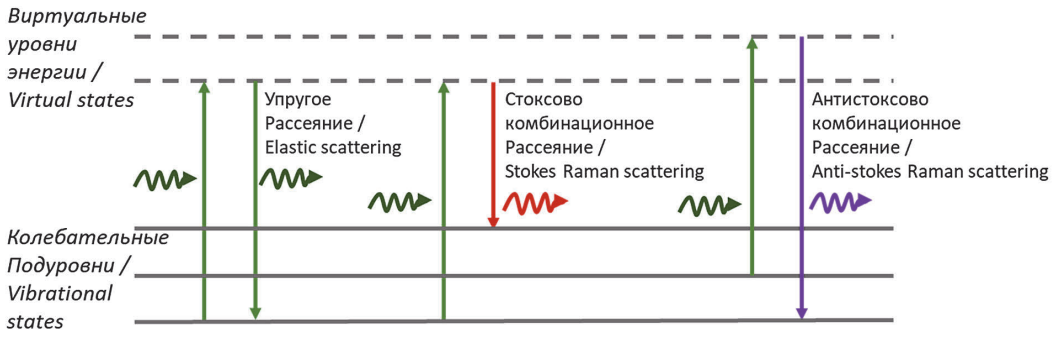

Рис. 5. Диаграммы Яблонского, иллюстрирующие эффект комбинационного рассеяния и его отличие от упругого рассеяния.
Fig. 5. Yablonsky diagrams illustrating the effect of Raman scattering and its difference from elastic scattering.

Spontaneous Raman scattering is the most accessible method in terms of cost, but due to the low cross section of the process the signal is too weak and exposure times on the order of several minutes are required. A number of approaches improve the sensitivity of the process. Instead of obtaining broadband Raman spectra in the range (0–3500 cm^{-1}), coherent Raman microscopy methods increase the signal intensity by targeting a specific wave number using a second excitation laser beam to coherently control the vibrational frequency of the active chemical Raman bonds. The two main techniques using this approach and applied to brain tumor imaging are stimulated Raman histology (SRH) and coherent anti-Stokes Raman scattering (CARS) microscopy.

A series of works [42, 43] presents the results of the application of a spectrally-resolved Raman based visualization technique for the analysis of images structurally similar to histological hematoxylin-eosin (H&E) images, but obtained using stimulated Raman scattering with a dual-wavelength fiber laser with a fixed pump wavelength of 790 nm and Stokes wavelengths in the range from 1015 nm to 1050 nm. For Stimulated Raman Histology (SRH) study, samples were sequentially scanned at two Raman shifts: 2850 cm^{-1} and 2950 cm^{-1}. Lipid-rich brain regions (e.g., myelinated white matter) show high signal at 2845 cm^{-1} due to symmetric CH_2 stretching in fatty acids. Cellular regions show high intensity at 2930 cm^{-1} and high S_{2930}/S_{2845} ratio, indicating high protein and DNA content. The resulting maps of the intensity ratios at these two peaks were converted to pseudocolor using the H&E coloring scheme. Convolutional neural networks (CNN) were used to classify the resulting images. This is a very promising method to use the entire array of currently accumulated H&E histologic slices as a training sample.

In work [44], CARS microscopy was used to visualize fresh unfixed and unstained *ex vivo* specimens from a mouse model of orthotopic human astrocytoma. The histologic features shown on CARS images were comparable to standard H&E histology. Chemically selective images of lipids (2845 cm^{-1}, symmetric CH_2 stretching) and proteins (CH_3 stretching, 2920 cm^{-1}; amide I band, 2960 cm^{-1}) allowed the delineation of the brain tumor boundary in a mouse model. The authors [45] used molecular C-H vibrations in different cryosectioned brain tumors (glioblastoma, melanoma, and breast cancer metastases) to assess lipid content compared to normal brain tissue, demonstrating that all tumor types have lower CARS lipid signal intensity than normal parenchyma.

Methodology for the application of machine learning in analyzing spectrally resolved images

Machine learning (ML) methods are used for spectrally resolved images at several levels. First, for image processing and segmentation, and second, for data classification. The combination of these methods is usually combined by the term machine vision. However, in the case of spectrally resolved images, we have a hypercube of data, i.e. the dimensionality we operate on is higher than when analyzing conventional images. At the same time, the sampling volume, as is often the case in medical applications, is limited by the image registration procedure itself.

Typically, to develop effective clinical decisions, AI models are trained to reproduce expert performance on large amounts of well-annotated data, leading to reasonably accurate and reproducible results in medical image analysis. However, this approach is critically dependent on the availability of large annotated datasets. Strict regulatory restrictions on medical data sharing and the opportunity cost for physicians to annotate data make the generation of large datasets far from a trivial task [46] Several approaches have been used to increase the amount of available data, such as synthetic dataset generation [47] or artificial expansion of available annotated datasets [48]. More non-trivial approaches are also possible, as in the case of histology based on Raman spectroscopy, where two characteristic peaks for proteins and lipids allow the generation of a pseudo-color image that mimics histological tissue images when stained with hematoxylin-eosin, which immediately opens access to huge databases of pathomorphological data [49]. The method of laser confocal endomicroscopy with

fluorescein offers a similar expansion of the annotated data base.

The stage of preprocessing of recorded signals is critical for successful tissue classification using spectrally resolved data, including images. In works devoted to hyperspectral imaging systems, a general algorithm can be identified, including such stages as formation of the hypercube of data (regardless of the type of scanning used), background correction, correction on the white and dark reference images, spectral correction, normalization, and often a synthetic full-color image. When analyzing spectrally resolved images based on the Raman effect, the algorithm includes removal of "silent" regions in the spectrum (those that do not contain characteristic peaks), cosmic rays removal, baseline and fluorescence correction, normalization.

Hyperspectral imaging has shown remarkable results as a diagnostic tool for tumor detection in various medical applications. In [50], using a k-fold cross-validation approach, they demonstrated that HSI combined with the proposed processing system (Table 1) is a promising intraoperative tool for in-vivo identification and delineation of brain tumors, including both primary (high and low malignancy) and secondary tumors. The obtained data were transformed into a set of spectral and spatial features with subsequent classification using both classical machine learning and deep learning methods [51].

An important stage of work with spectral data is the choice of a dimensionality reduction method. Among the most commonly used methods are feature filtering methods based either on a priori data on biochemical composition of tissues or on the results of statistical analysis and selection of those features that provide statistically significant differences between classes of data. Another widely used approach is the use of feature projection methods, among which the principal component analysis (PCA) is the most popular. PCA is used to project a higher-dimensional data matrix onto a low-component subspace. It reduces the set of variables to a smaller set of orthogonal, and thus independent, principal components in the direction of maximum variation, i.e., it reduces the dimensionality and preserves the most significant information for further analysis. Linear discriminant analysis (LDA) and, somewhat less frequently, quadratic discriminant analysis (QDA) are also frequently used for this purpose. The main goal of linear discriminant analysis (also called Fisher's linear discriminant) is to find "axes of discrimination" that optimally classify data into two or more classes. LDA is closely related to PCA (Principal Component Analysis) in that both look for latent axes that compactly explain the variance in the data. The main difference between PCA and LDA is that LDA is a supervised method and PCA is an unsupervised method. PCA looks for predictions that maximize the variance, and LDA looks for predictions that maximize the ratio of interclass variance to intraclass variance. QDA is a classifier with a quadratic decision boundary, generated by fitting class conditional densities to the data and using Bayes' rule.

Another way to reduce the dimensionality of the data is the t-Distributed Stochastic Neighbor embedding (t-SNE) algorithm. It is a nonlinear dimensionality reduction method well suited for embedding high-dimensional data for visualization into a low-dimensional space of two or three dimensions. In the higher dimension space, a probability distribution over pairs of points is constructed in such a way that similar points are assigned a high probability, and dissimilar points are assigned a lower probability. And in the lower dimension space, the algorithm tries to achieve similar probability distribution by minimizing Kullback–Leibler divergence between two distributions. t-SNE tries to preserve the relative positions of points in lower dimensional mapping.

To deal with high-dimensional hyperspectral data, a dimensionality reduction method with manifold embedding can also be used. This method uses a modified version of t-SNE based on deep learning, called t-SNE with fixed references (FR-t-SNE). This nonlinear embedding method seeks to preserve local spatial regularity (nearby pixels have a high probability of representing the same class) while preserving high-level global features (pixel classes) [52].

Both classical machine learning methods such as support vector machine (SVM) method, linear and quadratic discriminant analysis, ensembles of random forest (RF) based algorithms, and methods based on neural networks are used to classify tissues according to the

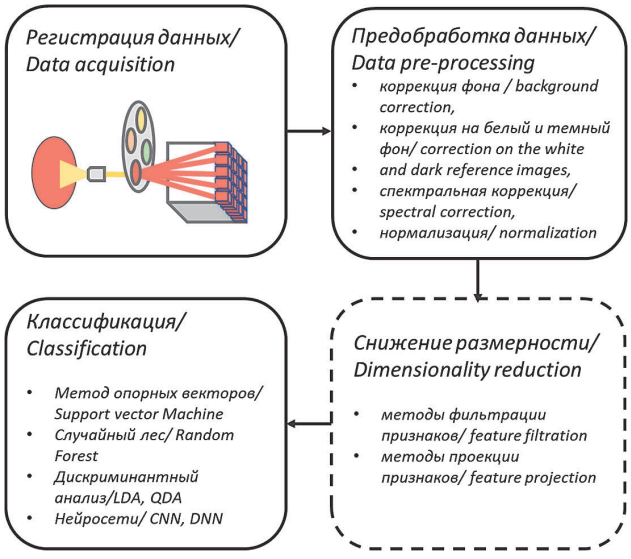

Рис. 6. Блок-схема основных этапов анализа спектрально-разрешенных изображений.
Fig. 6. Flowchart of the key steps involved in the analysis of spectrally-resolved images.

obtained features (Table 1). SVM method is a supervised machine learning algorithm that predicts an optimal hyperplane in n-dimensional space to divide the training set into several classes. Depending on the problem, different kernel functions can be defined for the decision function to add another dimensionality to the data, allowing better partitioning into classes. The algorithm proposed in the study [53] used a hybrid approach that combined both supervised and unsupervised machine learning methods. First, supervised pixel classification using SVM was performed. The generated classification map was spatially homogenized using the t-SNE dimensionality reduction algorithm and K-nearest neighbor (KNN) filtering. The information obtained from the supervised stage was merged with the segmentation map obtained by clustering. The merging was performed using a majority voting approach that associates each cluster with a particular class.

A combined approach was also used in [54]. The KNN-based filtering algorithm receives an input image that consists of probability maps estimated by the SVM classifier and a hypercube representation at one of the wavelengths generated using a dimensionality reduction algorithm such as PCA. The result is a classification map where each pixel is assigned to the most likely class. The nearest neighbors of a particular pixel are searched in the feature space, which contains both the pixel value and spatial coordinates.

Таблица 1.
Методология, используемая при классификации спектрально-разрешенных изображений, регистрируемых в условиях *in vivo*

Table 1.
Methodology used in the classification of spectrally resolved images recorded *in vivo*

Источник Source	Тип сигнала Signal type	Снижение размерности Dimensionality reduction	Методы МО ML methods
Ayaz 2022 [57]	ГСВ (ЛС) HSI (push-broom)	Автокорреляции и инкрементальный МГК The autocorrelation and incremental PCA	3D CNN
Baig 2021 [58]	ГСВ (ЛС) HSI (push-broom)	Эмпирическая модовая декомпозиция, выбор признаков EMD (Empirical Mode Decomposition), feature selection	SVM
Cruz-Guerrero, 2020 [59]	ГСВ (ЛС) HSI (push-broom)	Расширенное слепое извлечение конечных элементов и распространенности Extended blind end-member and abundance extraction (EBEAE)	Слепое линейное разложение Blind linear unmixing, SVM
Ezhov, 2023 [35]	ГСВ (ЛС) HSI (push-broom)	МГК PCA	
Fabelo, 2016 [33]	ГСВ (ЛС) HSI (push-broom)		SVM, CNN, RF
Fabelo, 2018 [53]	ГСВ (ЛС) HSI (push-broom)	t-SNE	SVM, KNN
Fabelo, 2019 [51]	ГСВ (ЛС) HSI (push-broom)	Эмпирический выбор трёх спектральных каналов Empirical choice of three spectral channels	2D-CNN, DNN
Florimbi, 2018 [54]	ГСВ (ЛС) HSI (push-broom)	PCA	SVM, KNN
Leon, 2023 [50]	ГСВ HSI	PCA	SVM, RF, KNN, DNN
Ravi, 2017 [52]	ГСВ (снимок) HSI (Snapshot)	Вложение многообразий Manifold embedding	STF
Ruiz, 2020 [60]	ГСВ (снимок) HSI (Snapshot)		SVM, RF
Salvador, 2016 [61]	ГСВ (ЛС) HSI (push-broom)		SVM, RF, CNN, KKN
Sutradhar, 2022 [62]	ГСВ (снимок) HSI (Snapshot)		SVM
Torti, 2018 [63]	ГСВ (ЛС) HSI (push-broom)	PCA	SVM, KNN
Urbanos, 2021 [64]	ГСВ (снимок) HSI (Snapshot)		SVM, RF и CNN

*ГСВ – гиперспектральная визуализация, ЛС – линейное сканирование, МГК – метод главных компонент, ЛДА – линейный дискриминантный анализ, КДА – квадратичный дискриминантный анализ, SVM – метод опорных векторов, RF – случайный лес, KNN – метод k ближайших соседей, CNN – конволюционная нейросеть, DNN – глубокая нейросеть, STF – семантический текстовый лес
*HSI – Hyperspectral Imaging, PCA – Principal Component Analysis, LDA – linear discrimimnant analysis, QDA – Quadratic Discriminant Analysis, SVM – Support Vector Machine, RF – Random Forest, KNN – k Nearest Neighbors, CNN – Convolutional Neural Network, DNN – Deep Neural Network, STF – Semantic Texton Forest

A random forest (RF) is an ensemble-based machine learning algorithm with a teacher that uses decision trees as a base. For classification tasks, the output of a random forest is the class selected by the majority of trees. For regression tasks, the output is the average of the predictions of the trees. Studies on the use of RF [55, 56] have proved that it is a successful classifier when hyperspectral images are used.

Convolutional neural networks (CNNs) have an advantage over classical machine learning methods in that they actually implement both stages: feature extraction and classification. In the feature extraction block, convolutions are performed to detect patterns in spatial and spectral dimensions, resulting in a 3D convolutional neural network (3D CNN) [57]. This feature extraction stage yields a reduced feature vector as output, which serves as input for the classification stage, where a number of fully connected layers display a feature to partition the data into desired classes. The parameters of convolutional and fully connected layers are trained in a supervised manner. Deep learning can be applied to tumor identification in both deep fully-connected pixel-by-pixel and convolutional spatial-spectral configurations [65]. The 3D CNN model proposed in [57] consists of only two 3D layers and utilizes a limited number of training samples (20%), which are further divided into 50% for training and 50% for validation, and tested blindly (80%) on the remaining data. This study outperformed the state-of-the-art hybrid architecture, achieving an overall accuracy of 99.99%. In [51], both a classifier based on a two-dimensional convolutional neural network (2D-CNN) of three convolutional layers, one averaging pooling layer and one fully connected layer, and a deep neural network (DNN) (implemented in TensorFlow on NVIDIA Quadro K2200 GPU and trained using only spectral features of the samples) were used. Three spectral channels (λ42=591.10 nm, λ50=620.21 nm, and λ80=729.34 nm) were selected from the hypercube to highlight blood vessels in the image, the resulting images were classified using 2D-CNN. The map of parenchymatous regions was also obtained using 2D-CNN. The hypercube was fed to the 1D-DNN input, classifying the tissues in the image into four classes: normal

Таблица 2.
Методология, используемая при классификации спектрально-разрешенных изображений, регистрируемых в условиях *ex vivo*

Table 2.
Methodology used in the classification of spectrally resolved images recorded *ex vivo*

Источник Source	Подготовка материала Sample Preparation	Тип сигнала Signal type	Снижение размерности Dimensionality reduction	Методы МО ML methods
Fürtjes 2023 [66]	*ex vivo*	SRH, двухфотонная флуоресценция SRH, two-photon fluorescence		CNN
Hollon, 2021 [43]	*ex vivo*	SRH	Inception-ResNet-v2	DNN
Hollon, 2023 [42]	*ex vivo*	Stimulated Raman histology (SRH)	ResNet-50	DNN
Kast, 2015 [41]	*ex vivo*	Raman microscopy (785 nm)	(1004 $см^{-1}$), (1300–1344 $см^{-1}$), (1600 $см^{-1}$)	Многочленная логистическая модель A multinomial logistic model
Lita, 2024 [70]	FFPE	Raman microscopy (532 nm)	МГК, tSNE PCA, tSNE	KNN, DBSCAN, SVM, RF
Morais, 2019 [71]	FFPE	Raman microspectroscopy imaging (785 nm)	МГК, АПП, ГА PCA, SPA, GA	LDA, QDA, SVM
Orringer, 2017 [49]	Замороженные срезы Frozen sections	Stimulated Raman scattering (SRS) microscopy		Многослойный персептрон (MLP) Multilayer perceptron (MLP)
Uckermann, 2020 [69]	Замороженные срезы, свежий биопсийный материал Cryosections, *ex vivo* fresh biopsies	CARS, TPEF		LDA

*FFPE – фиксированные формалином и залитые парафином препараты тканей, SRH – гистология на основе вынужденного комбинационного рассеяния, МГК – метод главных компонент, АПП – алгоритм последовательных проекций, ГА – генетический алгоритм, CNN – конволюционная нейросеть, DNN – глубокая нейросеть.
*FFPE – Formalin-fixed, paraffin-embedded tissue slides, SRH – Stimulated Raman histology, PCA – Principal Component Analysis, SPA – Successive projections algorithm, CNN – convolutional neural network, DNN – deep neural network.

tissue, tumor tissue, blood vessels/hypervascularized tissue, and background. The blood vessel map was then merged with the 1D-DNN classification map by filling in the positive mask, and this result was merged with the parenchyma map using negative mask filling.

Very promising results can be obtained by combining different approaches. Moving from the works devoted to spectrally resolved imaging *in vivo* to *ex vivo* approaches, it is necessary to consider several used optical-spectral modalities at once. In [66], brain autofluorescence and neoplasia were evaluated at the microscopic level using stimulated Raman histology (SRH) combined with two-photon fluorescence. By combining two different optical effects, Raman scattering and autofluorescence with two-photon excitation, virtual images similar in structure to classical histological images obtained by hematoxylin-eosin staining with corresponding fluorescence images were obtained. Based on a previously developed convolutional neural network (CNN) based model [67], tumor, non-tumor and low quality SRH images were differentiated, and a heat map was created as an overlay on the SRH image. Using the CNN heat map, regions of interest (ROIs) were created and overlaid on the corresponding autofluorescence image to determine the average fluorescence intensity in the corresponding ROI. Another important technique for visualizing biological tissues is microscopy based on the principle of multiphoton fluorescence. The main advantage of this method of molecular imaging is high spatial resolution in combination with greater depth of penetration into the tissue, and this method shows good results even without the introduction of additional dyes, based on autofluorescence analysis [68]. Interesting results were obtained by the authors [69] using a combination of techniques such as CARS, two-photon-excited fluorescence (TPEF) and second harmonic generation on brain tumor cryosections of 382 patients and 28 healthy brain tissue samples. The texture parameters of these images were calculated and used as input for linear discriminant analysis. The combined analysis of CARS and TPEF signal texture parameters proved to be the most suitable for distinguishing between non-tumor brain tissues and brain tumors (astrocytomas of low and high malignancy, oligodendroglioma, glioblastoma, recurrent glioblastoma, and metastases) with a sensitivity of 96%, specificity of 100%. To approximate the clinical results, the results were validated on 42 fresh unfixed tumor biopsies: 82% of tumors and all non-tumor specimens were correctly identified. An image resolution of 1 μm was sufficient to distinguish between brain tumors and non-tumor brain.

The use of forced Raman microscopy with the construction of a distribution map of the ratio of protein and lipid peaks makes it possible to construct a pseudo-hematoxylin-eosin image, i.e., to use the entire accumulated histological material to classify the corresponding samples, which was brilliantly demonstrated in [42, 43].

Conclusion

Optical spectroscopy methods, due to the possibility of non-damaging interaction of light with biological tissues and wide possibilities of analyzing the content of various molecules, markers, and their structural features, are increasingly used in neurosurgery of intracranial tumors to solve the problems of intraoperative demarcation of tumor and healthy tissues. Another trend is the use of optical-spectral methods as urgent biopsy techniques. Clinical specialists are already accustomed to working with medical images, which causes their growing interest in the expansion of optical-spectral methods into the field of analyzing spectrally resolved images. However, the interpretation of such images requires a complex mathematical apparatus including both methods of preprocessing of data obtained in spatial and spectral coordinates, and methods of classification of objects and tissues in these images in order to determine the boundaries of tumor tissues during surgery, or their classification during microscopic examination. This review considers such spectrally resolved image registration methods as video fluorescence intraoperative navigation including endomicroscopy, hyperspectral intraoperative imaging in diffuse-reflected light, Raman microscopy methods. Basic machine learning methods used for tissue classification in neuro-oncology based on the analysis of such images are also presented.

This work was financially supported by the Ministry of Science and Higher Education of the Russian Federation (Agreement No. 075-15-2021-1343 dated October 4, 2021).

REFERENCES

1. Aboras M., Amasha H., Ibraheem I. Early detection of melanoma using multispectral imaging and artificial intelligence techniques, *American Journal of Biomedical and Life Sciences*, 2015, vol. 3(2–3), pp. 29–33. doi: 10.11648/j.ajbls.s.2015030203.16.
2. Kotwal A., Saragadam V., Bernstock J. D. et al. Hyperspectral imaging in neurosurgery: a review of systems, computational methods, and clinical applications, *Journal of Biomedical Optics*, 2024, vol. 30(02) doi: 10.1117/1.JBO.30.2.023512.

ЛИТЕРАТУРА

1. Aboras M., Amasha H., Ibraheem I. Early detection of melanoma using multispectral imaging and artificial intelligence techniques // American Journal of Biomedical and Life Sciences. – 2015. – Vol. 3. – № 2–3. – P. 29–33.doi: 10.11648/j.ajbls.s.2015030203.16.
2. Kotwal A., Saragadam V., Bernstock J. D. et al. Hyperspectral imaging in neurosurgery: a review of systems, computational methods, and clinical applications // Journal of Biomedical Optics. – 2024. – Vol. 30. – № 02.doi: 10.1117/1.JBO.30.2.023512.

3. Stummer W., Stocker S., Wagner S. et al. Intraoperative Detection of Malignant Gliomas by 5-Aminolevulinic Acid-induced Porphyrin Fluorescence, *Neurosurgery*, 1998, vol. 42(3), pp. 518–526. doi: 10.1097/00006123-199803000-00017.
4. Traylor J. I., Pernik M. N., Sternisha A. C. et al. Molecular and Metabolic Mechanisms Underlying Selective 5-Aminolevulinic Acid-Induced Fluorescence in Gliomas, *Cancers*, 2021, vol. 13(3), pp. 580. doi: 10.3390/cancers13030580.
5. Ivanova-Radkevich V. I., Kuznetsova O. M., Filonenko E. V. The role of membrane transport proteins in 5-ALA-induced accumulation of protoporphyrin iX in tumor cells, *Biomedical Photonics*, 2024, vol. 13(2), pp. 43–48. doi: 10.24931/2413-9432-2024-13-2-43-48.
6. Nasir-Moin M., Wadiura L. I., Sacalean V. et al. Localization of protoporphyrin IX during glioma-resection surgery via paired stimulated Raman histology and fluorescence microscopy, *Nature Biomedical Engineering*, 2024, vol. 8(6), pp. 672–688. doi: 10.1038/s41551-024-01217-3.
7. Matsumura H., Akimoto J., Haraoka J. et al. Uptake and retention of the photosensitizer mono-l-asparthyl chlorine e6 in experimental malignant glioma, *Lasers in Medical Science*, 2008, vol. 23(3), pp. 237–245. doi: 10.1007/s10103-007-0469-3.
8. Valdés P. A., Jacobs V., Harris B. T. et al. Quantitative fluorescence using 5-aminolevulinic acid-induced protoporphyrin IX biomarker as a surgical adjunct in low-grade glioma surgery, *Journal of Neurosurgery*, 2015, vol. 123(3), pp. 771–780. doi: 10.3171/2014.12.JNS14391.
9. Rynda A. Yu., Olyushin V. E., Rostovtsev D. M. et al. Results of microsurgical resection of glioblastomas under endoscopic and fluorescent control, *Biomedical Photonics*, 2024, vol. 13(3), pp. 20–30. doi: 10.24931/2413-9432-2024-13-3-20-30.
10. Goryajnov S. A., Potapov A. A., Loschenov V. B. et al. Fluorescence in neurosurgery / S. A. Goryajnov, A. A. Potapov, V. B. Loschenov et al., ed. D.Yu. Usachev, Moscow: TPS Print, 2024. (in Russ.)
11. Loshchenov M., Zelenkov P., Potapov A. et al. Endoscopic fluorescence visualization of 5-ALA photosensitized central nervous system tumors in the neural tissue transparency spectral range, *Photonics & Lasers in Medicine*, 2014, vol. 3(2) doi: 10.1515/plm-2013-0017.
12. Savelieva T. A., Loshchenov M. V., Borodkin A. V. et al. Combined spectroscopic and video fluorescent instrument for intraoperative navigation when removing a glial tumor ed. Z. Zalevsky, V. V. Tuchin, W. C. Blondel, Online Only, France: SPIE, 2020.p. 35. doi: 10.1117/12.2556064.
13. Udeneev A. M., Kalyagina N. A., Reps V. F. et al. Photo and spectral fluorescence analysis of the spinal cord injury area in animal models, *Biomedical Photonics*, 2023, vol. 12(3), pp. 15–20. doi: 10.24931/2413-9432-2023-12-3-16-20.
14. Wainwright J. V., Endo T., Cooper J. B. et al. The role of 5-aminolevulinic acid in spinal tumor surgery: a review, *Journal of Neuro-Oncology*, 2019, vol. 141(3), pp. 575–584. doi: 10.1007/s11060-018-03080-0.
15. Valdés P. A., Jacobs V. L., Leblond F. et al. Quantitative spectrally resolved intraoperative fluorescence imaging for neurosurgical guidance in brain tumor surgery: pre-clinical and clinical results ed. H. Hirschberg, S. J. Madsen, E. D. Jansen et al., San Francisco, California, United States:, 2014.p. 892809. doi: 10.1117/12.2039090.
16. Picart T., Gautheron A., Caredda C. et al. Fluorescence-Guided Surgical Techniques in Adult Diffuse Low-Grade Gliomas: State-of-the-Art and Emerging Techniques: A Systematic Review, *Cancers*, 2024, vol. 16(15), pp. 2698. doi: 10.3390/cancers16152698.
17. Maragkou T., Quint K., Pollo B. et al. Intraoperative confocal laser endomicroscopy for brain tumors - potential and challenges from a neuropathological perspective, *Free Neuropathology*, 2022, pp. 24 Pages. doi: 10.17879/FREENEUROPATHOLOGY-2022-4369.
18. Sankar T., Delaney P. M., Ryan R. W. et al. Miniaturized Handheld Confocal Microscopy for Neurosurgery: Results in an Experimental Glioblastoma Model, *Neurosurgery*, 2010, vol. 66(2), pp. 410–418. doi: 10.1227/01.NEU.0000365772.66324.6F.
19. Foersch S., Heimann A., Ayyad A. et al. Confocal Laser Endomicroscopy for Diagnosis and Histomorphologic Imaging of Brain Tumors *In Vivo*, *PLoS ONE*, 2012, vol. 7(7), pp. e41760. doi: 10.1371/journal.pone.0041760.

3. Stummer W., Stocker S., Wagner S. et al. Intraoperative Detection of Malignant Gliomas by 5-Aminolevulinic Acid-induced Porphyrin Fluorescence // Neurosurgery. – 1998. – Vol. 42. – № 3. – P. 518–526.doi: 10.1097/00006123-199803000-00017.
4. Traylor J. I., Pernik M. N., Sternisha A. C. et al. Molecular and Metabolic Mechanisms Underlying Selective 5-Aminolevulinic Acid-Induced Fluorescence in Gliomas // Cancers. – 2021. – Vol. 13. – № 3. – P. 580.doi: 10.3390/cancers13030580.
5. Ivanova-Radkevich V. I., Kuznetsova O. M., Filonenko E. V. The role of membrane transport proteins in 5-ALA-induced accumulation of protoporphyrin iX in tumor cells // Biomedical Photonics. – 2024. – Vol. 13. – № 2. – P. 43–48.doi: 10.24931/2413-9432-2024-13-2-43-48.
6. Nasir-Moin M., Wadiura L. I., Sacalean V. et al. Localization of protoporphyrin IX during glioma-resection surgery via paired stimulated Raman histology and fluorescence microscopy // Nature Biomedical Engineering. – 2024. – Vol. 8. – № 6. – P. 672–688.doi: 10.1038/s41551-024-01217-3.
7. Matsumura H., Akimoto J., Haraoka J. et al. Uptake and retention of the photosensitizer mono-l-asparthyl chlorine e6 in experimental malignant glioma // Lasers in Medical Science. – 2008. – Vol. 23. – № 3. – P. 237–245.doi: 10.1007/s10103-007-0469-3.
8. Valdés P. A., Jacobs V., Harris B. T. et al. Quantitative fluorescence using 5-aminolevulinic acid-induced protoporphyrin IX biomarker as a surgical adjunct in low-grade glioma surgery // Journal of Neurosurgery. – 2015. – Vol. 123. – № 3. – P. 771–780.doi: 10.3171/2014.12.JNS14391.
9. Rynda A. Yu., Olyushin V. E., Rostovtsev D. M. et al. Results of microsurgical resection of glioblastomas under endoscopic and fluorescent control // Biomedical Photonics. – 2024. – Vol. 13. – № 3. – P. 20–30.doi: 10.24931/2413-9432-2024-13-3-20-30.
10. Горяйнов С. А., Потапов А. А., Лощенов В. Б. и др. Флуоресценция в нейрохирургии / С. А. Горяйнов, А. А. Потапов, В. Б. Лощенов и др., под ред. Д. Ю. Усачева, Москва: ТПС Принт, 2024.
11. Loshchenov M., Zelenkov P., Potapov A. et al. Endoscopic fluorescence visualization of 5-ALA photosensitized central nervous system tumors in the neural tissue transparency spectral range // Photonics & Lasers in Medicine. – 2014. – Vol. 3. – № 2.doi: 10.1515/plm-2013-0017.
12. Savelieva T. A., Loshchenov M. V., Borodkin A. V. et al. Combined spectroscopic and video fluorescent instrument for intraoperative navigation when removing a glial tumor ed. Z. Zalevsky, V. V. Tuchin, W. C. Blondel, Online Only, France: SPIE, 2020. C. 35.doi: 10.1117/12.2556064.
13. Udeneev A. M., Kalyagina N. A., Reps V. F. et al. Photo and spectral fluorescence analysis of the spinal cord injury area in animal models // Biomedical Photonics. – 2023. – Vol. 12. – № 3. – P. 15–20. doi: 10.24931/2413-9432-2023-12-3-16-20.
14. Wainwright J. V., Endo T., Cooper J. B. et al. The role of 5-aminolevulinic acid in spinal tumor surgery: a review // Journal of Neuro-Oncology. – 2019. – Vol. 141. – № 3. – P. 575–584.doi: 10.1007/s11060-018-03080-0.
15. Valdés P. A., Jacobs V. L., Leblond F. et al. Quantitative spectrally resolved intraoperative fluorescence imaging for neurosurgical guidance in brain tumor surgery: pre-clinical and clinical results ed. H. Hirschberg, S. J. Madsen, E. D. Jansen et al., San Francisco, California, United States, 2014. C. 892809.doi: 10.1117/12.2039090.
16. Picart T., Gautheron A., Caredda C. et al. Fluorescence-Guided Surgical Techniques in Adult Diffuse Low-Grade Gliomas: State-of-the-Art and Emerging Techniques: A Systematic Review // Cancers. – 2024. – Vol. 16. – № 15. – P. 2698.doi: 10.3390/cancers16152698.
17. Maragkou T., Quint K., Pollo B. et al. Intraoperative confocal laser endomicroscopy for brain tumors - potential and challenges from a neuropathological perspective // Free Neuropathology. – 2022. – P. 24 Pages.doi: 10.17879/FREENEUROPATHOLOGY-2022-4369.
18. Sankar T., Delaney P. M., Ryan R. W. et al. Miniaturized Handheld Confocal Microscopy for Neurosurgery: Results in an Experimental Glioblastoma Model // Neurosurgery. – 2010. – Vol. 66. – № 2. – P. 410–418.doi: 10.1227/01.NEU.0000365772.66324.6F.
19. Foersch S., Heimann A., Ayyad A. et al. Confocal Laser Endomicroscopy for Diagnosis and Histomorphologic Imaging of Brain Tumors *In Vivo* // PLoS ONE. – 2012. – Vol. 7. – № 7. – P. e41760.doi: 10.1371/journal.pone.0041760.

20. Martirosyan N. L., Cavalcanti D. D., Eschbacher J. M. et al. Use of *in vivo* near-infrared laser confocal endomicroscopy with indocyanine green to detect the boundary of infiltrative tumor: Laboratory investigation, *Journal of Neurosurgery*, 2011, vol. 115(6), pp. 1131–1138. doi: 10.3171/2011.8.JNS11559.
21. Sanai N., Eschbacher J., Hattendorf G. et al. Intraoperative Confocal Microscopy for Brain Tumors: A Feasibility Analysis in Humans, *Operative Neurosurgery*, 2011, vol. 68, pp. ons282–ons290. doi: 10.1227/NEU.0b013e318212464e.
22. Sanai N., Snyder L. A., Honea N. J. et al. Intraoperative confocal microscopy in the visualization of 5-aminolevulinic acid fluorescence in low-grade gliomas: Clinical article, *Journal of Neurosurgery*, 2011, vol. 115(4), pp. 740–748. doi: 10.3171/2011.6.JNS11252.
23. Eschbacher J., Martirosyan N. L., Nakaji P. et al. *In vivo* intraoperative confocal microscopy for real-time histopathological imaging of brain tumors: Clinical article, *Journal of Neurosurgery*, 2012, vol. 116(4), pp. 854–860. doi: 10.3171/2011.12.JNS11696.
24. Pavlov V., Meyronet D., Meyer-Bisch V. et al. Intraoperative Probe-Based Confocal Laser Endomicroscopy in Surgery and Stereotactic Biopsy of Low-Grade and High-Grade Gliomas: A Feasibility Study in Humans, *Neurosurgery*, 2016, vol. 79(4), pp. 604–612. doi: 10.1227/NEU.0000000000001365.
25. Liu J. T. C., Meza D., Sanai N. Trends in Fluorescence Image-Guided Surgery for Gliomas, *Neurosurgery*, 2014, vol. 75(1), pp. 61–71. doi: 10.1227/NEU.0000000000000344.
26. Sibai M., Veilleux I., Elliott J. T. et al. Quantitative spatial frequency fluorescence imaging in the sub-diffusive domain for image-guided glioma resection, *Biomedical Optics Express*, 2015, vol. 6(12), pp. 4923. doi: 10.1364/BOE.6.004923.
27. Wirth D., Kolste K., Kanick S. et al. Fluorescence depth estimation from wide-field optical imaging data for guiding brain tumor resection: a multi-inclusion phantom study, *Biomedical Optics Express*, 2017, vol. 8(8), pp. 3656. doi: 10.1364/BOE.8.003656.
28. Belykh E., Miller E. J., Carotenuto A. et al. Progress in Confocal Laser Endomicroscopy for Neurosurgery and Technical Nuances for Brain Tumor Imaging With Fluorescein, *Frontiers in Oncology*, 2019, vol. 9, pp. 554. doi: 10.3389/fonc.2019.00554.
29. Abramov I., Park M. T., Belykh E. et al. Intraoperative confocal laser endomicroscopy: prospective *in vivo* feasibility study of a clinical-grade system for brain tumors, *Journal of Neurosurgery*, 2023, vol. 138(3), pp. 587–597. doi: 10.3171/2022.5.JNS2282.
30. Belykh E., Miller E. J., Patel A. A. et al. Diagnostic Accuracy of a Confocal Laser Endomicroscope for *In Vivo* Differentiation Between Normal Injured And Tumor Tissue During Fluorescein-Guided Glioma Resection: Laboratory Investigation, *World Neurosurgery*, 2018, vol. 115, pp. e337–e348. doi: 10.1016/j.wneu.2018.04.048.
31. Acerbi F., Pollo B., De Laurentis C. et al. *Ex Vivo* Fluorescein-Assisted Confocal Laser Endomicroscopy (CONVIVO® System) in Patients With Glioblastoma: Results From a Prospective Study, *Frontiers in Oncology*, 2020, vol. 10, pp. 606574. doi: 10.3389/fonc.2020.606574.
32. Giannoni L., Bonaudo C., Marradi M. et al. Optical characterisation and study of *ex vivo* glioma tissue for hyperspectral imaging during neurosurgery ed. D. Contini, Y. Hoshi, T. D. O'Sullivan, Munich, Germany: SPIE, 2023.p. 81. doi: 10.1117/12.2670854.
33. Fabelo H., Ortega S., Kabwama S. et al. HELICoiD project: a new use of hyperspectral imaging for brain cancer detection in real-time during neurosurgical operations ed. D. P. Bannon, Baltimore, Maryland, United States:, 2016.p. 986002. doi: 10.1117/12.2223075.
34. Fabelo H., Ortega S., Lazcano R. et al. An Intraoperative Visualization System Using Hyperspectral Imaging to Aid in Brain Tumor Delineation, *Sensors*, 2018, vol. 18(2), pp. 430. doi: 10.3390/s18020430.
35. Ezhov I., Giannoni L., Shit S. et al. Identifying chromophore fingerprints of brain tumor tissue on hyperspectral imaging using principal component analysis ed. D. Contini, Y. Hoshi, T. D. O'Sullivan, Munich, Germany: SPIE, 2023.p. 78. doi: 10.1117/12.2670775.
36. Martinez B., Leon R., Fabelo H. et al. Most Relevant Spectral Bands Identification for Brain Cancer Detection Using Hyperspectral Imaging, *Sensors*, 2019, vol. 19(24), pp. 5481. doi: 10.3390/s19245481.

20. Martirosyan N. L., Cavalcanti D. D., Eschbacher J. M. et al. Use of *in vivo* near-infrared laser confocal endomicroscopy with indocyanine green to detect the boundary of infiltrative tumor: Laboratory investigation // Journal of Neurosurgery. – 2011. – Vol. 115. – № 6. – P. 1131–1138.doi: 10.3171/2011.8.JNS11559.
21. Sanai N., Eschbacher J., Hattendorf G. et al. Intraoperative Confocal Microscopy for Brain Tumors: A Feasibility Analysis in Humans // Operative Neurosurgery. – 2011. – Vol. 68. – P. ons282–ons290.doi: 10.1227/NEU.0b013e318212464e.
22. Sanai N., Snyder L. A., Honea N. J. et al. Intraoperative confocal microscopy in the visualization of 5-aminolevulinic acid fluorescence in low-grade gliomas: Clinical article // Journal of Neurosurgery. – 2011. – Vol. 115. – № 4. – P. 740–748.doi: 10.3171/2011.6.JNS11252.
23. Eschbacher J., Martirosyan N. L., Nakaji P. et al. *In vivo* intraoperative confocal microscopy for real-time histopathological imaging of brain tumors: Clinical article // Journal of Neurosurgery. – 2012. – Vol. 116. – № 4. – P. 854–860.doi: 10.3171/2011.12.JNS11696.
24. Pavlov V., Meyronet D., Meyer-Bisch V. et al. Intraoperative Probe-Based Confocal Laser Endomicroscopy in Surgery and Stereotactic Biopsy of Low-Grade and High-Grade Gliomas: A Feasibility Study in Humans // Neurosurgery. – 2016. – Vol. 79. – № 4. – P. 604–612. doi: 10.1227/NEU.0000000000001365.
25. Liu J. T. C., Meza D., Sanai N. Trends in Fluorescence Image-Guided Surgery for Gliomas // Neurosurgery. – 2014. – Vol. 75. – № 1. – P. 61–71.doi: 10.1227/NEU.0000000000000344.
26. Sibai M., Veilleux I., Elliott J. T. et al. Quantitative spatial frequency fluorescence imaging in the sub-diffusive domain for image-guided glioma resection // Biomedical Optics Express. – 2015. – Vol. 6. – № 12. – P. 4923.doi: 10.1364/BOE.6.004923.
27. Wirth D., Kolste K., Kanick S. et al. Fluorescence depth estimation from wide-field optical imaging data for guiding brain tumor resection: a multi-inclusion phantom study // Biomedical Optics Express. – 2017. – Vol. 8. – № 8. – P. 3656.doi: 10.1364/BOE.8.003656.
28. Belykh E., Miller E. J., Carotenuto A. et al. Progress in Confocal Laser Endomicroscopy for Neurosurgery and Technical Nuances for Brain Tumor Imaging With Fluorescein // Frontiers in Oncology. – 2019. – Vol. 9. – P. 554.doi: 10.3389/fonc.2019.00554.
29. Abramov I., Park M. T., Belykh E. et al. Intraoperative confocal laser endomicroscopy: prospective *in vivo* feasibility study of a clinical-grade system for brain tumors // Journal of Neurosurgery. – 2023. – Vol. 138. – № 3. – P. 587–597.doi: 10.3171/2022.5.JNS2282.
30. Belykh E., Miller E. J., Patel A. A. et al. Diagnostic Accuracy of a Confocal Laser Endomicroscope for *In Vivo* Differentiation Between Normal Injured And Tumor Tissue During Fluorescein-Guided Glioma Resection: Laboratory Investigation // World Neurosurgery. – 2018. – Vol. 115. – P. e337–e348.doi: 10.1016/j.wneu.2018.04.048.
31. Acerbi F., Pollo B., De Laurentis C. et al. *Ex Vivo* Fluorescein-Assisted Confocal Laser Endomicroscopy (CONVIVO® System) in Patients With Glioblastoma: Results From a Prospective Study // Frontiers in Oncology. – 2020. – Vol. 10. – P. 606574.doi: 10.3389/fonc.2020.606574.
32. Giannoni L., Bonaudo C., Marradi M. et al. Optical characterisation and study of *ex vivo* glioma tissue for hyperspectral imaging during neurosurgery ed. D. Contini, Y. Hoshi, T. D. O'Sullivan, Munich, Germany: SPIE, 2023. C. 81.doi: 10.1117/12.2670854.
33. Fabelo H., Ortega S., Kabwama S. et al. HELICoiD project: a new use of hyperspectral imaging for brain cancer detection in real-time during neurosurgical operations ed. D. P. Bannon, Baltimore, Maryland, United States:, 2016. C. 986002.doi: 10.1117/12.2223075.
34. Fabelo H., Ortega S., Lazcano R. et al. An Intraoperative Visualization System Using Hyperspectral Imaging to Aid in Brain Tumor Delineation // Sensors. – 2018. – Vol. 18. – № 2. – P. 430.doi: 10.3390/s18020430.
35. Ezhov I., Giannoni L., Shit S. et al. Identifying chromophore fingerprints of brain tumor tissue on hyperspectral imaging using principal component analysis ed. D. Contini, Y. Hoshi, T. D. O'Sullivan, Munich, Germany: SPIE, 2023. C. 78.doi: 10.1117/12.2670775.
36. Martinez B., Leon R., Fabelo H. et al. Most Relevant Spectral Bands Identification for Brain Cancer Detection Using Hyperspectral Imaging // Sensors. – 2019. – Vol. 19. – № 24. – P. 5481.doi: 10.3390/s19245481.

37. DePaoli D., Lemoine É., Ember K. et al. Rise of Raman spectroscopy in neurosurgery: a review, *Journal of Biomedical Optics*, 2020, vol. 25(05), pp. 1. doi: 10.1117/1.JBO.25.5.050901.
38. Romanishkin I. D., Savelieva T. A., Ospanov A. et al. Classification of intracranial tumors based on optical-spectral analysis, *Biomedical Photonics*, 2023, vol. 12(3), pp. 4–10. doi: 10.24931/2413-9432-2023-12-3-4-10.
39. Romanishkin I., Savelieva T., Kosyrkova A. et al. Differentiation of glioblastoma tissues using spontaneous Raman scattering with dimensionality reduction and data classification, *Frontiers in Oncology*, 2022, vol. 12, pp. 944210. doi: 10.3389/fonc.2022.944210.
40. Hollon T., Orringer D. A. Label-free brain tumor imaging using Raman-based methods, *Journal of Neuro-Oncology*, 2021, vol. 151(3), pp. 393–402. doi: 10.1007/s11060-019-03380-z.
41. Kast R., Auner G., Yurgelevic S. et al. Identification of regions of normal grey matter and white matter from pathologic glioblastoma and necrosis in frozen sections using Raman imaging, *Journal of Neuro-Oncology*, 2015, vol. 125(2), pp. 287–295. doi: 10.1007/s11060-015-1929-4.
42. Hollon T., Jiang C., Chowdury A. et al. Artificial-intelligence-based molecular classification of diffuse gliomas using rapid, label-free optical imaging, *Nature Medicine*, 2023, vol. 29(4), pp. 828–832. doi: 10.1038/s41591-023-02252-4.
43. Hollon T. C., Pandian B., Adapa A. R. et al. Near real-time intraoperative brain tumor diagnosis using stimulated Raman histology and deep neural networks, *Nature Medicine*, 2020, vol. 26(1), pp. 52–58. doi: 10.1038/s41591-019-0715-9.
44. Evans C. L., Xu X., Kesari S. et al. Chemically-selective imaging of brain structures with CARS microscopy, *Optics Express*, 2007, vol. 15(19), pp. 12076. doi: 10.1364/OE.15.012076.
45. Uckermann O., Galli R., Tamosaityte S. et al. Label-Free Delineation of Brain Tumors by Coherent Anti-Stokes Raman Scattering Microscopy in an Orthotopic Mouse Model and Human Glioblastoma, *PLoS ONE*, 2014, vol. 9(9), pp. e107115. doi: 10.1371/journal.pone.0107115.
46. Mascagni P., Alapatt D., Sestini L. et al. Computer vision in surgery: from potential to clinical value, *npj Digital Medicine*, 2022, vol. 5(1), pp. 163. doi: 10.1038/s41746-022-00707-5.
47. Rau A., Edwards P. J. E., Ahmad O. F. et al. Implicit domain adaptation with conditional generative adversarial networks for depth prediction in endoscopy, *International Journal of Computer Assisted Radiology and Surgery*, 2019, vol. 14(7), pp. 1167–1176. doi: 10.1007/s11548-019-01962-w.
48. Kassem H., Alapatt D., Mascagni P. et al. Federated Cycling (FedCy): Semi-Supervised Federated Learning of Surgical Phases, *IEEE Transactions on Medical Imaging*, 2023, vol. 42(7), pp. 1920–1931. doi: 10.1109/TMI.2022.3222126.
49. Orringer D. A., Pandian B., Niknafs Y. S. et al. Rapid intraoperative histology of unprocessed surgical specimens via fibre-laser-based stimulated Raman scattering microscopy, *Nature Biomedical Engineering*, 2017, vol. 1(2), pp. 0027. doi: 10.1038/s41551-016-0027.
50. Leon R., Fabelo H., Ortega S. et al. Hyperspectral imaging benchmark based on machine learning for intraoperative brain tumour detection, *npj Precision Oncology*, 2023, vol. 7(1), pp. 119. doi: 10.1038/s41698-023-00475-9.
51. Fabelo H., Halicek M., Ortega S. et al. Deep Learning-Based Framework for *In Vivo* Identification of Glioblastoma Tumor using Hyperspectral Images of Human Brain, *Sensors*, 2019, vol. 19(4), pp. 920. doi: 10.3390/s19040920.
52. Ravi D., Fabelo H., Callic G. M. et al. Manifold Embedding and Semantic Segmentation for Intraoperative Guidance With Hyperspectral Brain Imaging, *IEEE Transactions on Medical Imaging*, 2017, vol. 36(9), pp. 1845–1857. doi: 10.1109/TMI.2017.2695523.
53. Fabelo H., Ortega S., Ravi D. et al. Spatio-spectral classification of hyperspectral images for brain cancer detection during surgical operations, *PLOS ONE*, 2018, vol. 13(3), pp. e0193721. doi: 10.1371/journal.pone.0193721.
54. Florimbi G., Fabelo H., Torti E. et al. Accelerating the K-Nearest Neighbors Filtering Algorithm to Optimize the Real-Time Classification of Human Brain Tumor in Hyperspectral Images, *Sensors*, 2018, vol. 18(7), pp. 2314. doi: 10.3390/s18072314.

37. DePaoli D., Lemoine É., Ember K. et al. Rise of Raman spectroscopy in neurosurgery: a review // Journal of Biomedical Optics. – 2020. – Vol. 25. – № 05. – P. 1.doi: 10.1117/1.JBO.25.5.050901.
38. Romanishkin I. D., Savelieva T. A., Ospanov A. et al. Classification of intracranial tumors based on optical-spectral analysis // Biomedical Photonics. – 2023. – Vol. 12. – № 3. – P. 4–10.doi: 10.24931/2413-9432-2023-12-3-4-10.
39. Romanishkin I., Savelieva T., Kosyrkova A. et al. Differentiation of glioblastoma tissues using spontaneous Raman scattering with dimensionality reduction and data classification // Frontiers in Oncology. – 2022. – Vol. 12. – P. 944210.doi: 10.3389/fonc.2022.944210.
40. Hollon T., Orringer D. A. Label-free brain tumor imaging using Raman-based methods // Journal of Neuro-Oncology. – 2021. – Vol. 151. – № 3. – P. 393–402.doi: 10.1007/s11060-019-03380-z.
41. Kast R., Auner G., Yurgelevic S. et al. Identification of regions of normal grey matter and white matter from pathologic glioblastoma and necrosis in frozen sections using Raman imaging // Journal of Neuro-Oncology. – 2015. – Vol. 125. – № 2. – P. 287–295.doi: 10.1007/s11060-015-1929-4.
42. Hollon T., Jiang C., Chowdury A. et al. Artificial-intelligence-based molecular classification of diffuse gliomas using rapid, label-free optical imaging // Nature Medicine. – 2023. – Vol. 29. – № 4. – P. 828–832.doi: 10.1038/s41591-023-02252-4.
43. Hollon T. C., Pandian B., Adapa A. R. et al. Near real-time intraoperative brain tumor diagnosis using stimulated Raman histology and deep neural networks // Nature Medicine. – 2020. – Vol. 26. – № 1. – P. 52–58.doi: 10.1038/s41591-019-0715-9.
44. Evans C. L., Xu X., Kesari S. et al. Chemically-selective imaging of brain structures with CARS microscopy // Optics Express. – 2007. – Vol. 15. – № 19. – P. 12076.doi: 10.1364/OE.15.012076.
45. Uckermann O., Galli R., Tamosaityte S. et al. Label-Free Delineation of Brain Tumors by Coherent Anti-Stokes Raman Scattering Microscopy in an Orthotopic Mouse Model and Human Glioblastoma // PLoS ONE. – 2014. – Vol. 9. – № 9. – P. e107115.doi: 10.1371/journal.pone.0107115.
46. Mascagni P., Alapatt D., Sestini L. et al. Computer vision in surgery: from potential to clinical value // npj Digital Medicine. – 2022. – Vol. 5. – № 1. – P. 163.doi: 10.1038/s41746-022-00707-5.
47. Rau A., Edwards P. J. E., Ahmad O. F. et al. Implicit domain adaptation with conditional generative adversarial networks for depth prediction in endoscopy // International Journal of Computer Assisted Radiology and Surgery. – 2019. – Vol. 14. – № 7. – P. 1167–1176.doi: 10.1007/s11548-019-01962-w.
48. Kassem H., Alapatt D., Mascagni P. et al. Federated Cycling (FedCy): Semi-Supervised Federated Learning of Surgical Phases // IEEE Transactions on Medical Imaging. – 2023. – Vol. 42. – № 7. – P. 1920–1931.doi: 10.1109/TMI.2022.3222126.
49. Orringer D. A., Pandian B., Niknafs Y. S. et al. Rapid intraoperative histology of unprocessed surgical specimens via fibre-laser-based stimulated Raman scattering microscopy // Nature Biomedical Engineering. – 2017. – Vol. 1. – № 2. – P. 0027.doi: 10.1038/s41551-016-0027.
50. Leon R., Fabelo H., Ortega S. et al. Hyperspectral imaging benchmark based on machine learning for intraoperative brain tumour detection // npj Precision Oncology. – 2023. – Vol. 7. – № 1. – P. 119.doi: 10.1038/s41698-023-00475-9.
51. Fabelo H., Halicek M., Ortega S. et al. Deep Learning-Based Framework for *In Vivo* Identification of Glioblastoma Tumor using Hyperspectral Images of Human Brain // Sensors. – 2019. – Vol. 19. – № 4. – P. 920.doi: 10.3390/s19040920.
52. Ravi D., Fabelo H., Callic G. M. et al. Manifold Embedding and Semantic Segmentation for Intraoperative Guidance With Hyperspectral Brain Imaging // IEEE Transactions on Medical Imaging. – 2017. – Vol. 36. – № 9. – P. 1845–1857.doi: 10.1109/TMI.2017.2695523.
53. Fabelo H., Ortega S., Ravi D. et al. Spatio-spectral classification of hyperspectral images for brain cancer detection during surgical operations // PLOS ONE. – 2018. – Vol. 13. – № 3. – P. e0193721.doi: 10.1371/journal.pone.0193721.
54. Florimbi G., Fabelo H., Torti E. et al. Accelerating the K-Nearest Neighbors Filtering Algorithm to Optimize the Real-Time Classification of Human Brain Tumor in Hyperspectral Images // Sensors. – 2018. – Vol. 18. – № 7. – P. 2314.doi: 10.3390/s18072314.

55. Zhang Y., Cao G., Li X. et al. Cascaded Random Forest for Hyperspectral Image Classification, *IEEE Journal of Selected Topics in Applied Earth Observations and Remote Sensing*, 2018, vol. 11(4), pp. 1082–1094. doi: 10.1109/JSTARS.2018.2809781.
56. Xia J., Ghamisi P., Yokoya N. et al. Random Forest Ensembles and Extended Multiextinction Profiles for Hyperspectral Image Classification, *IEEE Transactions on Geoscience and Remote Sensing*, 2018, vol. 56(1), pp. 202–216. doi: 10.1109/TGRS.2017.2744662.
57. Ayaz H., Tormey D., McLoughlin I. et al. Hyperspectral Brain Tissue Classification using a Fast and Compact 3D CNN Approach Genova, Italy: IEEE, 2022.p. 1–4. doi: 10.1109/IPAS55744.2022.10053044.
58. Baig N., Fabelo H., Ortega S. et al. Empirical Mode Decomposition Based Hyperspectral Data Analysis for Brain Tumor Classification Mexico: IEEE, 2021.p. 2274–2277. doi: 10.1109/EMBC46164.2021.9629676.
59. Cruz-Guerrero I. A., Leon R., Campos-Delgado D. U. et al. Classification of Hyperspectral *In Vivo* Brain Tissue Based on Linear Unmixing, *Applied Sciences*, 2020, vol. 10(16), pp. 5686. doi: 10.3390/app10165686.
60. Ruiz L., Martin A., Urbanos G. et al. Multiclass Brain Tumor Classification Using Hyperspectral Imaging and Supervised Machine Learning Segovia, Spain: IEEE, 2020.p. 1–6. doi: 10.1109/DCIS51330.2020.9268650.
61. Salvador R., Fabelo H., Lazcano R. et al. Demo: HELICoiD tool demonstrator for real-time brain cancer detection Rennes, France: IEEE, 2016.p. 237–238. doi: 10.1109/DASIP.2016.7853831.
62. Sutradhar P., Sancho J., Villa M. et al. Exploration of Realtime Brain tumor classification from Hyperspectral Images in Heterogeneous Embedded MPSoC Pamplona, Spain: IEEE, 2022.p. 01–06. doi: 10.1109/DCIS55711.2022.9970064.
63. Torti E., Florimbi G., Castelli F. et al. Parallel K-Means Clustering for Brain Cancer Detection Using Hyperspectral Images, *Electronics*, 2018, vol. 7(11), pp. 283. doi: 10.3390/electronics7110283.
64. Urbanos G., Martín A., Vázquez G. et al. Supervised Machine Learning Methods and Hyperspectral Imaging Techniques Jointly Applied for Brain Cancer Classification, *Sensors*, 2021, vol. 21(11), pp. 3827. doi: 10.3390/s21113827.
65. Manni F., Van Der Sommen F., Fabelo H. et al. Hyperspectral Imaging for Glioblastoma Surgery: Improving Tumor Identification Using a Deep Spectral-Spatial Approach, *Sensors*, 2020, vol. 20(23), pp. 6955. doi: 10.3390/s20236955.
66. Fürtjes G., Reinecke D., Von Spreckelsen N. et al. Intraoperative microscopic autofluorescence detection and characterization in brain tumors using stimulated Raman histology and two-photon fluorescence, *Frontiers in Oncology*, 2023, vol. 13, pp. 1146031. doi: 10.3389/fonc.2023.1146031.
67. Reinecke D., Von Spreckelsen N., Mawrin C. et al. Novel rapid intraoperative qualitative tumor detection by a residual convolutional neural network using label-free stimulated Raman scattering microscopy, *Acta Neuropathologica Communications*, 2022, vol. 10(1), pp. 109. doi: 10.1186/s40478-022-01411-x.
68. Shirshin E. A., Yakimov B. P., Darvin M. E. et al. Label-Free Multiphoton Microscopy: The Origin of Fluorophores and Capabilities for Analyzing Biochemical Processes, *Biochemistry (Moscow)*, 2019, vol. 84(S1), pp. 69–88. doi: 10.1134/S0006297919140050.
69. Uckermann O., Galli R., Mark G. et al. Label-free multiphoton imaging allows brain tumor recognition based on texture analysis–a study of 382 tumor patients, *Neuro-Oncology Advances*, 2020, vol. 2(1), pp. vdaa035. doi: 10.1093/noajnl/vdaa035.
70. Lita A., Sjöberg J., Păcioianu D. et al. Raman-based machine-learning platform reveals unique metabolic differences between IDHmut and IDHwt glioma, *Neuro-Oncology*, 2024, vol. 26(11), pp. 1994–2009. doi: 10.1093/neuonc/noae101.
71. Morais C. L. M., Lilo T., Ashton K. M. et al. Determination of meningioma brain tumour grades using Raman micro-spectroscopy imaging, *The Analyst*, 2019, vol. 144(23), pp. 7024–7031. doi: 10.1039/C9AN01551E.

55. Zhang Y., Cao G., Li X. et al. Cascaded Random Forest for Hyperspectral Image Classification // IEEE Journal of Selected Topics in Applied Earth Observations and Remote Sensing. – 2018. – Vol. 11. – № 4. – P. 1082–1094.doi: 10.1109/JSTARS.2018.2809781.
56. Xia J., Ghamisi P., Yokoya N. et al. Random Forest Ensembles and Extended Multiextinction Profiles for Hyperspectral Image Classification // IEEE Transactions on Geoscience and Remote Sensing. – 2018. – Vol. 56. – № 1. – P. 202–216.doi: 10.1109/TGRS.2017.2744662.
57. Ayaz H., Tormey D., McLoughlin I. et al. Hyperspectral Brain Tissue Classification using a Fast and Compact 3D CNN Approach Genova, Italy: IEEE, 2022. C. 1–4.doi: 10.1109/IPAS55744.2022.10053044.
58. Baig N., Fabelo H., Ortega S. et al. Empirical Mode Decomposition Based Hyperspectral Data Analysis for Brain Tumor Classification Mexico: IEEE, 2021. C. 2274–2277.doi: 10.1109/EMBC46164.2021.9629676.
59. Cruz-Guerrero I. A., Leon R., Campos-Delgado D. U. et al. Classification of Hyperspectral *In Vivo* Brain Tissue Based on Linear Unmixing // Applied Sciences. – 2020. – Vol. 10. – № 16. – P. 5686. doi: 10.3390/app10165686.
60. Ruiz L., Martin A., Urbanos G. et al. Multiclass Brain Tumor Classification Using Hyperspectral Imaging and Supervised Machine Learning Segovia, Spain: IEEE, 2020. C. 1–6.doi: 10.1109/DCIS51330.2020.9268650.
61. Salvador R., Fabelo H., Lazcano R. et al. Demo: HELICoiD tool demonstrator for real-time brain cancer detection Rennes, France: IEEE, 2016. C. 237–238.doi: 10.1109/DASIP.2016.7853831.
62. Sutradhar P., Sancho J., Villa M. et al. Exploration of Realtime Brain tumor classification from Hyperspectral Images in Heterogeneous Embedded MPSoC Pamplona, Spain: IEEE, 2022. C. 01–06.doi: 10.1109/DCIS55711.2022.9970064.
63. Torti E., Florimbi G., Castelli F. et al. Parallel K-Means Clustering for Brain Cancer Detection Using Hyperspectral Images // Electronics. – 2018. – Vol. 7. – № 11. – P. 283.doi: 10.3390/electronics7110283.
64. Urbanos G., Martín A., Vázquez G. et al. Supervised Machine Learning Methods and Hyperspectral Imaging Techniques Jointly Applied for Brain Cancer Classification // Sensors. – 2021. – Vol. 21. – № 11. – P. 3827.doi: 10.3390/s21113827.
65. Manni F., Van Der Sommen F., Fabelo H. et al. Hyperspectral Imaging for Glioblastoma Surgery: Improving Tumor Identification Using a Deep Spectral-Spatial Approach // Sensors. – 2020. – Vol. 20. – № 23. – P. 6955.doi: 10.3390/s20236955.
66. Fürtjes G., Reinecke D., Von Spreckelsen N. et al. Intraoperative microscopic autofluorescence detection and characterization in brain tumors using stimulated Raman histology and two-photon fluorescence // Frontiers in Oncology. – 2023. – Vol. 13. – P. 1146031.doi: 10.3389/fonc.2023.1146031.
67. Reinecke D., Von Spreckelsen N., Mawrin C. et al. Novel rapid intraoperative qualitative tumor detection by a residual convolutional neural network using label-free stimulated Raman scattering microscopy // Acta Neuropathologica Communications. – 2022. – Vol. 10. – № 1. – P. 109.doi: 10.1186/s40478-022-01411-x.
68. Shirshin E. A., Yakimov B. P., Darvin M. E. et al. Label-Free Multiphoton Microscopy: The Origin of Fluorophores and Capabilities for Analyzing Biochemical Processes // Biochemistry (Moscow). – 2019. – Vol. 84. – № S1. – P. 69–88.doi: 10.1134/S0006297919140050.
69. Uckermann O., Galli R., Mark G. et al. Label-free multiphoton imaging allows brain tumor recognition based on texture analysis—a study of 382 tumor patients // Neuro-Oncology Advances. – 2020. – Vol. 2. – № 1. – P. vdaa035.doi: 10.1093/noajnl/vdaa035.
70. Lita A., Sjöberg J., Păcioianu D. et al. Raman-based machine-learning platform reveals unique metabolic differences between IDHmut and IDHwt glioma // Neuro-Oncology. – 2024. – Vol. 26. – № 11. – P. 1994–2009.doi: 10.1093/neuonc/noae101.
71. Morais C. L. M., Lilo T., Ashton K. M. et al. Determination of meningioma brain tumour grades using Raman microspectroscopy imaging // The Analyst. – 2019. – Vol. 144. – № 23. – P. 7024–7031. doi: 10.1039/C9AN01551E.

ФОТОСЕНСИБИЛИЗАТОРЫ НОВОГО ПОКОЛЕНИЯ ДЛЯ ФОТОДИНАМИЧЕСКОЙ ТЕРАПИИ

«ФОТОДИТАЗИН®» концентрат для приготовления раствора для инфузий — лекарственное средство (РУ № ЛС 001246 от 18.05.2012 г.)
«ФОТОДИТАЗИН®» гель — изделие медицинского назначения (РУ № ФСР 2012/13043 от 03.02.2012 г.)
«ФОТОДИТАГЕЛЬ®» — косметическое средство (ДС ЕАЭС № RU Д-RU.НВ42.В.06108/20 от 24.09.2020 г.)

Препараты применяются для флюоресцентной диагностики и фотодинамической терапии злокачественных новообразований, а также патологий неонкологического характера в следующих областях медицины:

- гинекология
- урология
- нейрохирургия
- торакальная хирургия
- офтальмология
- травматология
- ортопедия
- комбустиология
- гнойная хирургия
- дерматология
- косметология
- стоматология

www.fotoditazin.com
www.фотодитазин.рф

@FOTODITAZIN

@FOTODITAGEL_FDT

ООО «ВЕТА-ГРАНД»
123056, г. Москва, ул. Красина, д. 27, стр. 2
Тел.: +7 (499) 250-40-00, +7 (929) 971-44-46
E-mail: veta-grand@mail.ru